Doctoral Thesis

Visual Data-Driven Millimeter Wave Communication Systems

Yusuke KODA

Graduate School of Informatics, Kyoto University

March 2021

Preface

This thesis primarily aims at providing the feasibility of visual data-driven proactive performance prediction of millimeter wave (mmWave) communications subject to dynamic line-of-sight (LoS) blockage effects. The sequence of visual data involves spatio-temporal information on objects in a camera's field-of-view and hence captures mobility patterns of potential blockage obstacles that could not necessarily be captured based only on a radio frequency (RF) received power sequence. This feature of visual data brings the proactive performance prediction (e.g., received power and throughput) and proactive control (e.g., handover) into mmWave communication systems. Given this capability, the goal of this thesis opens up opportunities for leveraging visual data in mmWave wireless communication systems towards supporting data-intensive applications, by shedding lights on *1)* the benefits from the usage of visual data and the combinatorial usage of visual image and RF received power sequences, and *2)* methodology to alleviate the concern in collecting visual data, such as a higher communication cost and privacy leakage.

As a methodological building block to achieve this goal, this thesis first develops a measurement system capturing received powers of mmWave signals transmitted by off-the-shelf IEEE 802.11ad wireless LAN (WLAN) access points (APs) with packet-mode signal transmission. This system comprises a low-cost microwave spectrum analyzer and targets at capturing dynamic characteristics of received power attenuations due to LoS blockages. Owing to the capability of capturing time-varying received power sequences affected by LoS blockages, this system is leveraged through this thesis, particularly in experimental evaluations.

Given the measurement system, this thesis experimentally demonstrates the feasibility of triggering a handover proactively while predicting future throughput performance in each BS affected by LoS blockages. Because of a rapid attenuation of received powers due to a LoS blockage, predicting future throughput performance prior to the blockage occurrence is quite challenging. Hence, as discussed earlier, this thesis leverages visual data as side information to determine handover timing. Meanwhile, the usage of visual data brings another challenge of handling the large dimensionality of each image in a handover decision-making problem. To overcome the difficulty, this thesis leverages deep reinforcement learning known as a recent solution to handle the large dimensionality of visual data. Experimental evaluations show that as human obstacles approach a BS, the predicted throughput of the BS becomes lower prior to LoS blockages, and that this characteristic could not necessarily be obtained only with RF received powers. This exactly confirms the feasibility of the aforementioned proactive prediction. Moreover, owing to the proactive prediction, a handover is triggered prior to the LoS blockage events, which results in higher throughput than a baseline handover framework without visual data.

Subsequently, going beyond system architectures relying only on visual data, this thesis integrates visual data and RF received power sequences to enhance the prediction accuracy in future received powers. As discussed above, visual data is informative to predict sudden variations in future received powers. Meanwhile, current RF received powers are also informative to predict future received powers particularly when the received power values are highly correlated within a longer period in LoS conditions. By integrating such two features held by visual and RF received power data, one can perform unprecedentedly accurate predictions. Experimental results demonstrate the feasibility of benefitting from both two modalities, showing the accuracy improvement from single modality-based predictions, i.e., predictions based only on visual data or RF received power data sequences.

Moreover, in the course of the attempt to integrate these two modalities, this thesis addresses the problem of collecting visual data in a communication-efficient and privacy-preserving manner. The key idea is to leverage a split learning technique. Therein, the upper segment is distributed to a BS and integrates images and received powers for future received power prediction. Meanwhile, the lower segment is distributed to a camera and extracts image features from visual data. Owing to the split learning, the camera does not need to upload raw visual data and instead, uploads abstract compressed image features, which contribute to both privacy and communication efficiency. Moreover, by varying the compression intensity of the image features, this thesis further reduces communication costs and privacy leakage. Remarkably, experiments demonstrate that prediction accuracy does not necessarily trade-off with communication efficiency and privacy levels, by showing that compressing the lower segment output yields lower communication latency and less privacy leakage without sacrificing the prediction accuracy.

The chapters of this thesis are as follows. Chapter 1 discusses the background motivation and overview of this thesis. Chapter 2 introduces related technologies focusing on principles of leveraged machine learning techniques. Chapter 3 provides the measurement system for received powers of signals transmitted by packet-mode IEEE 802.11ad WLAN APs, which is thoroughly used in the subsequent chapters. Chapter 4 presents a visual data-driven handover framework with proactive performance prediction of each BS. Chapter 5 presents multimodal, i.e., visual and RF received power-based, received power prediction framework and addresses the communication costs and privacy leakages in collecting visual data. Finally, Chapter 6 concludes this thesis.

Acknowledgements

First of all, I would like to express my sincerest appreciation to my supervisor, Professor Masahiro Morikura for his valuable advice and continuous encouragement. From my joining his laboratory, he has given me various advices based on his vast knowledge while giving a great deal of freedom in my work. Without his constant help, the work in this dissertation would have never been completed.

I also greatly appreciate Associate Professor Koji Yamamoto. He directly supervised me, and his careful check and insightful comments on every manuscript I made were enormously helpful to me. Moreover, the countless discussions allowed me to stay focused and high-spirited.

I am genuinely grateful to Associate Professor Takayuki Nishio of School of Engineering, Tokyo Institute of Technology for his immense support, comments, and criticism on my research. Moreover, not only the regular meeting discussions, but also the frank discussions in the office kept me inspired and allowed me to embark on new research topics.

I would like to express my deep appreciation to Professor Hiroshi Harada and Professor Eiji Oki of the Graduate School of Informatics, Kyoto University for acting as opponents in the public defence and for giving valuable advices and incisive comments. Their advice and comments have been a great help in improving this dissertation.

I would like to thank Professor Mehdi Bennis of Centre for Wireless Communications, Oulu University, for giving me a warm welcome to his Intelligent Connectivity and Networks/Systems Group in 2019 and for inspiring me with various interesting ideas. I would also like to thank Lecturer Jihong Park of School of Info Technology, Deakin University. Not only during my visit in Oulu, but also after the visit, he supported me many times for completing the work on MultSL.

Finally, I am extremely grateful to the laboratory secretaries and student members of the Integrated-Media Communications Laboratory of Graduate School of Informatics, Kyoto University. Their considerable support and comments were invaluable.

Contents

List of Figures

List of Tables

Notations

Notation	Description
$\mathbb{R}$	Real numbers
$\mathbb{R}^n$	n-dimensional Euclidean space
$\mathbb{N}$	Natural numbers not including 0
$\mathbb{Z}$	Integers
$[a, b]$	Real numbers ranging from a to b for $a, b \in \mathbb{R}$
$\mathcal{A} \cup \mathcal{B}$	Union of sets $\mathcal{A}$ and $\mathcal{B}$
$\mathcal{A} \cap \mathcal{B}$	Intersection of sets $\mathcal{A}$ and $\mathcal{B}$
$\mathcal{A} \times \mathcal{B}$	Cartesian product of sets $\mathcal{A}$ and $\mathcal{B}$
$\mathcal{A}^N$	Nth Cartesian power of set $\mathcal{A}$
$\lvert\mathcal{A}\rvert$	Cardinality of set $\mathcal{A}$
$\lVert\boldsymbol{a}\rVert$	Euclidean norm of vector $\boldsymbol{a}$
$\min_{condition}$	Minimum operator under the condition
$\max_{condition}$	Maximum operator under the condition
$\mathbb{P}(A)$	Probability of event A
$\mathbb{P}(A \mid B)$	Conditional probability of A given B
$\mathbb{E}[\cdot]$	Expectation operator
$\mathbb{E}[\cdot \mid condition]$	Expectation operator given the condition
$(\cdot)^{\mathrm{T}}$	Transpose
$\lfloor\cdot\rfloor$	Floor function
$\nabla_{\boldsymbol{\theta}} f$	Gradient of f w.r.t. $\boldsymbol{\theta}$

Abbreviations

Abbreviation	Description
AIC	Akaike information criterion
AP	access point
AR	augmented reality
BIC	Bayes information criterion
BP	back propagation
BS	base station
CDF	cumulative distribution function
CNN	convolutional neural network
DP	dynamic programming
EM	expectation maximization
FP	forward propagation
GD	gradient descent
HMM	hidden Markov model
HPBW	half-power beam width
LoS	line-of-sight
LSTM	long-term short memory
MDP	Markov decision process
ML	machine learning
mmWave	millimeter wave
MSE	mean square error
MultSL	multimodal split learning
NLoS	non line-of-sight
NN	neural network
PHY	physical layer

Abbreviation	Description
ReLU	rectified linear unit
RF	radio frequency
RL	reinforcement learning
RMSE	root mean square error
RX	receiver
SGD	stochastic gradient descent
SL	split learning
STA	station
TCP	transmission control protocol
TX	transmitter
UE	user equipment
VR	virtual reality
V2X	vehicle-to-everything
WLAN	wireless local area network

Chapter 1

Introduction

1.1 Motivation

With the development of electronic devices and computer science, various data-intensive applications will emerge in our society and will give rise to significant demand for making higher data rate wireless communications available everywhere. Among these, high-resolution real-time visual data streaming for extending the field of view of humans eyes is receiving tremendous attention and has either indoor and outdoor use cases. For example, real-time ultra-high-resolution video or virtual reality (VR) data streaming of sports or concert scenes brings an immersive experience to content consumers no matter they are in a stadium, concert hall, and their private room. Besides entertainment services, VR data streaming brings an opportunity for remote operations to surgeons in an operating room or construction practitioners in an outside construction site. Camera image data streaming realizes a cooperative perception among vehicles in on-road environments in a vehicle-to-everything (V2X) networks [1]. These motivate to go beyond mega-bit-per-seconds data transmission in current wireless communication systems and to achieve giga-bit-per-seconds data transmission, which should be realized in various environments.

As a key enabler to meet such high-data-rate requirements, millimeter wave (mmWave) communications have attracted a lot of attention in both industrial and academic research areas [2]. This is because in the mmWave bands, a large amount of bandwidth is available, and the usage of such a larger bandwidth is an efficient way to enhance the wireless data rate. For example, in the licensed band in Japan, the bandwidth of 400 MHz in the 28 GHz spectrum was allocated to each mobile operator in 2019, which is larger than the allocated bandwidth in the microwave spectrum that amounts for the order of 10 MHz per each band. In the unlicensed band, the spectrum ranging from 57 GHz to 66 GHz is available in Japan for wireless communication systems. Although the number of available channels is limited to four, this is much larger than the spectrum in the unlicensed microwave band, i.e., 2.4 GHz and 5 GHz band upon which the current Wi-Fi® systems operate.

The historical background of the international standardization tells the fact that mmWave communication gradually expands its usage model such that it can be used in heterogeneous environments. The initial standardization approval dates back to the 2000s, wherein the following three international standards were approved [3]: WirelessHD, IEEE 802.15.3c, and European Computer Manufacturers Association (ECMA)-387. The common feature of these three standardizations is the transmission range of the order of several meters, which targets indoor personal areas[1]. At this time, particularly in the IEEE 802.15.3c standard, a beamforming protocol was established [5], which is referred to as a protocol to align directional antennas and is an essential procedure for the successful operation of the mmWave band. These standardizations were followed by the approval of the IEEE 802.11ad standard in 2012 [6]. Although many usage models were common with IEEE 802.15.3c, the IEEE 802.11ad standard added the wireless local area networks to the usage model of mmWave communications and

---

[1] The difference between WirelessHD/IEEE 802.15.3c and ECMA-387 is the multiple access method. The two former standards apply coordinated time division multiple access by forming a centralized network termed piconet in an ad hoc manner to enhance the reliability of data transmission [4], whereas the ECMA-387 applies contention-based fully distributed multiple access method. The difference between WirelessHD and IEEE 802.15.3c is in the variety of the applications. Specifically, WirelessHD mainly targets uncompressed video streaming, whereas IEEE 802.15.3c targets uncompressed video streaming, office desktop, conference ad hoc, and kiosk file downloading by defining three types of physical layer designs [4].

extended the transmission range to the order of up to several tens meters by employing multi-hop relaying[2]. At the time of writing, the recent IEEE 802.11 task group ay discusses adding wireless fronthauling/backhauling to the usage model of mmWave communications [7], which are the use cases in outdoor environments. Besides, the IEEE 802.11 task group bd, which is developing new specifications for V2X communications, discusses applying mmWave communications optionally [1]. As for the cellular networks, the 28 GHz band became available in many countries in response to the third generation partnership project (3GPP) defining the fifth-generation (5G) new radio in release 15 [8]. This will open up diverse mmWave communications use cases in both indoor and outdoor scenarios including the applications discussed at the beginning of this section.

However, the mmWave communications suffer from rapid and drastic degradation in received powers caused by line-of-sight (LoS) path blockages. This is mainly attributed to larger diffraction loss in the mmWave spectrum and the usage of directional antennas [9]. More specifically, the diffraction loss in decibel scale is typically calculated by [10]:

$$6.9 + 20 \log\left(\sqrt{(\nu - 0.1)^2 + 1} + \nu - 0.1\right),$$

where

$$\nu = h\sqrt{\frac{2}{\lambda}\left(\frac{1}{d_1} + \frac{1}{d_2}\right)}. \tag{1.1}$$

In the above equation, h, d_1, and d_2 are constant, and λ denotes the wavelength. As λ decreases (i.e., the frequency increases), ν and diffraction loss increases, which is the reason for the larger attenuation in received power due to LoS path blockages[3]. Moreover, the usage of directional antennas to compensate for the large path loss in the mmWave spectrum limits the radiation powers of diffraction paths, which further deviates the received

---

[2] In terms of multiple access methods, there is a difference between the IEEE 802.15.3c and IEEE 802.11ad standards. The IEEE 802.15.3c standard employs coordinated time-division multiple access, whereas the IEEE 802.11ad standard mainly employs a distributed contention-based multiple access method.

[3] This is validated via propagation experiments in [9].

powers. The large number of measurement campaigns in [9, 11–13] show that the attenuation of the received power due to the LoS blockage in a fixed directional beam amounts for the order of 10 dB, which is also shown in Chapter 3 in this thesis. This attenuation causes considerable packet loss and throughput degradation and deters the user experience in the aforementioned applications, which should be solved from a system-level perspective.

From a PHY layer perspective, leveraging multiple beams is one approach to combat the LoS blockage, which searches for the reflected path with strong received power. Indeed, in 2008, Panasonic corporation developed televisions compliant to the WirelessHD standard collaborating with SciBEAM corporation, wherein such a beam search mechanism was implemented. According to those companies, the implemented modules could avoid the blockage events by searching for a reflected path from wall surfaces, thereby providing reliable links even if obstacles block a LoS path [14].

However, given that mmWave communication is acquiring use cases not only in indoor personal areas as targeted by Wireless HD but also in indoor/outdoor open areas, beam search is not necessarily sufficient to combat the LoS blockage problem. This is because the distance from a receiver/transmitter to a reflection point depends on the channel environment, and reflected waves cannot necessarily reach the receiver with a feasible received power due to path loss, particularly in open spaces. Fig. 1.1 validates this fact, which shows the throughput of the link established by a pair of IEEE 802.11ad-compliant smart-phones termed ROG®phone [15] for different channel environments under a blockage effect. Specifically, in the smart-phone, a beam search mechanism is implemented in compliance with the IEEE 802.11ad amendment [6][4]. The measurement was performed in three types of channel environments: a narrow corridor, an indoor room in the south part of the no. 9 research building in the main campus of Kyoto University, and an open outdoor space surrounded by the no. 2 research

---

[4] Note that these results are not specific to the IEEE 802.11ad standard. Although the IEEE 802.15.3c standard may provide more reliable links owing to almost contention-free time-division multiple access, the problem is not attributed to multiple access methods but is attributed to the weakness of the second reflected path. This problem will generally happen in mmWave communications.

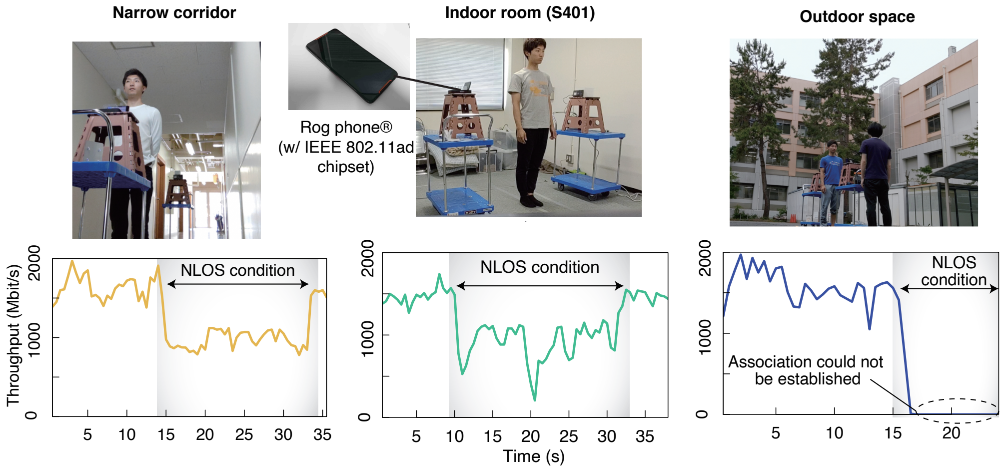

Figure 1.1: Throughput under blockage event in different channel environment. This throughput measurement is performed by the author. The throughput was measured via Iperf3 [16] generating a transmission control protocol (TCP) traffic and outputting a log of TCP throughput.

building in the main campus of Kyoto University. To focus on the difference of the channel environments, the measurement is performed under the same conditions in terms of both the distance between the phones and that between the human obstacle and either phone[5]. From Fig. 1.1, one can see that throughput under blockage effects is different for the channel environment and that the degradation in throughput in an open outdoor space is severe even if multiple beams and beam search mechanisms are implemented.

This observation debunks the necessity of not only multiple beams, but also multiple base stations (BSs) to gain a link redundancy and handover operations to use an appropriate BS, which is exactly the focus of this thesis. Given this multiple BSs scenario, this thesis targets to design *proactive and data-driven mmWave communication systems*. The importance of proactiveness and data-driven-ness is elaborated as follows:

---

[5] More specifically, the two phones are separated by 1.2 m, and the human obstacle and either phone are separated by 0.60 m. The human obstacle blocks the LoS path between the phones for approximately 20 s. The height of the phones is approximately 1.0 m.

Proactiveness. Being different from the multiple beams, the usage of multiple BSs incurs more complicated procedure to finalize the handover such as association request or data forwarding. Accordingly, it involves service interruptions. If one can predict the blockage effects in a proactive manner, not only such blockage effects are completely avoided, but also the aforementioned complicated handover procedure can be completed beforehand, which gets rid of serious service interruptions incurred by handover. This finally prevents from deterring user experiences in data-intensive applications.

Data-driven-ness. As discussed above, throughput in non-LoS (NLoS) conditions depends on channel environments, and accordingly, the necessity of performing a handover also depends on the environments. In the aforementioned example, on the one hand, a handover should be performed in open outdoor spaces to avoid serious throughput degradation. On the other hand, a handover may not be preferable in a narrow corridor or an indoor room because satisfactory throughput may be maintained even without handovers. If one can learn such environment-specific factors from quantitative feedbacks such as received power, data rate, and throughput in a data-driven manner, he/she can determine more intelligent handover strategies involving the necessity of performing handovers.

To summarize, a proactive and data-driven mmWave communication system is a unified framework that provides extreme robustness against LoS blockages in heterogeneous environments towards various data-intensive applications. Namely, this framework possesses the following two characteristics. First, it integrates the blockage robustness of beam search mechanisms in indoor narrow spaces by standing on the shoulders of dedicated contributors for wireless personal/local area networks in the 2000s. Second, it also solves the LoS blockage problems in open areas that could not necessarily be solved only with beam search towards upcoming data-intensive applications. Hence, the insights provided in this thesis shed lights on great research opportunities to bring high-data-rate wireless communications everywhere, which gives a step forward to many data-intensive applications such as data streaming in wireless personal areas, monitoring in automated factories in indoor open spaces, and cooperative perception in V2X networks in outdoor areas.

1.2 Scope of This Thesis

Given the aforementioned philosophy, this thesis mainly focuses on the following research question: *how one can design such a proactive and data-driven mmWave communication systems?* The key idea to answer the question is to leverage visual data and machine learning (ML) techniques. Visual data involves spatio-temporal features of obstacles causing blockage effects that cannot be necessarily captured only by monitoring received powers in mmWave links. These features enables not only a binary prediction of whether blockage events occurs or not, but also a quantitative prediction of how serious the blockage effect is in terms of received powers, which facilitates an appropriate selection of deployed BSs. However, such essential features of obstacles' mobility is not explicit in visual image data because each image itself is no more than a large dimensional vector, and this mandates to extract the features from a feedback of radio frequency (RF) received powers. Moreover, to realize the idea of data-driven systems, one should associate visual data to quantitative feedbacks in mmWave communications. Hence, this thesis leverages machine learning techniques to form an appropriate prediction of future performances in BSs in a data-driven manner while extracting meaningful features form visual data to achieve such goals.

Particularly, the focus of this thesis is two-folds: First, this thesis demonstrates the feasibility of proactive handover via visual data-driven performance predictions based on deep reinforcement learning (RL). Second, in the ML-based visual-data-driven received power prediction, this thesis addresses the challenges to integrate received power data and visual data while collecting visual data in a communication-efficient and privacy preserving manner. The detailed introduction of these focuses are elaborated in the subsequent sections.

1.2.1 Visual Data-Driven Proactive Handover

This thesis first presents a paradigm shift for leveraging time-consecutive camera images in handover decision problems, which is provided in Chapter 4. While making handover decisions, it is important to predict future long-term performance—e.g., the cumulative sum of time-varying data rates—proactively to avoid making myopic decisions. However, this thesis experimentally notices that a time-variation in the received powers is not necessarily informative for proactively predicting the rapid degradation of data rates caused by moving obstacles.

To overcome this challenge, this thesis proposes a proactive framework wherein handover timing is optimized while obstacle-caused data rate degradations are predicted before the degradations occur. The key idea is to expand a state space to involve time-consecutive camera images, which comprises informative features for predicting such data rate degradations. To overcome the difficulty in handling the large dimensionality of the expanded state space, a deep RL is used to decide handover timing. The evaluations performed based on the experimentally obtained camera images and received powers demonstrate that the expanded state space facilitates (i) the prediction of obstacle-caused data rate degradations from 500 ms before the degradations occur and (ii) superior performance to a handover framework without the state space expansion.

1.2.2 Communication-Efficient and Privacy-Preserving Multimodal Received Power Prediction

As provided in Chapter 5, this thesis improves the accuracy of millimeter wave received power prediction by utilizing camera images and RF received powers, while gathering image inputs in a communication-efficient and privacy-preserving manner. To this end, this chapter proposes a distributed multimodal ML framework, coined *multimodal split learning (MultSL)*, in which a large neural network (NN) is split into two wirelessly connected segments. The upper segment combines images and received powers for future received power prediction, whereas the lower segment extracts features from camera images and compresses its output to reduce communication costs and privacy leakage. Experimental evaluation corroborates that MultSL achieves higher accuracy than the baselines utilizing either images or RF signals. Remarkably, without compromising accuracy, compressing the lower segment output by 16x yields 1/16 communication latency and 2.8% less privacy leakage compared to the case without compression.

1.3 Chapter Overview

The goal of this thesis is to demonstrate the feasibility of visual data-driven mmWave communication systems using ML techniques to enable proactive performance prediction against blockage effects. As shown in Fig. 1.2, the building blocks of this thesis are five-folds in a higher-level perspective: introduction, ML principles, experimental setting, visual-data-driven handover management, and multimodal received power prediction. The ML principles and experimental setting correspond to the methodological building blocks to achieve the aforementioned goal, which are detailed in Chapters 2 and 3, respectively. More specifically, Chapter 2 details the ML techniques leveraged in this thesis. Chapter 3 details the measurement system of RF received powers in an off-the-shelf 60 GHz wireless LAN (WLAN) access point (AP) being operated in a packet-mode transmission. This measurement system is leveraged to examine the visual data-driven mmWave communication systems in the subsequent chapters.

Chapters 4 and 5 mainly provide feasibility studies on visual data-driven mmWave communication systems from different point-of-views in terms of addressed problems. More specifically, Chapter 4 demonstrates the feasibility of proactive prediction on throughput performance of deployed BSs in a handover decision problem, and that of performing handover prior to blockage events. Note that this chapter also highlights that this characteristic is not necessarily obtained in a handover without visual data (i.e., only with RF received powers). To summarize, through the comparison between a handover with and without visual data, this chapter provides an in-depth insight into how visual data assist a network controller in determining hand-

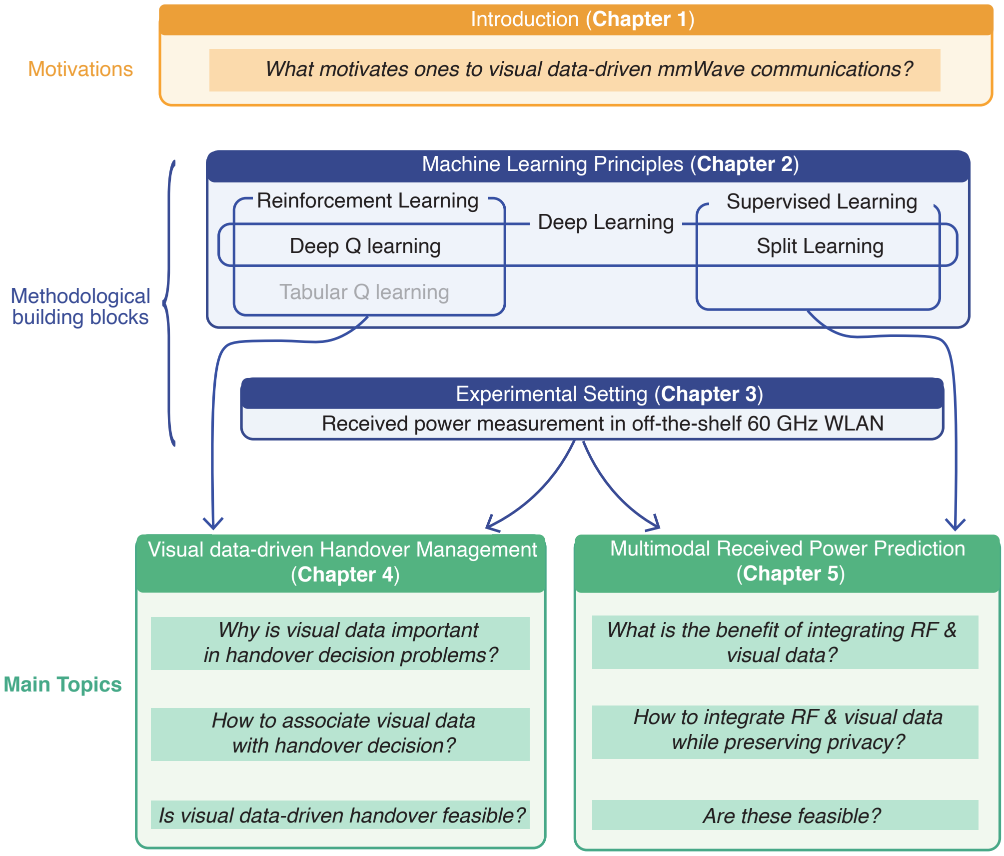

Figure 1.2: Chapter overview. The essential research questions addressed in this thesis are presented in the Italic font.

over strategies.

Chapter 5 mainly focuses on the following two research questions: 1) how to integrate multimodal data, i.e., visual data from multiple cameras and RF received powers, to enhance the performance of future received power; 2) how to collect visual data in a communication-efficient and privacy preserving manner. To this end, this chapter proposes MultSL, where a NN is split into two connected segments. The upper segment combines multiple images and received powers for future received power prediction, whereas the lower segment extracts features from camera images and compresses its output to reduce communication costs and privacy leakage.

1.4 Contributions

Regarding the RF received power measurement of mmWave links, the contributions of this thesis are as follows: First, this thesis answers how to capture RF received powers of mmWave signals transmitted by off-the-shelf WLAN access points operating in a packet-mode only using microwave spectrum analyzers and RF down converters. Therein, the frames are transmitted intermittently, and there is a challenge of estimating the duration where the frames are transmitted. To perform the estimation, this thesis applies two-state hidden Markov model (HMM). Second, the performed measurements are validated from a statistical perspective. More specifically, the measured duration in which the signal attenuates by 5 dB is consistent with the statistical model built in a previous report [11]. This measurement does not only provides an insight regarding the RF received power attenuation due to blockage events, but also could be used in the experiment of visual data-driven mmWave communication systems due to the capability of capturing time-series of the received power with a comparable frequencies to general camera frame rates (e.g., several tens frames per second).

Regarding the topic of the visual data-driven handover systems, the contributions of this thesis are twofold: First, via test-bed experiments using the aforementioned measurement sytems, this thesis highlights that the variation in the received powers before blockage events is not necessarily informative in predicting future data rate degradation in mmWave links. Accordingly, the handover framework without visual data, i.e., only with received power, triggers a handover in a reactive fashion and could not necessarily avoid blockage events in mmWave links. Second, motivated by this problem, this thesis proposes the proactive handover framework wherein handover timing is optimized while the degradation in data rate caused by obstacles is predicted within hundreds of milliseconds before degradation, being driven by visual data.

Regarding the topic of the multimodal received power prediction, the contributions of this thesis are twofolds: First, via test-bed experiments of mmWave received power prediction with measured channels and depth images, this thesis demonstrates the feasibility of benefitting from the aforementioned multimodal (i.e., visual and RF received power) data in privacy-preserving model training. Second, this thesis studies MultSL performance in terms of not just prediction accuracy, but also other metrics, i.e., communication efficiency and privacy levels. This yields a key insight that the prediction accuracy in MultSL does not necessarily trade-off with communication efficiency and privacy levels. To this end, this thesis provides the method to compress visual data towards communication efficiency and privacy, which is detailed in Chapter 5.

Chapter 2

Related Technologies: Machine Learning Principles

2.1 Supervised Learning

2.1.1 Problem Descriptions

The objective of supervised learning is to find a feasible hypothesis representing the relationship between input values and other values correlated with the input values [17–19]. Let the spaces of the input and the latter targeted values be denoted by $\mathcal{X}$ and $\mathcal{Y}$, respectively. Given observed data $(x_i, y_i)_{i \in \mathcal{I}}$, where $\mathcal{I}$ is the index set of the samples, $x_i \in \mathcal{X}$, and $y_i \in \mathcal{Y}$, $\forall i \in \mathcal{I}$, supervised learning outputs a hypothesis function $h : \mathcal{X} \to \mathcal{Y}$. The targeted values are generally called "label" in a supervised learning terminology, and this thesis follows this terminology, hereinafter.

Typically, as hypotheses, supervised learning uses parametric functions, and the problem falls into finding feasible parameters so that the resultant hypothesis becomes a good approximation of the relationship between input values and labels. Let $\boldsymbol{\theta}$ denote the parameters, and let $h_{\boldsymbol{\theta}}(x)$ denote the hypothesis with the parameter $\boldsymbol{\theta}$ that is generally called "model". Supervised learning is performed so that for every input value $x \in \mathcal{X}$ and label $y \in \mathcal{Y}$, the difference between $h_{\boldsymbol{\theta}}(x)$ and y becomes smaller as much as possible.

More technically, given available data set $(x_i, y_i)_{i \in \mathcal{I}}$, supervised learning minimizes the sum of measures showing sample-wise difference between $h_{\boldsymbol{\theta}}(x_i)$ and y_i. Let such a sample-wise difference metric be denoted by $l : \mathcal{Y} \times \mathcal{Y} \to \mathbb{R}$, which is generally called "per-sample loss function". This per-sample loss function is exemplified by the squared error, which is utilized to predict future received powers in mmWave links in Chapter 5 and is given by:

$$l(h_{\boldsymbol{\theta}}(x_i), y_i) = \|h_{\boldsymbol{\theta}}(x_i) - y_i\|^2. \tag{2.1}$$

Given a per-sample loss function l, the problem solved by supervised learning is summarized as:

$$\underset{\boldsymbol{\theta}}{\text{minimize}} \quad \frac{1}{|\mathcal{I}|} \sum_{i \in \mathcal{I}} l(h_{\boldsymbol{\theta}}(x_i), y_i). \tag{2.2}$$

In the optimization problem, the objective function is called "loss function". The subsequent section provides the algorithm to solve the optimization problem generally used in a supervised learning context.

2.1.2 Stochastic Gradient Descent

In supervised learning, to solve the problem (2.2), the stochastic gradient descent (SGD) algorithm [17] is generally utilized. The SGD algorithm is an variant of the well-known gradient descent (GD) algorithm, and hence, this section firstly introduces the GD algorithm. The GD algorithm iterates the parameter updates according to the gradients of the loss function. Denoting the parameters in the kth update as $\boldsymbol{\theta}^{(k)}$, the parameter update rule in the GD algorithm is given as:

$$\boldsymbol{\theta}^{(k+1)} = \boldsymbol{\theta}^{(k)} - \alpha_k \frac{1}{|\mathcal{I}|} \nabla_{\boldsymbol{\theta}} \sum_{i \in \mathcal{I}} l(h_{\boldsymbol{\theta}}(x_i), y_i), \tag{2.3}$$

where $\alpha_k \in [0, 1]$ is the learning rate in the kth update.

The key difference of the SGD algorithm from the GD algorithm is that in each parameter update, SGD algorithm calculates the gradient based on data sampled from the data set $(x_i, y_i)_{i \in \mathcal{I}}$ every parameter update, which is called "minibatch". Let the minibatch in the kth update be denoted by

$(x_m, y_m)_{m \in \mathcal{M}_k}$, where $\mathcal{M}_k \subseteq \mathcal{I}$, and the components of $\mathcal{M}_k$ are typically sampled from $\mathcal{I}$ in a random fashion. The parameter update rule in the SGD algorithm is given as:

$$\boldsymbol{\theta}^{(k+1)} \leftarrow \boldsymbol{\theta}^{(k)} - \alpha_k \frac{1}{|\mathcal{M}_k|} \nabla_{\boldsymbol{\theta}} \sum_{m \in \mathcal{M}_k} l(h_{\boldsymbol{\theta}}(x_m), y_m). \tag{2.4}$$

2.1.3 Feedforward Neural Network

The architecture of the model $h_{\boldsymbol{\theta}}$ is typified by feedforward NNs, which are applied to a large variety of supervised learning problems [17]. The feedforward NN is formed by a chain of multiple parametric functions called "layer" function, i.e., the model is given by [17]:

$$\begin{aligned} h_{\boldsymbol{\theta}} &= f^{(L)}_{\boldsymbol{\theta}^{(L)}}(o^{(L-1)}), \\ o^{(L-1)} &= f^{(L-1)}_{\boldsymbol{\theta}^{(L-1)}}(o^{(L-2)}), \\ &\vdots \\ o^{(1)} &= f^{(1)}_{\boldsymbol{\theta}^{(1)}}(x), \end{aligned}$$

where $f^{(l)}_{\boldsymbol{\theta}^{(l)}}(\cdot)$ denotes the lth layer for $l = 1, 2, \ldots, L$, and L is the layer size. In the above NN, $\boldsymbol{\theta}^{(l)}$ is the parameters of the lth layer. Note that in the above NN, $\boldsymbol{\theta}$ is the vector formed by all elements of $\boldsymbol{\theta}^{(1)}, \ldots, \boldsymbol{\theta}^{(L)}$.

Typically, the layer function consists of the sub-chain of a non-linear function called an "activation" function and a linear function. More specifically, the layer function is given by:

$$f^{(l)}_{\boldsymbol{\theta}^{(l)}} = g^{(l)}(f_{\mathrm{lin}, \boldsymbol{\theta}^{(l)}}(o)), \tag{2.5}$$

where o is the arbitrary input of the functions. In (2.5), $g(\cdot)$ and $f_{\mathrm{lin}, \boldsymbol{\theta}^{(l)}}(\cdot)$ correspond to the activation function and linear function, respectively. The activation function is typified by the rectified linear unit (ReLU) function, which is given by $\max\{0, o\}$ and is thoroughly applied to build models in this thesis.

Regarding the linear functions, one should choose an appropriate function according to the input structure, and this section limits the discussion specific to visual data processing. In the visual data processing, the linear function of the lower layers involves convolutional operation, which runs filtering process on input visual data. Therein, an appropriate filter is learned, and such layers are termed "convolutional layer". Contrary, as the linear function in the upper layers, e.g., the last two or three layers, the affine function that performs the multiplication of a matrix filled with non-zero values and addition of a non-zero vector termed bias is typically applied. This types of layer is also referred to as "dense layer". The overall structure of the NN comprising some convolutional layers is termed convolutional NN (CNN), and this thesis also leverages this thoroughly.

2.1.4 Split Learning

The privacy of data owners has been a huge concern in building large scale ML models [20]. As an ML task becomes complicated, the size of feedforward NN becomes larger, and the large volume of data is necessary to train such ML models [17]. For this reason, a cloud-centric model training becomes popular, wherein the cloud server holds the large size of feedforward NNs and collects training data from remote data owners. However, data owners are sometimes reluctant to upload raw data motivated by the concern for their privacy particularly when the data involves privacy sensitive information. Hence, many studies provide frameworks that train large scale ML models without requiring data owners to upload their raw data, which is comprehensively detailed in [21].

Split learning [22] is also a privacy-preserving framework that does not force data owners to share their raw data. The key idea behind the split learning is to divide such a large scale feedforward NN into multiple segments and to distribute the lower segments into data owners. In this setting, each data owner trains a partial feedforward NN up to a specific layer termed cut layer. The outputs at the cut layer are sent to a cloud-server which completes the rest of the training. This procedure prohibits data of each data owner from being exposed to a cloud-server, which contributes to preserving data privacy. This split learning is used in Chapter 5 to perform privacy-preserving model training in visual data-driven mmWave received power prediction.

2.2 Reinforcement Learning

2.2.1 Problem Descriptions

General RL algorithms are performed over an Markov Decision Process (MDP) [23, 24]. An MDP consists of the following four elements: a state space $\mathcal{S}$, an action space $\mathcal{A}$, a reward function $r : \mathcal{S} \times \mathcal{A} \times \mathcal{S} \to \mathbb{R}$, and transition probabilities $q : \mathcal{S} \times \mathcal{A} \to \Omega(\mathcal{S})$, where $\Omega(\mathcal{S})$ denotes the collection of the probability distribution over $\mathcal{S}$. At each decision epoch $t \in \mathbb{N}$, a decision maker observes the state information $s_t \in \mathcal{S}$. Subsequently, the decision maker selects an action on the basis of the *policy* $\pi : \mathcal{S} \to \mathcal{A}(s_t)$, where $\mathcal{A}(s_t) \subseteq \mathcal{A}$ denotes the set of possible actions when the state s_t is observed. Given the current state s_t and selected action $a_t \in \mathcal{A}(s_t)$, the state transitions to $s_{t+1} \in \mathcal{S}$ at the next decision epoch $t + 1$ according to the transition probability $q(s_{t+1}, s_t, a_t)$; thereafter, the decision maker is given a reward $r(s_{t+1}, a_t, s_t)$.

The objective of the decision maker is to determine the optimal policy $\pi^\star$ that maximizes the total expected discounted reward. The optimal policy satisfies the following condition:

$$\begin{aligned}\mathbb{E}&\left[\sum_{t'=0}^{\infty} \gamma^{t'} r\big(s_{t+t'+1}, \pi^\star(s_{t+t'}), s_{t+t'}\big) \,\middle|\, s_t = s\right] \\ &\qquad\qquad \geq \mathbb{E}\left[\sum_{t'=0}^{\infty} \gamma^{t'} r\big(s_{t+t'+1}, \pi(s_{t+t'}), s_{t+t'}\big) \,\middle|\, s_t = s\right], \end{aligned} \tag{2.6}$$

$\forall s \in S$ and $\forall \pi$, where $\gamma \in [0, 1)$ represents the discount factor. In the MDP wherein $\mathcal{S}$ and $\mathcal{A}$ are both countable non-empty sets, there exists at least one optimal policy [23].

To obtain the optimal policy in an MDP, it is sufficient to obtain the optimal action-value function $Q^\star : \mathcal{S} \times \mathcal{A} \to \mathbb{R}$. The optimal action-value function is defined as follows:

$$Q^\star(s, a) \coloneqq \mathbb{E}_{s'}[r(s', a, s) + \gamma V^\star(s') \,|\, s, a], \quad s \in \mathcal{S}, a \in \mathcal{A}(s), \tag{2.7}$$

where $\mathbb{E}_{s'}[\,\cdot\,|\, s, a\,]$ denotes the expectation operator under the transition probability $q(s', s, a)$, and $V^\star(s)$ denotes the left-hand side in (2.6). This is attributed to the fact that the optimal action-value function is related to the optimal policy as follows [23]:

$$\pi^\star(s) = \mathop{\arg\max}_{a \in \mathcal{A}(s)} Q^\star(s, a). \tag{2.8}$$

In other words, the policy that selects the action that maximizes $Q^\star(s, a)$ is optimal.

It should be noted that the optimal action-value function $Q^\star(s, a)$ satisfies the following Bellman optimal equation [23]:

$$\mathbb{E}_{s'}\left[r(s', a, s) + \gamma \max_{a' \in \mathcal{A}} Q^\star(s', a') - Q^\star(s, a) \,\middle|\, s, a \right] = 0, \tag{2.9}$$

$\forall s, a$, where $\mathbb{E}_{s'}[\cdot \mid s, a]$ denotes the expectation operator under the transition probability $q(s', s, a)$. Hence, the problem falls into searching for the functions that satisfy the Bellman equation. This is done by the algorithms that are detailed in the subsequent sections.

2.2.2 Tabular Q-Learning

To exactly solve the Bellman equation (2.9), and thereby achieve the optimal policy $\pi^\star$, the prior knowledge of $q(s', s, a)$ is required [23]. In the visual-data driven mmWave communication systems, $q(s', s, a)$ includes the transition probability of the visual data. However, in practical use, the prior knowledge of the transition probability might not be often obtained.

Hence, in handover decision problems, this thesis employs RL algorithms to learn the optimal action-value functions that satisfy the Bellman optimal equation (2.9). The RL algorithms enable for the agent to learn the optimal action-value functions via the interaction to the communication environment. Tabular Q-learning—one of the RL algorithms—enables for the network controller to learn the optimal action-value functions exactly [23], which provides a practical solution to achieve the optimal policy.

Tabular Q-learning is applicable to decision-making problems in which the elements of the state vector are discrete value, and learns the optimal action-value function by recursively updating a table filled with the estimated value of the optimal action-value function. Let $Q^{(k)}(s, a)$ denote the table of the estimated optimal action-value function in the kth update. In each decision epoch t, the agent faces to the state s_t and then takes an action a_t with a pre-defined policy. Then, the states transitions to s_{t+1} and the agent observes the reward $r_t \coloneqq r(s_{t+1}, a_t, s_t)$. Using the available information (s_{t+1}, a_t, s_t, r_t) the agent updates the estimator of the optimal action-value functions $\forall s \in \mathcal{S}, \forall a \in \mathcal{A}$ as follows:

$$Q^{(k+1)}(s,a) = \begin{cases} Q^{(k)}(s,a) + \beta\big(r_t + \gamma \quad \max_{a \in \mathcal{A}(s_{t+1})} Q^{(k)}(s_{t+1}, a) - Q^{(k)}(s,a)\big), \\ \qquad\qquad\qquad\qquad \text{if } s = s_t,\ a = a_t, \\ Q^{(k)}(s,a), \qquad\qquad \text{otherwise,} \end{cases} \tag{2.10}$$

where $\beta \in [0,1]$. Tabular Q-learning algorithm is summarized in Algorithm 2.1. Note that the RL algorithms learn the optimal policy based on the data sets $(s_{t+1}, a_t, s_t, r_t)_{t=1}^{T}$, where T denotes the number of elapsed time steps. This data set is called a replay buffer, and each data is called experience in an RL terminology, hence, the thesis follows this terminology.

However, the drawback of the tabular Q-learning is that it has to estimate all action-values $Q(s,a)$ for each state-action pair. This is infeasible in the usage of visual data because visual data, which is regarded as state, generally contains large dimensional information, which prohibits from filling the table of the action-values for each state-action pair.

2.2.3 Deep Q-Learning

One of the solutions to deal with the problem of the tabular Q-learning is to approximate the optimal action-value function by parametric functions $Q(s, a; \boldsymbol{\theta})$, where $\boldsymbol{\theta}$ denotes the parameters of the approximate functions, and then estimate feasible parameters which allow to achieve a good approximation of the optimal action-value functions. Deep Q-learning algorithm is one of the successful function approximation methods to achieve a feasible approximation of the optimal action-value functions [25]. Deep Q-learning algorithm approximates the optimal action-value functions by

Algorithm 2.1 Q-learning algorithm.

```
initialize: initialize estimator of the optimal action-value, $Q^{(0)}(s,a)$ $\forall s \in \mathcal{S}$, $\forall a \in \mathcal{A}$ arbitrarily
specify $\epsilon$, $\gamma$, and $\alpha$
observe an initial state $s_1$
for $t = 1, 2, \ldots, T$ do
    choose an action $a_t$ via pre-defined policy
    observe next state $s_{t+1}$ and reward $r_t$
    update the estimator of the optimal action-value according to (2.10)
end for
```

NNs—because of this, each approximate function is an NN and the parameter $\boldsymbol{\theta}$ is the weight vector of the NN—and trains the NN with the algorithm as discussed below.

In the deep Q-learning algorithm, the NN is trained so that the difference between $Q(s_t, a_t; \boldsymbol{\theta})$ and $r_t + \gamma \max_{a'} Q(s_{t+1}, a'; \boldsymbol{\theta})$ is minimized. This is motivated by the fact that such NNs roughly satisfy the Bellman equation, and hence, one can achieve a good approximation of the optimal action value function. To quantify the difference, one can typically leverage the following per-sample loss as an example:

$$\Big(Q(s_t, a_t; \boldsymbol{\theta}) - \Big(r_t + \gamma \max_{a' \in \mathcal{A}} Q\big(s_{t+1}, a'; \boldsymbol{\theta}_{\text{target}}\big)\Big)\Big)^2 \tag{2.11}$$

where, $Q\big(\cdot, \cdot; \boldsymbol{\theta}_{\text{target}}\big)$ is the proxy NN that is called "target network" and is updated once in a while to stabilize the training [25].

To minimize the loss function, one can apply the aforementioned SGD algorithm, which is a typical approach in the deep Q-learning [25]. Given the target network $Q\big(\cdot, \cdot; \boldsymbol{\theta}_{\text{target}}\big)$ and relay buffer $(s_{t+1}, a_t, s_t, r_t)_{t=1}^{T}$, the update rule of the NN weights are given by:

$$\begin{aligned} &\boldsymbol{\theta}^{(k+1)} = \\ &\boldsymbol{\theta}^{(k)} + \frac{1}{|\mathcal{T}'|} \alpha_k \nabla_{\boldsymbol{\theta}} \sum_{t' \in \mathcal{T}'} \Big(Q(s_{t'}, a_{t'}; \boldsymbol{\theta}) - \Big(r_{t'} + \gamma \max_{a' \in \mathcal{A}} Q\big(s_{t'+1}, a'; \boldsymbol{\theta}_{\text{target}}\big)\Big)\Big)^2, \end{aligned} \tag{2.12}$$

Algorithm 2.2 Deep Q-learning [25].

```
initialize: initialize NNs, $Q(s, a; \boldsymbol{\theta}^{(0)})$ and $Q(s, a; \boldsymbol{\theta}_{\text{target}})$, and replay memory $\mathcal{D}$
specify discount factor $\gamma$ and learning rate $\alpha$.
observe an initial state $s_1$
for $t = 1, 2, \ldots, T$ do
    choose action $a_t$ via pre-defined policy
    observe next state $s_{t+1}$ and reward $r_t$
    store transition $(s_t, a_t, r_t, s_{t+1})$ in $\mathcal{D}$
    sample experiences randomly from $\mathcal{D}$
    update parameter according to (2.12)
    every $C$ steps, update target NN
end for
```

where $\mathcal{T}' \subseteq \{1, 2, \ldots, T\}$ denotes the index set of the experience, which is randomly sampled from the replay buffer and corresponds to the indices of the minibatch in the supervised learning terminology. The weights of the target network is also updated when the SGD steps are performed for the pre-defined number of times. The deep Q-learning algorithm is summarized in Algorithm 2.2.

Chapter 3

Measurement Method of Temporal Attenuation by Human Body in Off-the-Shelf 60 GHz WLAN

3.1 Overview

As discussed in Chapter 1, a mmWave WLAN which leverages a channel bandwidth of over 2 GHz offers multi-gigabit data transfers, which attracts a lot of attention [26–29]. However, the mmWave WLAN experiences more signal attenuation induced by human blockage than WLANs that operate at the microwave band [30]. The attenuation is attributable to the use of higher directional antennas which are to compensate for a larger pass loss, and to propagation characteristics of mmWave [31].

To obtain a deeper insight into the impact of LoS blockages on mmWave links, measurements of the time-variant signal attenuation in the mmWave band have been conducted in many studies [9, 11–13, 31–34]. For example, the authors in [32] measured the attenuation in the 60 GHz band and then compared the results with a knife edge diffraction model where the human body is modeled by two cylinders. The authors in [11] measured statistical characteristics of the time duration in which the signal attenuates by 5 dB, the time duration in which the signal attenuation level recovers from 5 dB to 0 dB, and time duration in which the human blockage event continues. From these parameters, they built a piecewise linear model for the time series of the signal attenuation in the 60 GHz .

These measurements generally have employed horn antennas in a transmitter, while transmitters in mmWave WLANs employ consumer-grade array antennas to perform beamforming [29]. The authors in [30] revealed a significant difference between these two types of antennas in terms of directivity and side lobes. The difference between two types of antennas might give rise to the gap between the measurement results because antenna pattern of the transmitters gives an impact on the time series of signal attenuation [33]. For practical operation of mmWave WLANs, the gap should be investigated using a commercially available IEEE 802.11ad WLAN AP as a transmitter.

Being different from many measurements above where transmitters transmit continuous waves to receivers, the measurement of signals transmitted by an IEEE 802.11ad WLAN AP requires the estimation of whether the AP transmits signals or not at each sampling point in a sweep. This is due to the transmission mechanism of the AP. The AP transmits signals intermittently to a station (STA) according to medium access control protocols [6]. The durations in which the AP transmits a signal might be smaller than a sweep length, hence, in each sweep length, there exist both durations in which the AP transmitted signals and durations in which the AP did not. Thus, in order to temporally track the signal attenuation due to human blockage, it is required to classify the samples into those in the former durations and those in the latter durations.

This chapter conducts a measurement of time-varying signal attenuation induced by human blockage, involving a commercially available IEEE 802.11ad WLAN AP and STA while proposing the classification method of signal presences and absences. More specifically, the classification of whether signal is present or not at each sampling point is performed using a simple two-state hidden Markov model.

The contributions of this chapter are threefold:

- This chapter provides the classification method whether the AP trans-

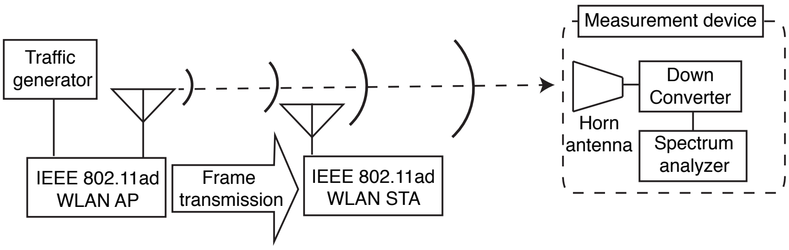

Figure 3.1: Block diagram of measurement system.

mitted frames or not at each sampling point using a simple two-state HMM.

- Applying a two-state HMM to data obtained when the AP does not transmit any signals causes model overfitting and consequent invalid power calculation. Thus, this chapter performs Bayesian information criterion (BIC)-based model selection. Therein, it is selected which two-state HMM or one-state model is more applicable to obtained data. Thereby, one can detect this kind of the data and prevent model overfitting.

- The measurements presented in this chapter are validated in terms of several statistical characteristics. More specifically, this chapter confirms that the duration in which the signal attenuates by 5 dB is consistent with the statistical model built in a previous report, and that the range of the duration in which the signal attenuation decreases from 5 dB to 0 dB is similar to that in the report.

The rest of this chapter is organized as follows. Section 3.2 presents the architecture of the measurement system in detail. Section 3.3 presents the method to obtain the time-varying attenuation, involving an estimation of whether the AP transmitted a frame or not using HMM. Section 3.4 shows the measurement results. Section 3.5 concludes the present chapter.

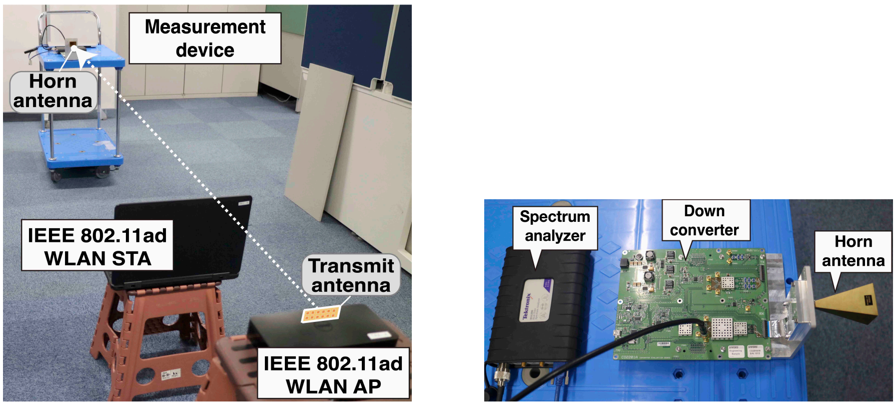

(a) Measurement system. (b) Measurement device.

Figure 3.2: Measurement system and device.

3.2 Measurement Setup

Fig. 3.1 shows the measurement system. The horn antenna receives RF signals at 60.48 GHz, which antenna is affixed to a waveguide flange input on the down converter. Then, the down converter converts the RF signal to a baseband signal. The microwave spectrum analyzer filters I-channel components of the baseband signal at the center frequency of 100 MHz with a bandwidth of 10 MHz. These signals are then sampled by an A/D converter in a spectrum analyzer. Figs. 3.2(a) and 3.2(b) show pictures of the measurement system and the measurement device, respectively. Details regarding the measurement equipment and the measurement parameters are shown in Tables 3.1 and 3.2, respectively.

Note that the choice of the bandwidth, which is smaller than the IEEE 802.11ad WLAN channels, is attributed to the time resolution in which the signal attenuation is obtained. In order to show the consistency in the time duration in which signal attenuates by 5 dB and thereby to validate the presented measurement method, the time resolution of tens of milliseconds is required—the time duration is reported to have the value of tens of milliseconds in the reference [11]—. Because there is a trade-off between the acquisition bandwidth and the time resolution—a wider acquisition bandwidth sacrifices the time resolution—, the measurement in a smaller bandwidth than the IEEE 802.11ad WLAN channel bandwidth was conducted. In

Table 3.1: Measurement equipment.

IEEE 802.11ad WLAN AP	Dell®Wireless Dock D5000
IEEE 802.11ad WLAN STA	Dell®Latitude E5540
Client laptop	Dell®Latitude E5540
Wired network	1000BASE-T Gigabit Ethernet
Microwave spectrum analyzer	Tektronix®RSA306
Down converter	Sivers®IMA FC2221V
Anntena	Sivers®IMA Horn anntena, 24 dBi

the measurement system, the measurement bandwidth of 10 MHz allowed to obtain the temporal signal attenuation in a time resolution of around 20 ms.

The measurement was conducted under the condition that the AP transmits data frames to the STA as shown in Fig. 3.1. The frame transmission was done by generating uplink traffic from the laptop connected to the AP with a gigabit ethernet cable. The traffic was generated by Iperf3 [16].

For the sake of clarity of the discussion in the following sections, the signal representation is introduced here. Let $r(t)$ be the representation of I-channel components of the 11ad WLAN signal converted by the down converter and $b(t)$ be the impulse response of the acquisition bandpass filter in the spectrum analyzer. Then, the signal which is to be sampled by the A/D converter in the spectrum analyzer is represented by $y(t) = (r(t) + n(t)) * b(t)$, where $n(t)$ is the noise inherent in the measurement device, and the $*$ represents the convolution of two functions. Note that $r(t)$ is equivalent to 0 when the AP does not transmit any frames.

Table 3.2: Measurement parameters.

Channel	60.48 GHz
Sampling frequency $1/T$	14 MHz
Receive antenna gain	24 dBi
Acquisition bandwidth	10 MHz
Number of samples per sampling K	2800

3.3 Measurement Method of Temporal Signal Attenuation

3.3.1 Overview

Let the vector which identifies whether the AP transmits frames or not be denoted by $\boldsymbol{z}(t) = [z_0(t), z_1(t)]^{\mathrm{T}}$, which is defined as

$$\boldsymbol{z}(t) := \begin{cases} [0,1]^{\mathrm{T}} & \text{if the AP transmits a frame,} \\ [1,0]^{\mathrm{T}} & \text{otherwise.} \end{cases} \tag{3.1}$$

Let $\mathcal{D}$ be the union of disjoint time intervals when the AP transmits frames, defined as

$$\mathcal{D} := \{\, t \mid z_1(t) = 1 \,\}. \tag{3.2}$$

Let $\mathcal{D}(t_m) := \mathcal{D} \cap [t_m, t_m + KT]$ be the time duration when the AP transmitted frames in the sampling window $[t_m, t_m + KT]$, where t_m denotes the time at which the analyzer starts the mth sweep; while K and T denote the number of samples and the sampling period, respectively, therefore, $t_m + KT$ denotes the time at which the analyzer ends the sweep. The timing of sweeps is depicted in Fig. 3.3. Note that the time length KT for which the analyzer sweeps —it is 200 μs in the measurements—is shorter than the interval $t_{m+1} - t_m$ between successive sweeps—it is 20 ms—.

The goal is to obtain the time-dependent attenuation value $A(t_m)$ given by

$$A(t_m) = \frac{P(t_m)}{P(t_1)}, \tag{3.3}$$

where $P(t_m)$ is the mean power of the measured signal, given by

$$P(t_m) = \frac{\int_{D(t_m)} |y(t)|^2 \, \mathrm{d}t}{\int_{D(t_m)} \mathrm{d}t}, \tag{3.4}$$

i.e., the mean value of the power samples $p_m[k_m] \coloneqq |y(t_m + k_m T)|^2$ for $k_m \in \{1, \ldots, K\}$ taken only if $z_1(t_m + k_m T) = 1$. $P(t_m)$ for $m > 1$ is obtained in the possible presence of human bodies; while $P(t_1)$ is obtained in the absence of human bodies and is the reference used to compute the attenuation $A(t_m)$.

The attenuation values $A(t_m)$ are calculated by three steps: the BIC-based model selection, the HMM-based frame transmission state estimation, and averaging. First, BIC-based model selection decides which a two-state HMM or a one-state model is more appropriate to be applied to the obtained data $\boldsymbol{p}_m = (p_m[1], \ldots, p_m[K])^{\mathrm{T}}$. Only when the two-state HMM is selected, the HMM-based frame transmission state estimation is conducted. Then, it is estimated whether $z_1(t_m + k_m T) = 1$ or not for $k_m \in \{1, \ldots, K\}$, i.e., whether the AP transmitted frames or not at each sampling point. Finally, the average of $p_m[k_m]$ is calculated for k_m that is estimated to be $z_1(t_m + k_m T) = 1$.

3.3.2 HMM-Based Frame Transmission State Estimation

HMM-Based Estimation Scheme

Let $\boldsymbol{z}_m[k_m] = [z_{m,0}[k_m], z_{m,1}[k_m]]^{\mathrm{T}}$ denote $\boldsymbol{z}(t_m + k_m T)$. The main purpose of this section is to decide whether $z_{m,1}[k_m] = 1$ or not for $k_m \in \{1, \ldots, K\}$. The decision is based on modeling the power observations $p_m[k_m]$ using a two state HMM. This section now considers that the two-state HMM is selected in the BIC-based model selection in advance. The model selection is discussed in the subsequent section.

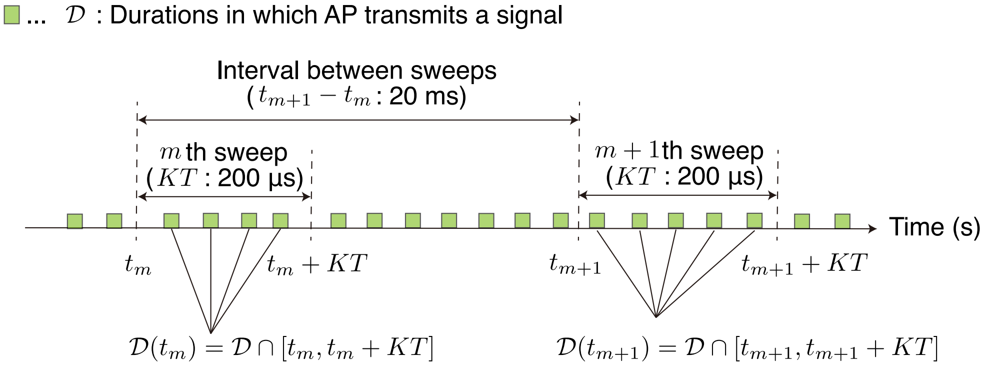

Figure 3.3: Timing of sweeps.

An HMM is a statistical model that forms a sequence of observations whose distribution depends on a latent variable that follows a Markov chain. The value $\boldsymbol{z}_m[k_m]$ is regarded as the latent variable which the distribution of $p_m[k_m]$ depends on. Hereinafter, this chapter refers to the event that $z_{m,1}[k_m] = 1$ as *frame transmission state*; the phenomenon that $z_{m,1}[k_m] = 0$ as *pausing state*. This chapter assumes that the distribution conditioned on $\boldsymbol{z}_m[k_m]$ is an exponential distribution, thus, the probability density functions of $p_m[k_m]$ conditioned on $\boldsymbol{z}_m[k_m]$ is given as follows:

$$\begin{aligned} p(p_m[k_m] \mid z_{m,0}[k_m] = 1) &= \lambda_0 \exp\left(-\lambda_0 p_m[k_m]\right), \\ p(p_m[k_m] \mid z_{m,1}[k_m] = 1) &= \lambda_1 \exp\left(-\lambda_1 p_m[k_m]\right), \end{aligned} \tag{3.5}$$

where $\lambda_{i_{\text{state}}}$ for $i_{\text{state}} \in \{0, 1\}$ denotes the parameter of the exponential distribution when $z_{m,i_{\text{state}}}[k_m] = 1$. The assumption is validated by the experimental results.

The most likely sequence of the latent variables is estimated utilizing Viterbi algorithm. Viterbi algorithm requires the parameters of the HMM which include $\lambda_{i_{\text{state}}}$, transition probabilities, and initial state probabilities. Because of the lack of the knowledge of the true parameters, the most likely parameters is estimated using expectation maximization (EM) algorithm beforehand. Each algorithm is described in detail as follows.

Parameter Estimation

This section estimates the parameters of the HMM given by $\boldsymbol{\theta}_{\mathrm{HMM}} = [\lambda_0, \lambda_1, q_{0,0}, q_{0,1}, q_{1,0}, q_{1,1}, \pi_{\mathrm{init},0}, \pi_{\mathrm{init},1}]^{\mathrm{T}}$, where $q_{i_{\mathrm{state}}, j_{\mathrm{state}}}$ for $i_{\mathrm{state}} \in \{0, 1\}$ and $j_{\mathrm{state}} \in \{0, 1\}$ represents the transition probability of a latent variable that is defined as $\mathbb{P}(z_{m, j_{\mathrm{state}}}[k_m + 1] = 1 \mid z_{m, i_{\mathrm{state}}}[k_m] = 1)$; $\pi_{i_{\mathrm{state}}}$ represents the initial state probability that is defined as $\mathbb{P}(z_{m, i_{\mathrm{state}}}[1] = 1)$. To avoid the complicated notations , this section omits the subscript "state" in i_{state} and j_{state}.

The estimation utilizes EM algorithm [19]. The EM algorithm derives the estimator $\hat{\boldsymbol{\theta}}_{\mathrm{HMM}}$ maximizing a likelihood $p(\boldsymbol{p}_m \mid \boldsymbol{\theta}_{\mathrm{HMM}})$ via the iteration of E-step and M-step. The E-step derives the expectation of $\ln p(\boldsymbol{p}_m, \boldsymbol{Z}_m \mid \boldsymbol{\theta}_{\mathrm{HMM}})$ under the posterior distribution of $\boldsymbol{Z}_m := [\boldsymbol{z}_m[1], \dots, \boldsymbol{z}_m[K]]$ and a current estimator:

$$\boldsymbol{\theta}^{(n)}_{\mathrm{HMM}} = \left[\lambda^{(n)}_0, \lambda^{(n)}_1, q^{(n)}_{0,0}, q^{(n)}_{0,1}, q^{(n)}_{1,0}, q^{(n)}_{1,1}, \pi^{(n)}_{\mathrm{init},0}, \pi^{(n)}_{\mathrm{init},1}\right]^{\mathrm{T}}, \tag{3.6}$$

where n is an iteration number. The M-step derives the estimator:

$$\boldsymbol{\theta}^{(n+1)}_{\mathrm{HMM}} = \left[\lambda^{(n+1)}_0, \lambda^{(n+1)}_1, q^{(n+1)}_{0,0}, q^{(n+1)}_{0,1}, q^{(n+1)}_{1,0}, q^{(n+1)}_{1,1}, \pi^{(n+1)}_0, \pi^{(n+1)}_1\right]^{\mathrm{T}}, \tag{3.7}$$

which maximizes the expectation. Details of each step are described in later. The iteration is guaranteed to converge to the locally optimal estimator $\hat{\boldsymbol{\theta}}_{\mathrm{HMM}}$ [19].

The goal of the E-step is to derive the expectation of $\ln p(\boldsymbol{p}_m, \boldsymbol{Z}_m \mid \boldsymbol{\theta}_{\mathrm{HMM}})$ under the posterior distribution of $\boldsymbol{Z}_m$ given $\boldsymbol{p}_m$ and the current estimator $\boldsymbol{\theta}^{(n)}_{\mathrm{HMM}}$. Let the expectation be denoted by $Q(\boldsymbol{\theta}_{\mathrm{HMM}}, \boldsymbol{\theta}^{(n)}_{\mathrm{HMM}})$, which is described as follows:

$$\begin{aligned} Q\left(\boldsymbol{\theta}_{\mathrm{HMM}}, \boldsymbol{\theta}^{(n)}_{\mathrm{HMM}}\right) &:= \mathbb{E}_{\boldsymbol{Z}_m}\left[\ln p(\boldsymbol{p}_m, \boldsymbol{Z}_m \mid \boldsymbol{\theta}_{\mathrm{HMM}}) \,\middle|\, \boldsymbol{p}_m, \boldsymbol{\theta}^{(n)}\right] \\ &= \sum_{\boldsymbol{Z}_m} p\left(\boldsymbol{Z}_m \,\middle|\, \boldsymbol{p}_m, \boldsymbol{\theta}^{(n)}_{\mathrm{HMM}}\right) \cdot \ln p(\boldsymbol{p}_m, \boldsymbol{Z}_m \mid \boldsymbol{\theta}_{\mathrm{HMM}}). \end{aligned} \tag{3.8}$$

As in [19], the expectation is given as follows:

$$\begin{aligned}
&Q\Big(\boldsymbol{\theta}_{\mathrm{HMM}}, \boldsymbol{\theta}_{\mathrm{HMM}}^{(n)}\Big) \\
&\quad= \sum_{i=0}^{1} \gamma(z_{m,i}[1]) \cdot \ln \pi_{\mathrm{init},i} \\
&\qquad+ \sum_{k_m=2}^{K} \sum_{j=0}^{1} \sum_{i=0}^{1} \xi(z_{m,j}[k_m-1], z_{m,i}[k_m]) \cdot \ln q_{j,i} \\
&\qquad+ \sum_{k_m=1}^{K} \sum_{i=0}^{1} \gamma(z_{m,i}[k_m]) \cdot \ln p\Big(p_m[k_m] \,\Big|\, z_{m,i}[k_m]=1, \boldsymbol{\theta}_{\mathrm{HMM}}^{(n)}\Big),
\end{aligned} \tag{3.9}$$

where

$$\begin{aligned}
\gamma(z_{m,i}[k_m]) &:= \mathbb{E}_{\boldsymbol{z}_m[k_m]}\Big[z_{m,i}[k_m] \,\Big|\, \boldsymbol{p}_m, \boldsymbol{\theta}_{\mathrm{HMM}}^{(n)}\Big] \\
&= \sum_{\boldsymbol{z}_m[k_m]} z_{m,i}[k_m] \cdot p\left(\boldsymbol{z}_m[k_m] \,\Big|\, \boldsymbol{p}_m, \boldsymbol{\theta}_{\mathrm{HMM}}^{(n)}\right),
\end{aligned} \tag{3.10}$$

$$\begin{aligned}
&\xi(z_{m,j}[k_m-1], z_{m,i}[k_m]) \\
&\quad:= \mathbb{E}_{\boldsymbol{z}_m[k], \boldsymbol{z}_m[k-1]}\Big[z_{m,j}[k_m-1] \cdot z_{m,i}[k] \,\Big|\, \boldsymbol{p}_m, \boldsymbol{\theta}_{\mathrm{HMM}}^{(n)}\Big] \\
&\quad= \sum_{\boldsymbol{z}_m[k_m-1]} \sum_{\boldsymbol{z}_m[k_m]} z_{m,j}[k_m-1] \cdot z_{m,i}[k_m] \\
&\qquad\quad \cdot p\left(\boldsymbol{z}_m[k_m-1], \boldsymbol{z}_m[k_m] \,\Big|\, \boldsymbol{p}_m, \boldsymbol{\theta}_{\mathrm{HMM}}^{(n)}\right).
\end{aligned} \tag{3.11}$$

These expectations; $\gamma(z_{m,i}[k_m])$ and $\xi(z_{m,j}[k_m-1], z_{m,i}[k_m])$ are derived via the forward-backward algorithm [19].

The M-step derives the revised estimator $\boldsymbol{\theta}_{\mathrm{HMM}}^{(n+1)}$ that maximizes $Q(\boldsymbol{\theta}_{\mathrm{HMM}}, \boldsymbol{\theta}_{\mathrm{HMM}}^{(n)})$, i.e., that satisfies

$$\boldsymbol{\theta}_{\mathrm{HMM}}^{(n+1)} = \underset{\boldsymbol{\theta}_{\mathrm{HMM}}}{\arg\max}\, Q(\boldsymbol{\theta}_{\mathrm{HMM}}, \boldsymbol{\theta}_{\mathrm{HMM}}^{(n)}). \tag{3.12}$$

The maximization with respect to $\pi_{\mathrm{init},i}$, $q_{i,j}$ $\forall i, j$ is achieved using appropriate Lagrange multipliers with the results [19]:

$$\pi_{\text{init},i}^{(n+1)} = \frac{\gamma(z_{m,i}[1])}{\sum_{j=0}^{1} \gamma(z_{m,j}[1])}, \tag{3.13}$$

$$q_{j,i}^{(n+1)} = \frac{\sum_{k_m=2}^{K} \xi(z_{m,j}[k_m-1], z_{m,i}[k_m])}{\sum_{i=0}^{1} \sum_{k_m=2}^{K} \xi(z_{m,j}[k_m-1], z_{m,i}[k_m])}. \tag{3.14}$$

The maximization with respect to λ_i for $\forall i$ is achieved via partial derivative with respect to λ_i, which result in

$$\lambda_i^{(n+1)} = \frac{\sum_{k_m=1}^{K} \gamma(z_{m,i}[k_m])}{\sum_{k_m=1}^{K} p_m[k_m] \gamma(z_{m,i}[k_m])}. \tag{3.15}$$

These steps are iterated until the convergence condition, $|Q(\boldsymbol{\theta}^{(n+1)}, \boldsymbol{\theta}_{\text{HMM}}^{(n)}) - Q(\boldsymbol{\theta}_{\text{HMM}}^{(n)}, \boldsymbol{\theta}^{(n-1)})| < \epsilon_0$ is satisfied, where ϵ_0 is the predefined tolerance. This chapter sets the tolerance to be 10^{-2}, which is much smaller than the likelihoods that have a value of the order of 10^5 in these experiments.

Estimation of Sequence of Latent Variables

The goal to estimate the most likely sequence of latent variables is achieved via Viterbi algorithm. The Viterbi algorithm seeks for the sequence of latent variables $\hat{\boldsymbol{Z}}_m$ which is described as

$$\hat{\boldsymbol{Z}}_m = \arg\max_{\boldsymbol{Z}_m} p(\boldsymbol{p}_m, \boldsymbol{Z}_m \,|\, \hat{\boldsymbol{\theta}}_{\text{HMM}}). \tag{3.16}$$

The Viterbi algorithm in the HMM works as maximum likelihood detection of convolutional codes [35]. Consider the trellis diagram where for all values k_m, all possible latent variables in the k_mth sampling point are deployed as the nodes at the trellis depth k_m and all the nodes at the trellis depth k_m is connected to all the nodes at the trellis depth $k_m + 1$. $\hat{\boldsymbol{Z}}_m = [\hat{\boldsymbol{z}}_m[1], \ldots, \hat{\boldsymbol{z}}_m[K]]$ is achieved by seeking for the trellis path maximizing path metric, defining the branch metric from the $(i+1)$th node at the depth k_m to the $(j+1)$th node at the depth $k_m + 1$, $B_{k_m}^{(i \to j)}$ as the following;

$$\begin{aligned} B_{k_m}^{(i \to j)} &= \ln\{p(\boldsymbol{z}_{m,j}[k_m+1] = 1 \,|\, \boldsymbol{z}_{m,i}[k_m] = 1, \hat{\boldsymbol{\theta}}_{\text{HMM}}) \\ &\qquad \cdot p(p_m[k_m+1] \,|\, \boldsymbol{z}_{m,j}[k_m+1] = 1, \hat{\boldsymbol{\theta}}_{\text{HMM}})\}. \end{aligned} \tag{3.17}$$

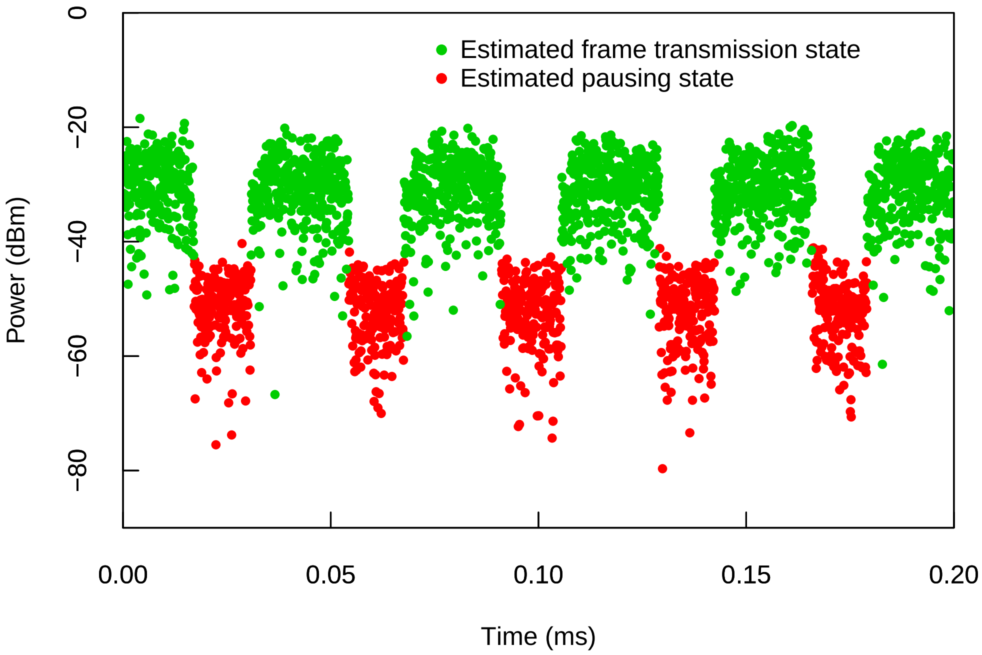

Figure 3.4: Example of the estimate of whether the AP transmitted frames or not.

Model Verification

This section shows that the Viterbi algorithm can estimate latent variables in each sampling point. Using the results, this section validates the assumption that $p_m[k_m]$ in each state follows the exponential distribution.

Fig. 3.4 shows an example of the estimation of latent variables. This shows that each latent variable is consecutive for a certain duration. This result agrees with the fact that the AP transmits a frame in a certain duration; from the start of transmission to the end.

Fig. 3.5 shows the cumulative frequencies of $p_m[k_m]$ in each estimated state and theoretical cumulative distribution function (CDF) of each exponential distribution. The parameter of each exponential distribution are estimated via EM algorithm. This figure shows that the distribution of

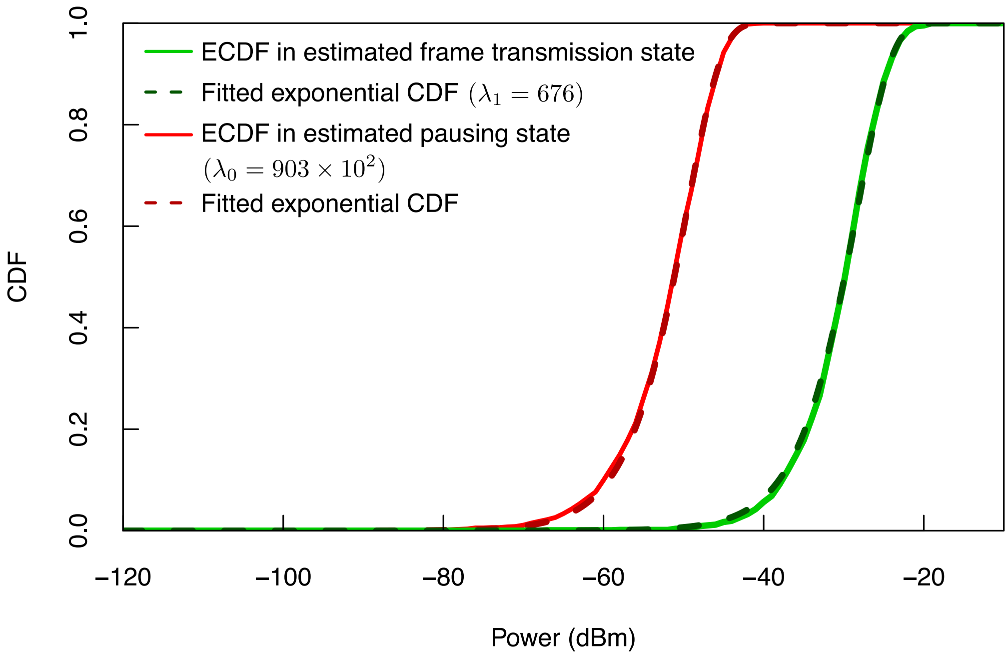

Figure 3.5: Cumulative frequencies of power observations in each state and CDF of fitted exponential distributions.

$p_m[k_m]$ in each state coincides with the theoretical CDF, which also shows the validity of the assumption that $p_m[k_m]$ in each state follows the exponential distribution.

3.3.3 BIC-Based Model Selection

The previous subsection considered that fitting the data using a two-state model is more appropriate than using a one-state model. However, there exists data in which no frames are observed because the AP did not transmit any frames for the time duration of $[t_m, t_m + KT]$.[1] In this case, applying a one-state model, where $p_m[k_m]$ follows an identical exponential distribution, is more appropriate because applying a two-state model causes model overfitting and consequent invalid calculation of $A(t_m)$. If a two-state HMM

---

[1] As an alternative approach, one can set the sampling rate and the number of samples per sweep so that at least one beacon signal is received. Note that the beacon interval of the employed AP is 1.1 ms [11].

is applied in this case, there exists $k_m \in \{1, \ldots, K\}$ for which $\hat{z}_{m,1}[k] = 1$ although the truth is that $\hat{z}_{m,1}[k_m] = 0 \ \forall k_m \in \{1, \ldots, K\}$. Thus, it is required that which model to be appropriate is decided and that if the one-state model is estimated to be appropriate, it is decided that $A(T_m)$ is not calculated.

To decide which model to be appropriate, BIC [19] is utilized. The BIC is given as follows:

$$\mathrm{BIC} = -L(\hat{\boldsymbol{\theta}}_{\mathrm{HMM}}) + \frac{d_{\mathrm{param}}}{2} \ln K, \tag{3.18}$$

where $L(\cdot)$ denotes the log-likelihood function and d_{param} is the number of parameters that is required to describe each model. In the two-state HMM, $d_{\mathrm{param}} = 5$, that is, the parameters are λ_0, λ_1, $q_{0,0}$, $q_{1,0}$, $\pi_{\mathrm{init},0}$. Note that $q_{0,1}$, $q_{1,1}$ and $\pi_{\mathrm{init},1}$ are not counted because these parameters are decided deterministically from $q_{0,0}$, $q_{1,0}$, and π_0, respectively. In the one-state model, $d_{\mathrm{param}} = 1$. $\hat{\boldsymbol{\theta}}_{\mathrm{HMM}}$ is the vector containing the model parameters with maximum likelihood. The model whose BIC is smaller than that of the counterpart is applied.

The second term of BIC is interpreted as the penalty of increasing the number of model parameters. The penalty of the BIC is more than that of the Akaike information criterion (AIC) [36], which is a reason why BIC is applied. BIC tends not to select the two-state model which has more parameters, and therefore prevents from model overfitting.

3.3.4 Procedure of Calculating Time-varying Signal Attenuation

The procedure of the calculation of $A(t_m)$ is summarized in Algorithm 3.1. First, the BIC of each model is cumputed. The BIC of the one-state exponential distribution model, BIC_1 is calculated via maximum likelihood estimation; that of the two-state HMM, BIC_2 is calculated via EM algorithm. If $\mathrm{BIC}_2 < \mathrm{BIC}_1$, Viterbi algorithm is conducted to estimate the latent variables and then $A(t_m)$ is calculated by averaging $p_m[k]$ in frame transmission state. If not, it is decided that the calculation of $A(t_m)$ is not conducted because the AP did not transmit any frames.

Algorithm 3.1 Procedure for measuring temporal signal attenuation in mmWave WLAN.

```
input: power observations $\boldsymbol{P} = (\boldsymbol{p}_1, \dots, \boldsymbol{p}_M)$
output: time series of signal attenuation $(A(t_1), \dots, A(t_M))^{\mathrm{T}}$
for $m \in \{1, \dots, M\}$ do
    conduct maximum likelihood estimation of a one-state exponential distribution model and calculate BIC, $\mathrm{BIC}_1$
    conduct EM algorithm in a two-state HMM and compute BIC, $\mathrm{BIC}_2$
    if $\mathrm{BIC}_2 < \mathrm{BIC}_1$ then
        estimation of the maximum-likely latent variables $\hat{\boldsymbol{Z}}_m$ using Viterbi algorithm
        $P_m \leftarrow$ average of $p_m[k_m]$ for $\forall k_m \in \{\, k \in \{1, \dots, K\} \mid \hat{z}_{m,1}[k] = 1\,\}$
        $A(t_m) \leftarrow P_m / P_1$
    end if
end for
```

3.4 Measurement of Time-Varying Attenuation in IEEE 802.11ad WLAN

3.4.1 Objective

The main objective of the measurements is to validate the measurement method by demonstrating the consistency in quantities associated with the signal attenuation under a similar condition to that in the previous report [11]; additional measurements in other conditions are out-of-scope. As in [11], the following values are measured: the duration $t_{\mathrm{decay,5\,dB}}$ in which signal attenuation level increases from 0 dB to 5 dB, the duration $t_{\mathrm{rise,5\,dB}}$ in which signal attenuation level decreases from 5 dB to 0 dB, and the mean signal attenuation A_{mean} in the interval $[t_{\mathrm{b}} + (t_{\mathrm{e}} - t_{\mathrm{b}})/3, t_{\mathrm{e}} - (t_{\mathrm{e}} - t_{\mathrm{b}})/3]$. Therein, t_{b} and t_{e} represent, respectively, the last zero crossing time before a shadowing event and the first zero crossing time after the shadowing event.

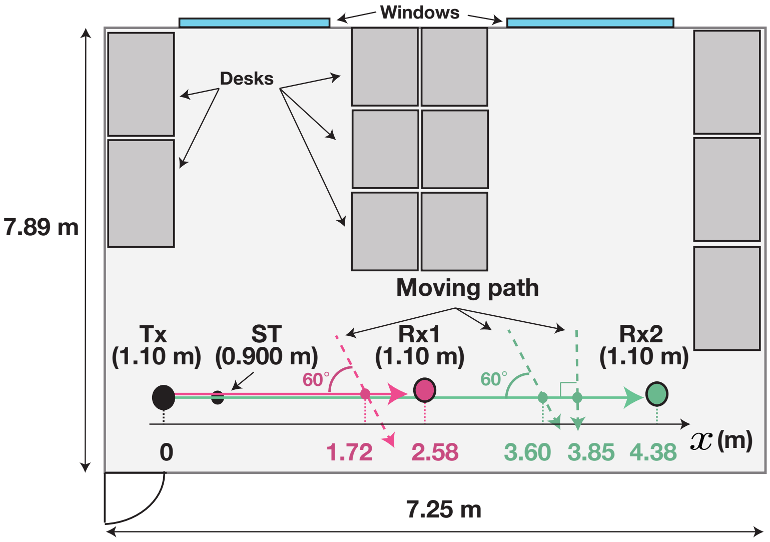

Figure 3.6: Top view of measurement environment with the moving path and positions of the AP, STA, and measurement device, denoted by TX, ST and RX1 or RX2, respectively. Values in parentheses indicate the height of each device.

3.4.2 Experiment Description

The measurements were conducted in a similar experimental scenario to the previous report [11] in order to compare the results with the results in the report. The moving paths of the pedestrian were kept fixed as in Fig. 3.6, which are similar moving paths to those in the report.

Fig. 3.6 also depicts the deployment of the measurement equipment. The AP and STA were kept fixed at the position TX and ST, whereas the measurement device was placed at the positions, RX1 and RX2. The separation distances between TX and RX1 and between TX and RX2 were 2.58 m and 4.38 m, respectively. The height of the AP and the measurement device was 1.10 m; that of the STA was 0.90 m.

3.4.3 Experimental Results

Fig. 3.7 shows an example of the time series of measured signal attenuation induced by human blockage. The signal attenuation level oscillates by up

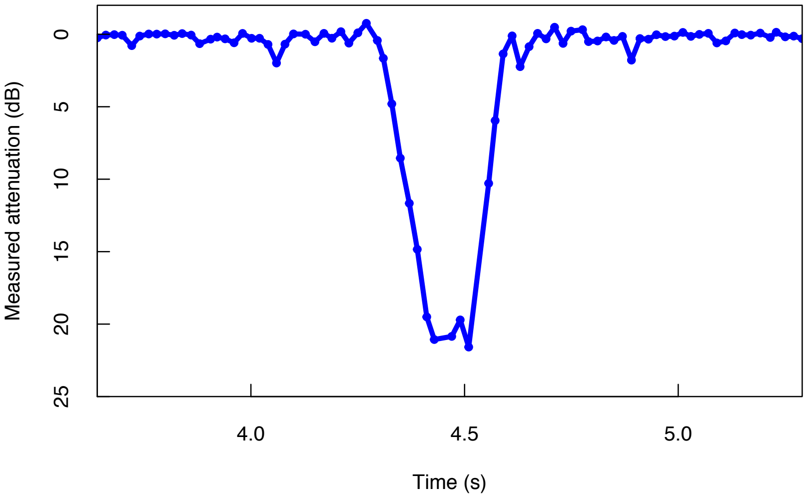

s

Figure 3.7: Time series of measured attenuation of signal transmitted by IEEE 802.11ad AP induced by human blockage.

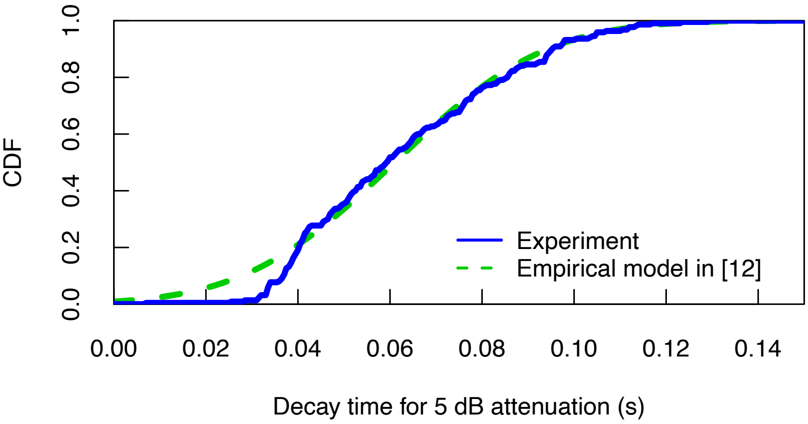

Figure 3.8: CDF of decay time for 5 dB attenuation, $t_{\mathrm{decay,5\,dB}}$.

to 2 dB before and after the signal attenuates. This is in agreement with a knife edge diffraction theory [37].

Fig. 3.8 shows the CDF of the decay time $t_{\mathrm{decay,5\,dB}}$. The empirical model in [11] is the Gaussian distribution with the mean of 0.061 s and the standard deviation of 0.026 s. The measured cumulative frequency of $t_{\mathrm{decay,5\,dB}}$ coincides with the model. In fact, the model cannot be rejected by the Kolmogorov-Sminov test [38] with a significance level of 1%. Thus, in

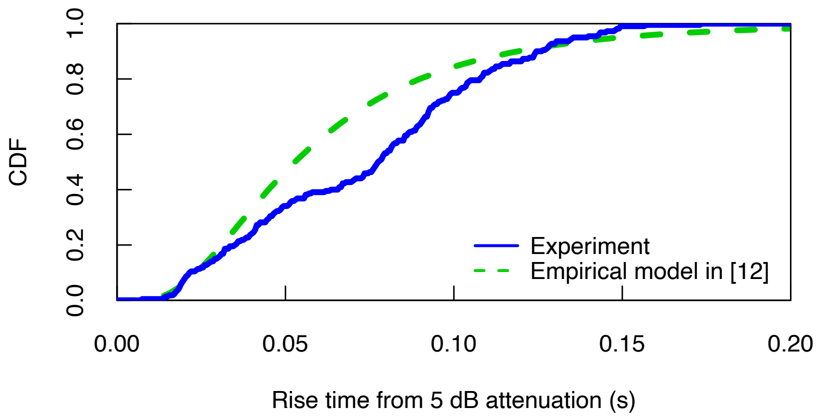

Figure 3.9: CDF of rise time from 5 dB attenuation, $t_{\mathrm{rise,5\,dB}}$.

terms of the decay time $t_{\mathrm{decay,5\,dB}}$, the empirical model is valid for the IEEE 802.11ad WLAN signals transmitted by a commercially available AP with a consumer-grade array antenna as well as ones transmitted by a transmitter with a horn antenna.

Fig. 3.9 shows the CDF of the rise time t_{rise}. The empirical model in [11] is the log-normal distribution with the log mean of -2.94 and the log standard deviation of 0.63. One can see that although there is a difference in the shape of the CDF, these results are consistent with the empirical model in that the rise time ranges from 0.02 s to 0.15 s.

Fig. 3.10 shows the CDF of the mean signal attenuation A_{mean}. The empirical model in [11] is the Gaussian distribution with the mean of 13 dB and the standard deviation of 2.0 dB. This result shows that the signal in IEEE 802.11ad WLAN attenuates about 4.0 dB more than the signal in [11]. These difference might be attributable to the difference between the transmit antennas: the horn antenna employed in the report and the array antenna packed in the AP, and the position at which the pedestrian crossed the LoS path—the report [9] demonstrated that blockage at nearer positions to the receiver causes the higher signal attenuation in directional communications—.

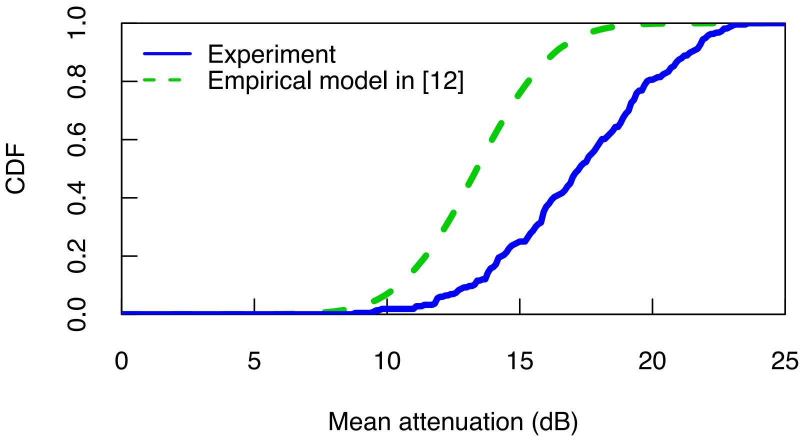

Figure 3.10: CDF of mean signal attenuation while pedestrian is blocking the LoS path, A_{mean}.

3.5 Conclusion

This chapter discussed a measurement method of time-varying attenuation of signals transmitted by a commercially available IEEE 802.11ad WLAN AP caused by human blockage. A two-state HMM is applied in order to estimate whether the AP transmitted signals or not in each sampling point. In addition, the BIC-based model selection is presented to decide which one-state model or two-state model to be applied. The two-state HMM-based estimation showed the valid results: both the sampling points estimated to be in frame transmission state and those estimated to be in pausing state are consecutive for a certain duration, which is consistent with a transmission mechanism of IEEE 802.11ad WLAN APs. The measurements are validated in a sense that the measured time-varying signal attenuation is in an agreement with knife edge diffraction theory. The measurements are also validated in that the statistical characteristics of the duration in which the signal transmitted by the AP attenuates by 5 dB was consistent with the existing statistical model. Meanwhile, the measurement results are different from the existing report in terms of the mean attenuation while a human is blocking a LoS path.

Chapter 4

Visual Data-Driven Handover Management for mmWave Networks Using Deep Reinforcement Learning

4.1 Overview

As discussed in the Chapter 1, mmWave communications are expected to play an important role in next-generation wireless networks, such as fifth-generation mobile networks or WLANs [29, 39–41]. The exploitation of wider spectrum bands in the mmWave band facilitates multi-gigabit data transmission, thereby supporting communication services, such as ultra-high-definition televisions [39], VR [42], or augmented reality (AR) [43] that require the multi-gigabit data transmission.

However, designing robust millimeter networks is quite challenging owing to the high frequency of the mmWave bands. The distinct feature of mmWave communication is the use of directional antennas to compensate for high path loss in mmWave bands. The directional antennas can be implemented by embedding many small antenna elements designed for mmWave in a limited physical space in mobile terminals as well as mmWave BSs. However, as discussed in Chapter 1, the antenna directivity makes mmWave communication links vulnerable to link blockage caused by moving obstacles. The link blockage suddenly penalizes the mmWave link budget by 20–30 dB in the case of data transmission comprising the use of directional antennas [28, 33]. The sudden and damaging degradation in the received power causes frequent interruptions within a transmission of streamed data, which is a crucial problem for VR/AR applications.

To overcome the blockage problem and provide reliable mmWave communications, a handover between multiple BSs is envisioned as a promising scheme [44–48]. By performing handovers at appropriate times, the decreased link budget can be compensated with another BSs. In next-generation cellular networks, an increasing number of mmWave BSs will be deployed to ensure a LoS path between a mobile terminal and one of the deployed BSs; hence, designing a decision problem concerning when and to which BS a handover should be triggered, which is referred to as a *handover decision problem*, is an important research direction.

In a handover decision problem, it is important to predict a future long-term performance, e.g., the time-average or cumulative sum of the data rates prior to performing a handover in order to avoid making myopic decisions [49–54]. This is because a handover involves a service disruption caused by procedures that are necessary for changing association and for data forwarding to a BS to which handover is performed [55]. Performing handovers based on a short-term performance, i.e., making myopic decisions, results in frequent handovers that may cause the overall long-term performances to deviate [51, 52]. Thus, a future long-term performance in both the currently associated BS and the candidate BSs should be predicted prior to triggering a handover, and a handover decision rule should be formed such that the predicted performance is maximized.

In addition to the avoidance of redundant handovers, predicting future long-term performance is beneficial to avoid a lower data rate situation, particularly in mmWave communications, what is a main topic of this chapter. Due to moving obstacles, mmWave links experience faster data rate variation compared to microwave links. Given such constraints, the data rate provided by current BS may be lower than the rates provided by another BS before a handover execution is performed if the handover occurs after data rate variation. As a result, severe loss of the data rate takes place. By predicting future data rates within a longer time horizon, handover is performed to avoid data rate loss, so *proactive handover* is beneficial rather than detrimental.

However, it is still challenging to predict the future long-term performance in mmWave links proactively under the condition that moving obstacles cause the rapid variation of received powers or data rates. This is because the sudden variation exhibits little prior indications in the RF signal domain such as received power samples and channel state information[1]. Thus, to predict the rapid variations in data rates or received powers proactively, one should utilize other information domains that provide more informative features for predicting such variations.

To address this challenge, this chapter develops a proactive framework wherein future data rate degradations caused by moving obstacles are predicted from several hundreds of milliseconds before the degradation occurs and the handover timings are optimized based on the predicted values. The key idea is to leverage the time consecutive camera images[2] and to use deep Q-learning. Time consecutive camera images comprise information of the spatiotemporal dynamics of moving obstacles, which exhibits informative features for predicting the future obstacle-caused degradation of data rates in mmWave links. The optimization of the handover timings while predicting such future degradations based on camera images is a new challenge. The usage of camera images is incorporated into the RL-based handover

---

[1] With regard to the degradation of the received powers, there is a slight fluctuation in the received powers within 100 ms prior to the degradation, which is known as diffraction effects [9, 11, 33]. Hence, by analyzing the time-series of the received powers, one can predict the degradation from at most 100 ms before the occurrence [56]. Nonetheless, it is worthwhile utilizing the camera image domain for the two reasons. First, as experimentally confirmed in this chapter, based only on the variation, the degradation cannot be necessarily predicted in a proactive manner. Second, the degradation should be predicted earlier because the service interruption incurred by a handover could be several hundreds of milliseconds long [57].

[2] This chapter uses depth images pixels of which are used to measure the distance between the obstacles and the camera [58]. Depth images allow to obtain geometric relations between components within the scene. In the following discussion, it is considered that the depth images are available to a network controller.

frameworks (discussed in detail in the following section) by expanding the state space such that the state involves camera images. Moreover, by using a deep RL [25], the difficulty in handling the large dimensionality of the state space incurred by the state space expansion is overcome.

The contributions of this chapter are summarized as follows:

- This chapter highlights that the variation in the received powers before blockage events is not necessarily informative in predicting future data rate degradation in mmWave links. To confirm this, this chapter predicts the cumulative sum of future data rates with the RL method based on the state of the received power.
- Based on the following two ideas, this chapter proposes a proactive framework wherein handover timing is optimized while the degradation in data rate caused by obstacles is predicted within hundreds of milliseconds before degradation. The first idea is to expand the states such that the states comprise time-consecutive camera images, which provide informative features for predicting degradations, i.e., spatiotemporal dynamics of moving obstacles. The second idea is to leverage deep RL to overcome the computational complexity of learning the optimal handover policy incurred by the expanded state.

The rest of this chapter is organized as follows. Section 4.2 summarizes related works. Section 4.3 provides a generic system model of learning-based handover frameworks. Section 4.4 presents an experimental evaluation of the received-power-based prediction of the cumulative sum of the future data rates in a handover decision problem. Section 4.5 presents the image-based handover framework, which leverages time-consecutive camera images in a handover decision problem. Section 4.6 extends the proposed image-based handover framework to a multiple cameras case. Finally, Section 4.7 presents concluding remarks.

It should be noted that Sections 4.4 and 4.5 are related to each other. The former provides a baseline for the framework without camera images to be compared with the proposed image-based handover framework, and the latter details the image-based handover framework. In concrete, in Section 4.4, the problem of a received power-based handover framework sum-

Table 4.1: Comparison of handover-related previous works.

	[49, 54, 59]	[51–53]	[50, 60, 61]	[62]	[63–65]	[66, 67]	**This chap.**
Timing Opt.	Yes	Yes	Yes	Yes	No	No	**Yes**
Frequency	mrc.	mrc.	mmW	mmW.	mmW	mmW	**mmW**
Usage of images	No	No	No	No	Yes	Yes	**Yes**
Proactive prediction	No	No	Yes	Yes	Yes	Yes	**Yes**
Approach	DP	RL	DP	RL	Heuristic	SL	**RL**

marized in the first contribution is highlighted. This received power-based handover framework is referred to as a baseline without camera images, and compared to the proposed image-based handover framework in Section 4.5. Focusing on the highlighted problem, Section 4.5 proposes the image-based handover framework presented in the second contribution. Subsequently, the section discusses the difference between the handover policies learned with and without camera images by comparing the proposed image based-handover framework with the received power-based handover framework.

4.2 Related Works

4.2.1 Handover Decision Problems

In many studies, handover decision-making problems or cell selection problems in heterogeneous microwave networks or millimeter wave networks were formulated with the objective of maximizing the future long-term performance [49–54, 59]. The authors of [49, 54, 59] designed the optimal cell selection problem in heterogeneous wireless networks with the objective of maximizing the weighted sum of the network bandwidth and network delay via the MDP models or optimal control models. The optimal strategies are provided via dynamic programming (DP) techniques. In [50], optimal cell selection in mmWave networks was proposed to maximize the long-term throughput or total received data in a mobile terminal using a similar approach. The authors of [51–53, 68] applied an RL algorithm to learn the optimal cell selection with the objective of maximizing the long-term quality of experiences or channel capacities, wherein an optimal strategy of cell selection can be learned without prior knowledge of the transition probability of the channel states or received powers. However, in the aforementioned studies, a decision process was considered wherein a decision maker makes a decision based on a current network state such as the channel information, received power, or network bandwidth. These studies did not detail the challenge of predicting the future long-term performance in mmWave links under the condition of moving obstacles causing blockage effects and received powers at a user equipment (UE) or the BSs[3] and the data rates in the mmWave links undergoing rapid degradation.

Other works have addressed handover decision-making problems in mmWave networks by using user mobility information or pedestrian mobility information [60–62]. User mobility information facilitates the prediction of future data rates in mmWave links with blockage effects that occur when users are entering areas blocked by static obstacles [60, 61]. However, the proactive prediction of the data rate degradations caused by moving obstacles is not addressed. The author's previous work [62] addressed handover decision problems based on the positions and velocities of a moving pedestrian. However, the proposal is not applicable to handover decision problems wherein more pedestrians cause blockage effects because of the challenge of capturing the spatial features of each pedestrian such as their height or shape. In contrast, in this chapter, camera images that comprise spatial information are used, which enables one to capture the spatial features of moving obstacles.

4.2.2 Camera Image-Based Frameworks in mmWave Networks

The authors of [63–65] have conceptualized a camera-assisted proactive handover system for mmWave networks. The camera images are employed to predict the occurrence of blockage effects caused by pedestrians approaching a LoS path between a BS and a UE. The experiments conducted in these

---

[3] Hereinafter, being consistent with a terminology of cellular networks, terminal nodes are termed UEs, and infrastructure nodes serving UEs are termed as BSs. This is due to prevent the use case discussion of the proposed handover framework from being limited into WLANs in an indoor room and to open the discussion for other environments as discussed in Chapter 1.

works demonstrated that using camera images, a handover can be triggered several seconds before blockage the occurrence of the blockage effects. However, the methods embedded in the experiments are focused on predicting the timings at which blockage effects occur, and they do not quantitatively predict the future data rate degradation caused by pedestrians. As discussed in the previous section, the optimal handover requires a prediction of the future long-term performances; hence, the aforementioned methods cannot provide the optimal solution to handover decision problems.

Motivated by the issue, a novel method for quantitatively predicting a future received power value in mmWave communications was proposed in [67]. The method predicts a received power value from several hundreds of milliseconds before the value is observed. In this method, camera images are mapped, via a supervised learning technique, to a future received power value that is obtained several hundreds of milliseconds after the camera images are obtained. However, the prediction method in [67] is not specific to handover decision problems. While the method in [67] can be used to predict a future data rate at a certain time period, the optimization of the handover timings requires a different prediction, i.e., the prediction of the expected cumulative sum of future long-term data rates as confirmed in the previous studies discussed in Section 4.2.1. Thus, the method in [67] cannot be necessarily adopted directly in handover decision problems. Table 4.1 summarizes the main aspects of the previous works related to this chapter.

4.3 System Model

Fig. 4.1 shows the system model of learning-based handover frameworks. The main building blocks are a channel environment, a processing unit, and a network controller. The processing unit accepts possible observations from the channel environment and makes handover decisions. These handover decisions are sent to a network controller, and subsequently, the network controller sends a control instruction to a serving BS and notifies the index of the target BS.

The following handover procedure can be optional. For an example of the X2 handover procedure in long-term evolution networks [69], the serv-

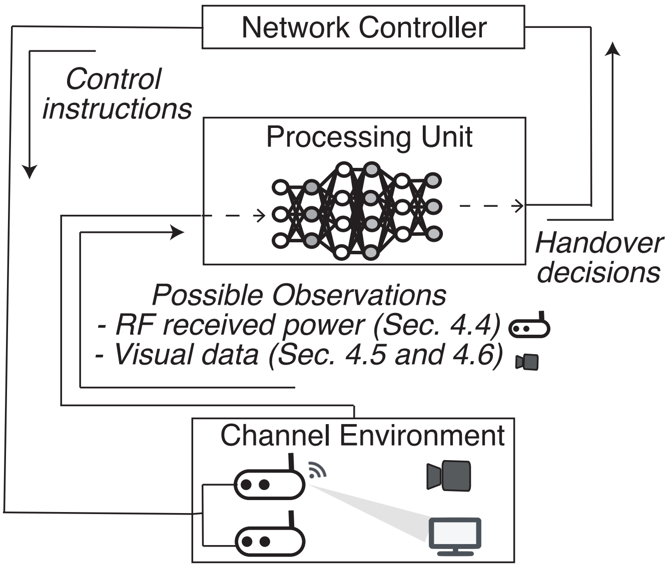

Figure 4.1: System model of learning-based handover frameworks. The processing unit accepts possible observations and determines the BS that the UE should be associated with. This chapter mainly proposes the usage of visual data as possible observation in Sections 4.5 and 4.6, which is compared to the usage of RF received powers in Section 4.4.

ing BS sends a handover request message to the target BS, and the target BS responds to the request by sending a handover request acknowledgment message. Subsequently, the serving BS sends a radio resource control connection reconfiguration message to the UE, and the target UE completes association procedures with the target BS.

The main objective of this chapter is to reveal the difference among possible observations in terms of handover policies. In Section 4.4, the usage of the time series of received powers is examined as a baseline. In Section 4.5, the usage of visual data is proposed, and it is shown that the visual data facilitates proactive predictions of blockage events, and thereby enabling to perform a proactive handover. In Section 4.6, this image-based handover is extended to the usage of multiple cameras, and the feasibility of cooperative sensing among multiple cameras is demonstrated.

4.4 Received Power-Based Handover Framework

The main objective of this section is to highlight that the fusture degradation of data rates in mmWave links caused by moving obstacles cannot necessarily be predicted based only on a variation in received powers. To illustrate this point, the cumulative sum of the future data rates is predicted using RL with the state information of the experimentally obtained received powers. This chapter will refer to the received power-based handover framework as a baseline without camera images, to be compared with the proposed image-based handover framework in Section 4.5.2. First, the decision process considered in this experiment is presented. Then, an experimental study of the prediction based on the received powers is provided.

4.4.1 States, Actions, Rewards, and State Transition Rules

This section presents the decision-making process considered in this experiment by detailing the states, actions, rewards, and state transition rules. In the decision-making process, a network controller makes handover decisions in the mmWave networks based on the received power values. In this section, it is considered that multiple mmWave BSs and a UE are deployed. There exist obstacles that block the LoS path between the UE and the BS associated with the UE. It is also considered that a handover should be triggered with respect to the time length of service disruption because the communication between the BS and UE is generally disrupted because of the necessary procedures for the association, which involves beam alignment and for data forwarding to a BS to which a handover is performed [57,70,71]. The duration for which the communication is disrupted is defined as the service disruption time T_{dis}.

It should be noted that in many existing studies [49, 50, 54, 60, 61], the handover decision process was formulated as an MDP, although it was assumed that the interval between the decision epochs was several seconds long, which is longer than a realistic service disruption time of several tens or hundreds of milliseconds [70]. Hence, the service disruption occurs within an interval between the successive decision epochs. However, the assumption of the large interval is not suitable for predicting the blockage effects that moving obstacles cause within several hundred milliseconds [11]. Hence, this section reformulates the problem wherein an interval between the successive decision epochs is shorter than several tens or hundreds of milliseconds, and several decision epochs could be within a service disruption.

States

For the network controller to detect blockage effects based on received powers, the states are desined such that they include the received power values. Let the number of time-consecutive received power values used in making handover decisions be denoted by N. The state space is given as follows:

$$\mathcal{S}_{\mathrm{rp}} \coloneqq \underbrace{\mathcal{P} \times \cdots \times \mathcal{P}}_{N} \times \mathcal{J} \times \mathcal{C}. \tag{4.1}$$

In (4.1), $\mathcal{P} \subseteq \mathbb{R}^J$ denotes the set of all possible received powers observed at all BSs, $\mathcal{J} \coloneqq \{1, \ldots, J\}$ denotes the set of the BS indices, and $\mathcal{C} \coloneqq \{\, c \mid c \in \mathbb{Z}, 0 \leq c \leq \lfloor T_{\mathrm{dis}}/\tau \rfloor \,\}$ denotes the set of the remaining decision epochs until the service disruption time ends, where J denotes the number of the deployed BSs, $\lfloor \cdot \rfloor : \mathbb{R} \to \mathbb{R}$ denotes the floor function, and τ denotes the interval between the successive decision epochs.

Let $s_t = (p_t, p_{t-1}, \ldots, p_{t-N+1}, j_t, c_t) \in \mathcal{S}_{\mathrm{rp}}$ denote the state at the decision epoch t. The element $p_{t-k} \in \mathcal{P}$ for $k \in \{0, 1, \ldots, N-1\}$ is set as the received power observed at the decision epoch $t-k$. The element $j_t \in \mathcal{J}$ is set as the index of the BS associated with the UE. The element $c_t \in \mathcal{C}$ is set as the number of remaining decision epochs that the network controller experiences until the service interruption ends. When the decision epoch is not within the service disruption time, c_t is set as zero.

Actions

The action set $\mathcal{A}(s_t)$ consists of the possible actions and is given as follows:

$$\mathcal{A}(s_t) := \begin{cases} \mathcal{J}, & c_t = 0; \\ \{j_t\}, & c_t \neq 0. \end{cases} \tag{4.2}$$

In other words, the controller selects one of the BSs when the decision epoch is not within the service disruption time; otherwise, the controller selects only the index of the BS to which a handover is performed.

Reward

The reward is given by a performance metric in the link provided by the BS that is currently associated with the UE. Meanwhile, when the next decision epoch $t + 1$ is within the service disruption duration, the reward is given as zero. These are formulated as follows:

$$r(s_{t+1}, a_t, s_t) := \begin{cases} R_{j_{t+1},t+1}, & c_{t+1} = 0; \\ 0, & c_{t+1} \neq 0. \end{cases} \tag{4.3}$$

In (4.3), $R_{j_{t+1},t+1}$ denotes the performance metric in the link provided by BS j_{t+1} at $t + 1$. In the performance evaluation, the metric $R_{j_{t+1}}$ is set as the achievable data rate provided by BS j_{t+1} as discussed in Section 4.4.2.

State Transition

The state transition to the next state is as follows. Let the state at epoch $t+1$ be $s_{t+1} = (p_{t+1}, p_t, \ldots, p_{t-N+2}, j_{t+1}, c_{t+1}) \in \mathcal{S}_{\mathrm{rp}}$. Evidently, the received power values $(p_{t+1}, p_t, \ldots, p_{t-N+2})$ at $t+1$ are updated by concatenating the received power values at p_{t+1} with the current values $(p_t, p_{t-1}, \ldots, p_{t-N+1})$ and removing the oldest value p_{t-N+1}. Based on the definition of the state, the term j_{t+1} is determined as follows:

$$j_{t+1} = a_t. \tag{4.4}$$

The term c_{t+1} is determined as follows:

$$c_{t+1} = \begin{cases} c_t - 1; & c_t \neq 0, \\ \lfloor T_{\mathrm{dis}}/\tau \rfloor; & c_t = 0, a_t \neq j_t, \\ 0; & c_t = 0, a_t = j_t. \end{cases} \tag{4.5}$$

It should be noted that without knowing the transition probabilities, one can learn the optimal action-value function using deep RL [25]. To learn the optimal policy, one only requires transition samples (s_t, a_t, r_t, s_{t+1}) that can be obtained while making decisions in the learning procedure.

In the following, an example of the temporal transition of the decision process is provided. Consider that at the decision epoch t, $s_t = (p_t, p_{t-1}, \dots, p_{t-N+1}, 1, 0)$, i.e., the received power values $(p_t, p_{t-1}, \dots, p_{t-N+1})$ are available, the UE is associated with BS 1, and the decision epoch is not within the service disruption time. If the controller selects action $a_t \neq 1$, i.e., a handover is performed, then the state transitions to $s_{t+1} = (p_{t+1}, p_t, \dots, p_{t-N+2}, a_t, \lfloor T_{\mathrm{dis}}/\tau \rfloor)$. The controller is subsequently given a reward of zero because $c_t = \lfloor T_{\mathrm{dis}}/\tau \rfloor \neq 0$ (see (4.3)). In this case, until the service disruption time ends, the controller selects action a_t, is given a reward of zero, and decreases the last element of the state by one. Conversely, if the controller selects action $a_t = 1$, i.e., the handover is not performed, then the state transitions to the state $s_{t+1} = (p_{t+1}, p_t, \dots, p_{t-N+2}, 1, 0)$ and the controller is then given the reward $R_{1,t+1}$.

4.4.2 Experimental Evaluation

Evaluated Scenario

As shown in Fig. 4.2, two BSs and an UE are deployed in an indoor room whose length, width, and height are 4.87 m, 5.34 m, and 2.57 m, respectively. The size of the room corresponds to that of the room where the measurement in the next section was conducted. The two BSs are operated over the 60 GHz channel. The UE is initially associated with the BS that observes a higher received power as compared to that of the counterpart when there are

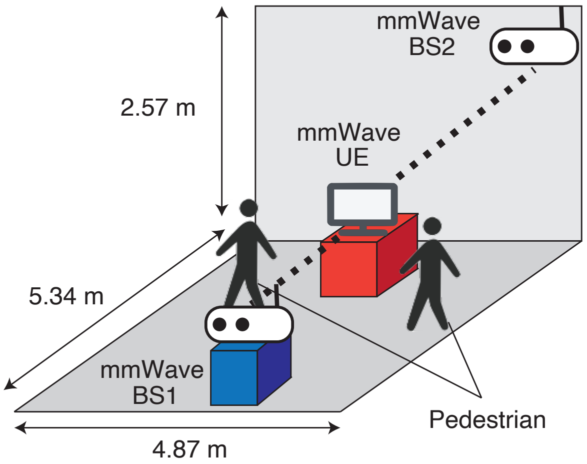

Figure 4.2: Experimented scenario of mmWave links.

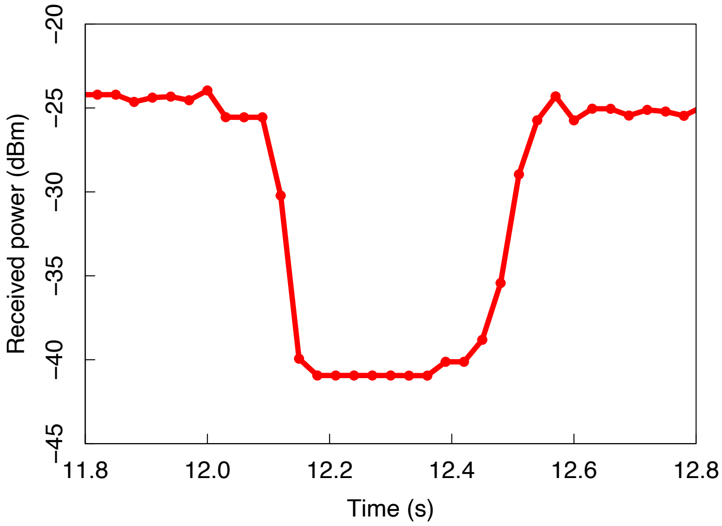

Figure 4.3: An example of the variation of the received power in a blockage effect.

no obstacles within the deployed area. The BS that is initially associated with the UE is termed as BS 1 and the other is termed as BS 2. BS 2 is a candidate BS for a case in which the link between BS 1 and the UE is blocked by obstacles. In the following discussion, the considered scenario is detailed including coverage area, UE mobility, channel characteristics, beamforming, initial access procedure, and beam tracking.

Coverage Area. A BS covers an entire room in Fig. 4.2 at least in a LoS condition, which is examined as follows. It is determined whether a BS can cover a certain position or not by examining whether a commercially available IEEE 802.11ad equipped transmitter and receiver can associate with each other. In this examination, it is validated that the transmitter can associate with the receiver placed 10 m apart from the transmitter in a LoS condition. Because the maximum distance between two positions is 7.67 m in the room, it is safe to say that a BS covers the room in Fig. 4.2 at least in a LoS condition, which is sufficient for performing the evaluation.

UE Mobility. In this evaluation, the received power varies only because of moving obstacles, not because of the UE movements to focus on the sudden variation of the data rate caused by moving obstacles. To obtain such received power samples, the experiment is arranged such that the position of the UE is static, and a handover is performed to compensate the degraded data rate caused by the obstacles rather than to support the UE mobility. The evaluation in such a scenario is sufficient for the two objectives of this chapter: highlights that the such sudden variations of the data rate cannot be predicted from a received power time series (provided in Section III) and demonstrates the feasibility of the proactive prediction on such variations achieved by camera images (provided in Section IV). This scenario of the static UE is reasonable for certain realistic application such as the transmission of streaming data to a wireless monitor in an offices.

Channel Characteristics Between BS 1 and UE. The channel between BS 1 and UE is based on the measurement in the next section, where the overall characteristics are similar to “dynamic 60 GHz radio channel” [11] in terms of the variation of the received powers only due to the moving obstacles. An example of the variation of the received power in a blockage effect is shown in Fig. 4.3, and the overall characteristics are as follows. In a blockage effect, the received power decreases by approximately 15 dB within 50–200 ms Subsequently, the received power remains constant for 200–300 ms, and then it recovers to the original value within 50–200 ms.

Blockage Distributions. Because the channel between BS 1 and UE is based on the measurement provided in the next section, the distributions

Table 4.2: Estimated distribution parameters characterizing blockage events observed in measurement.

Values	Distribution	Estimated Distribution Parameters
$t_{\mathrm{decay},5\,\mathrm{dB}}$	Gaussian [6]	mean: 0.059, standard deviation: 0.034
$t_{\mathrm{rise},5\,\mathrm{dB}}$	Log Normal [6]	log mean: -3.01, log standard deviation: 0.195
A_{mean}	Gaussian [6]	mean: 14.2, standard deviation: 2.08
t_{D}	Weibull [6]	scale: 0.553, shape: 4.08
t_{LOS}	Weibull [72]	scale: 2.31, shape: 1.51

characterizing the blockage events also depend on the measurement. To quantitatively characterize the blockage events in the measurement, Table 4.2 provides the estimated distribution parameters of the following five variables, which are essential in characterizing blockage events [11, 72]. In Table 4.2, $t_{\mathrm{decay},5\,\mathrm{dB}}$ denotes the duration in which signal attenuation level increases from 0 dB to 5 dB, $t_{\mathrm{rise},5\,\mathrm{dB}}$ denotes the duration in which signal attenuation level decreases from 5 dB to 0 dB, A_{mean} is the mean signal attenuation, and t_{D} denotes the duration of the blockage event. The value t_{LOS} is the duration wherein a LoS condition sustained. The definitions of the values follow the works of [11] and [72]. The choice of the distribution functions is based on [11] or [72], and the parameters of the distributions are determined by the maximum-likelihood estimation. The blockage events occurred within the 21% time-length relative to the whole measurement time.

Channel Characteristics Between BS 2 and UE. Meanwhile, the mmWave channel between BS 2 and UE is static, and it is assumed that BS 2 is free of blockages. The assumption is reasonable given that a network controller is likely to perform a handover to a BS that is not blocked by obstacles. In the following discussion, it is considered that BS 2 is at a position where pedestrians cannot block the path between the UE and

BS 2, and the received power at BS 2 is constant over time. Since the focus of the evaluation is on a blockage effects between UE and BS 1, only the link between the UE and BS 1 is discussed in the following discussion.

Beamforming. The UE and BS 1 communicate with each other with directional antennas. Because channel characteristics between BS 1 and UE are based on the measurement, the antenna gain is also attributed to the measurement equipment. The antenna gains of a transmitter and measurement device, which corresponds to the UE and BS 1, respectively, are provided in the measurement setup.

Initial Access Procedure. Prior to the evaluation, the beam of UE is established based on an initial access procedure termed as iterative beam search method [71], which is used in the IEEE 802.11ad standard. This initial access procedure is because the measurement used the a commercially available IEEE 802.11ad equipped transmitter as the UE. Meanwhile, the beam of BS 1 is established manually such that the beams of BS 1 and the UE point towards each other. The procedure of establishing the beam directions of the UE and BS 1 is discussed in detail in the measurement setup.

Beam Tracking. In the next section, the measurement is conducted such that the UE and BS 1 do not perform a beam tracking. The aim is to eliminate the variation of the received powers due to beam tracking whose mechanisms depend on manufacturers and thereby to focus only on the sudden variations of the received powers due to moving obstacles. In the next section, it is detailed how the measurement is conducted such that the beam tracking is not performed.

Measurement Setup

As shown in Fig. 4.4, the measurement equipment is setup involving IEEE 802.11ad equipped transmitter/receiver, a measurement device, and a camera. The transmitter and a measurement device correspond to the UE and BS 1, respectively. The transmitter and measurement device is place at the height of 0.70 and 0.85 m, respectively. The camera is placed at either position $(0.60, 2.65)$ and $(1.80, 0.45)$ and at the heights of 1.50 m and

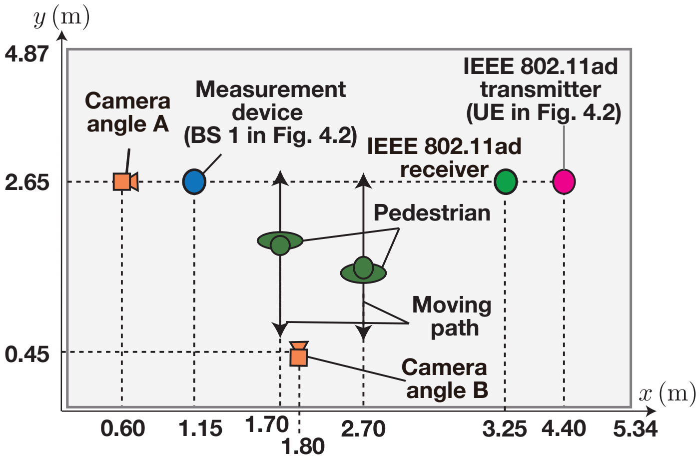

Figure 4.4: Top view of the measurement environment showing the mmWave transmitter, measurement device, and camera. The measurement device and mmWave transmitter correspond to BS 1 and the UE in Fig. 4.2, respectively.

1.25 m, respectively to obtain the a dataset with two different camera angles. The angle from the former position is termed angle A while the latter is termed angle B. The measurement device is equipped with a horn antenna with directivity gain of 24 dBi and the half-power beam width (HPBW) of 11 degree while the transmitter is equipped with an array antenna with size of 16, directivity gain of approximately 8 dBi, and HPBW of approximately 15 degree [30].

The beam directions of the measurement device and transmitter are established from the following procedure such that the beams point towards each other. First, the transmitter and receiver in Fig. 4.4 performed, in a LoS condition, an iterative beam search wherein the beam pair was searched with a two-stage beam scanning [71] such that the receiver can benefit from the maximum received power. Through the procedure, the beam of the transmitter is configured such that the beam points towards the receiver. Subsequently, the measurement device is placed behind the receiver such that the horn antenna attached with the measurement device faced for the transmitter. Since the beam of the transmitter also points towards the measurement device, the beams of the transmitter and measurement device point towards each other.

The measurements are conducted as discussed in Chapter 3, and the received powers and camera images are obtained. The mmWave transmitter transmits signals at the carrier frequency of 60.48 GHz to the receiver, and subsequently, the measurement device behind the receiver measures the power of a part of the signals. The transmitted signals are considered as uplink signals from the UE to BS 1. In this environment, two pedestrians walk along the moving path in Fig. 4.4 and obstruct the path between the transmitter and measurement device. Tables 4.3 summarizes the experimental equipment and parameters associated with the experiment.

Throughout the measurement, the beam tracking between the measurement device and transmitter is not performed. This eliminates the variation of the received powers due to beam tracking whose mechanisms depend on manufacturers, and one can thereby focus only on the sudden variations of the received powers due to moving obstacles. The details are as follows: The measurement device was located behind the receiver, and the pedestrians traveled between the receiver and measurement device indicated in Fig. 4.4. This arrangement prevented the receiver and transmitter from performing beam tracking because the received power at the receiver was not altered even when the LoS path between the receiver and measurement device was blocked. In this situation, the beam direction of the transmitter is almost fixed. Consequently, the beam directions in the transmitter and measurement device were also fixed, wherein the beam tracking between them was not performed.

It should be noted that the camera images obtained in this experiment are not used in this evaluation but are used in the next section. This evaluation provides the baseline that does not utilize camera images and only uses the time series of received powers to decide handover timings.

Procedure of Performing Decision Process

The obtained received powers are divided into two parts, and the individual parts are used for the learning and performance evaluation, respectively. Let the obtained received power values be denoted by $\left(p_{1,t}\right)_{t\in\mathcal{T}}$, where

Table 4.3: Experimental equipment and parameters.

IEEE 802.11ad transmitter	Dell® Wireless Dock D5000
IEEE 802.11ad receiver	Dell® Latitude E5540
Spectrum analyzer	Tektronix® RSA306
Down-converter	Sivers IMA® FC2221V
Antenna	Sivers IMA® Horn antenna, 24 dBi
Depth camera	Microsoft Kinect® [73] for Windows (Model:1656)
Channel	60.48 GHz
Sampling frequency	56 MHz
Transmit antenna gain	10 dBi [30]
Receive antenna gain	24 dBi
Measurement bandwidth W	40 MHz, 20 MHz

$p_{1,t}$ denotes the received power obtained at the tth observation, and $\mathcal{T} = \{1, 2, \ldots, T\}$ denotes the set of the time indices. The index set $\mathcal{T}$ is into the following two subsets: $\mathcal{T}_1 = \{1, 2, \ldots, T'\}$ and $\mathcal{T}_2 = \{T' + 1, T' + 2, \ldots, T\}$, where $1 < T' < T$. The first part $(p_{1,t})_{t \in \mathcal{T}_1}$ is used to learn the optimal action-value function, and $(p_{1,t})_{t \in \mathcal{T}_2}$ is used to evaluate the learned policy. In the following discussion, p_t is referred to as both received power values observed at BS 1 and at BS 2, i.e., $p_t \coloneqq (p_{1,t}, p_{2,t})$, where $p_{2,t}$ is the received power value observed at BS 2 and is constant $\forall t \in \mathcal{T}$.

The decision process in the learning procedure is simulated using $(p_t)_{t \in \mathcal{T}_1}$ as follows. The decision epoch is set as the time step at which a received power value is obtained. The decision process starts at the time step at which $p_{1,N}$ is observed. The UE is initially associated with BS 1 and the time at which the process starts is not within a service disruption time, i.e., $j_1 = 1$ and $c_1 = 0$. Thus, the state s_N is set as $(p_N, p_{N-1}, \ldots, p_1, 1, 0)$. The action a_N is selected according to a heuristic ϵ-greedy policy [25]; the next state s_{N+1} is then set such that it includes the images $(p_{N+1}, p_N, \ldots, p_2)$, j_{N+1}, and c_{N+1}, where j_{N+1} and c_{N+1} are determined based on a_N as shown in (4.4) and (4.5). The procedure is iterated, and it then ends when the state includes the received power values $p_{T'-1}$.

The performance metric $R_{j,t+1}$ for $j \in \mathcal{J}$ in (4.3) is set as the achievable data rate provided by BS j, which is associated with the UE and is calculated as follows. The metric $R_{j,t+1}$ is calculated by the Shannon capacity formula with the received power value $p_{j,t+1}$ as follows:

$$R_{j,t+1} = W \log_2\left(1 + \frac{p_{j,t+1}}{\sigma^2 W}\right),$$

where σ^2 denotes the noise power spectral density. It should be noted that the metric at $R_{2,t+1}$ is set as a constant value based on the assumption that the received power at BS 2 is a constant over time.

The performance of the learned policy is evaluated in the following step termed as performance test. In the performance test, a decision process is simulated using the same procedure as the learning procedure with the exception that $(p_t)_{t\in\mathcal{T}_2}$ is used, and the action is selected according to a greedy policy [23]. The time average of the reward is calculated as a performance metric of the learned policy. Then, the learning and evaluation are iterated using the same data set. The policy that achieves the highest average reward throughout the iterations is evaluated.

It should be noted that the handover policy is learned via deep RL [25] with a neural network (NN) that is different from that shown in Fig. 4.7 (discussed later). The NN architecture is simplified because the input of the NN in this scenario comprises several elements—the four elements in the evaluation. More specifically, the combination of the convolutional neural network (CNN) and long short-term memory (LSTM) in Fig. 4.7 are replaced with a fully connected multi-layer with eight hidden units and 32 output units, where the two layers are activated using rectified linear units [17]. The parameters associated with the deep RL are summarized in Table 4.4.

Results

In this experiment, it was shown that the obstacle-caused degradation in the data rates could not be predicted in a proactive manner by analyzing

Table 4.4: Parameters associated with RL.

Discount factor, γ	0.99
Number of obtained received powers T	16860
Number of received powers used for learning T'	13500
Number of iterations of learning and evaluation	1000
Exploration rate ϵ	1–0.01 (Decreased by 0.01 per iteration)
Number of received power values in state N	2
Interval between successive decision epochs τ	30 ms
Noise power spectral density σ^2	-173 dBm/Hz
Received power at BS 2, $p_{2,t}$	-129 dBm (const.)
Batch size [25]	32
Frequency of updating the target network [25]	10000

the learned action-value function in Fig. 4.5. Fig. 4.5 shows the time series of the achievable data rate provided by BS 1 and the corresponding learned action values. The data rate provided by BS 1 is degraded from approximately 13.25 s to 13.70 s because a pedestrian walks between the measurement device and transmitter. First, one can observe in Fig. 4.5 (a) that the data rate oscillates within approximately 90 ms before the degradation occurs, and thus, the time-variation in the received powers is successfully observed before the degradation, as confirmed in other propagation experiments [9, 11, 33]. However, the action value decreases sharply after the degradation in the data rate provided by BS 1. As the action value is defined as the expected sum of the future performance, one can conclude that the obstacle-caused degradation of data rates in a mmWave link cannot necessarily be predicted proactively based only on the variation in the received powers.

Owing to the characteristics of the action-value functions, handovers are performed after the variation in the data rate provided by BS 1. Fig. 4.6 shows an example of the time-varying data rate provided by the image-based handover framework when the service disruption time $T_{\mathrm{dis}} = 0.09$ s.

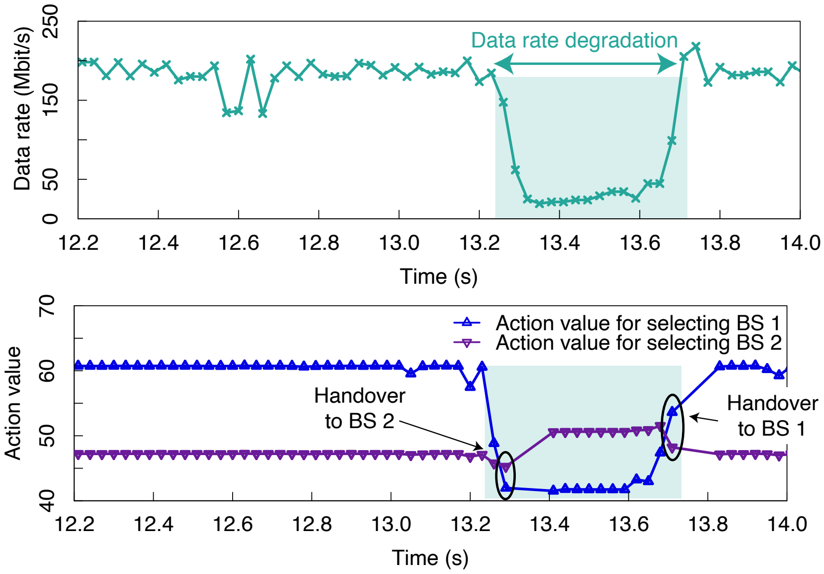

Figure 4.5: Comparison between time series of achievable data rate provided by BS 1 and that of learned action values. The action value, i.e., the estimation of the cumulative sum of the future data rates, decreases after the data rate decreases, which indicates that the degradation in the data rate provided by BS 1 cannot be predicted in a proactive manner.

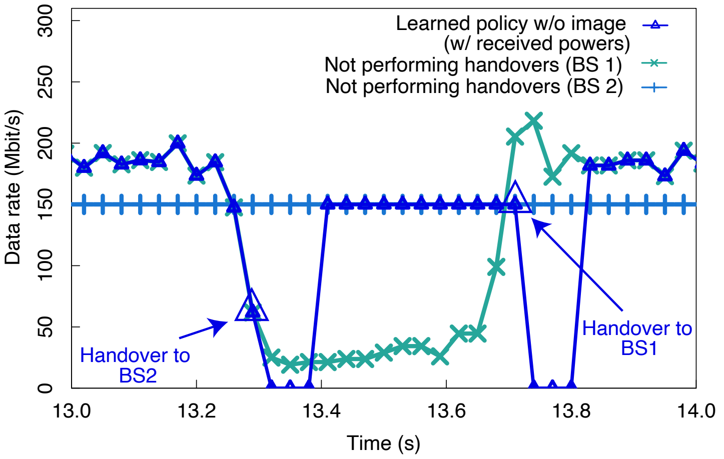

Figure 4.6: Example of handover timing when $T_{\mathrm{dis}} = 0.09\,\mathrm{s}$. Handovers are performed after the variation in the data rate provided by BS 1.

It can be observed that a handover is performed after the variation in the data rate, the degradation is experienced within approximately 60 ms. If the handover is performed earlier, the occurrence of the degradation in the data rate provided by BS 1 is prevented, and the time-average of the data rates is enhanced.

It should be noted that, if one observes the received powers to have a short time-resolution, e.g., one millisecond, he could predict the degradation in the data rate provided by BS 1 from based on the time-variation in the received powers that occurred before the degradation. However, as the time-variation occurred within approximately 90 ms, the degradation cannot be predicted from several hundreds of milliseconds before the degradation. This example motivates to develop a framework using other state information that exhibits more informative features for predicting even such degradation in the data rates in a proactive manner.

4.5 Image-Based Handover Framework—Single Camera Case

This section details a proactive framework wherein the handover timings are decided while the future degradation in the data rates is predicted in a proactive manner. First, to enable the proactive prediction, this section expands the state information such that the state includes time-consecutive camera images. Using the time-consecutive camera images, one can capture the spatiotemporal dynamics of obstacles that are informative for predicting the degradation. This section then demonstrates that with the expansion of the state space, the degradation can be predicted from several hundreds of milliseconds in advance and confirm that a performance gain is realized owing to the proactive prediction.

4.5.1 State Space Expansion for Proactive Prediction

For the network controller to leverage camera images for making handover decisions, this section expands the state space in the previous section such that the state includes consecutive camera images. Let the number of time-consecutive camera images used in making handover decisions be denoted by N. The state space is set as follows:

$$\mathcal{S}_{\mathrm{img}} \coloneqq \mathcal{S}_{\mathrm{rp}} \times \underbrace{\mathcal{X} \times \cdots \times \mathcal{X}}_{N}, \tag{4.6}$$

where $\mathcal{X}$ denotes the set of all possible images. It should be noted that the same actions, rewards, and state transition rules as (4.2)–(4.5), respectively, are considered to obtain a fair comparison of the performances achieved with the state space $\mathcal{S}_{\mathrm{rp}}$ and $\mathcal{S}_{\mathrm{img}}$, respectively.

The state design enables an RL to predict the future data rate degradations in mmWave links caused by moving obstacles and facilitates the maximization of the expected cumulative sum of the future data rates as in (2.6). This is because the state involving time-consecutive camera images reflects the spatiotemporal dynamics of the moving obstacles—for example, the dynamics of the obstacles approaching a LoS path—thus, reflecting the behavior of the data rates provided by deployed BSs at the future decision epochs $t+1, t+2, \dots$, which may comprise the decision epochs, in which one of the BSs is blocked. This section demonstrates that this novel state design allows to predict the degradation in the data rates caused by moving obstacles from several hundreds of milliseconds before the degradation occurs in the following section.

In the evaluation, the time-series of the received power values in the state information was not used because the information of the received power values may be redundant in the case of the existence of consecutive camera images. This is because the camera images $x_t, x_{t-1}, \dots, x_{t-N+1}$, reflect the spatial features at the decision epochs $t, t-1, \dots, t-N+1$, which may also be informative for capturing the received power values $p_t, p_{t-1}, \dots, p_{t-N+1}$ because the received power values are heavily dependent on the spatial features, such as the distance between a transmitter and receiver and the positions and shapes of obstacles that obstruct the path between the receiver and transmitter [9]. Thus, in this evaluation, the state space is set as follows:

$$\hat{\mathcal{S}}_{\mathrm{img}} \coloneqq \underbrace{\mathcal{X} \times \cdots \times \mathcal{X}}_{N} \times \mathcal{J} \times \mathcal{C}.$$

That is, the sets of received power values $\mathcal{P}$ are omitted from the state space $\mathcal{S}_{\mathrm{img}}$.

4.5.2 Experimental Evaluation

The image-based handover framework discussed above is evaluated. The objective of this evaluation is to verify the feasibility of the proactive prediction on data rate variation caused by moving obstacles if a camera is available for performing the prediction. Hence, further issues incurred by introducing cameras, such as costs for camera installments, were left aside, and this section perform the evaluation focusing on the objective. The next section details the evaluated scenario and discusses realistic scenarios where the results from this feasibility study can be applied possibly without any additional costs for camera installments.

Evaluated Scenario

Consider the scenario as discussed in Section 4.4.2 with regard to the deployment of the BSs and UE, channel, initial access procedure, and the coverage area of the BSs. In the scenario, a camera monitors the two pedestrians that walk between BS 1 and the UE. As it was assumed that BS 2 is free of blockages, the prediction in the performance of the link between BS 2 and the UE is not performed.

This experiment is performed by fixing measurement device and transmitter positions and changing camera angles motivated by the objective of this evaluation. The objective of this experiment is to validate the feasibility of the proactive prediction achieved by introducing cameras in the two basic angles. Hence, it is beyond the scope of this chapter to perform experiments in various configurations such as in terms of the parameters irrelevant to cameras.

There are some realistic scenarios to which the results from this feasibility study in this chapter can be applied. In this feasibility study, it is examined that one can at least perform the proactive prediction with camera images if an UE and BSs are static, and the order of the distances from the UE and BSs are several meters. Hence, it is expected that the results are also applied to, for example, a video streaming to static wireless monitors in an office, where the UE and BSs are also static and the order of the distances from an UE to BSs are several meters.

Moreover, in such realistic scenarios, additional costs are not necessarily incurred when one can utilize pre-installed cameras. In concrete, given the aforementioned scenarios transmitting streaming data, one can utilize pre-installed surveillance cameras monitoring the entire office. In this case, the results from this feasibility study can be applied possibly without any additional costs for camera installments.

Concerning a real implementation, the image-based handover framework is evaluated in the two totally different camera angles shown in Fig. 4.4. The camera angles affect how the obtained images represent the movement of pedestrians, and thus, they may also affect the feasibility of the proactive prediction more strongly compared to other parameters irrelevant of cameras such as the distance of the UE and BS or their heights. Hence, concerning the camera angles may be important for a real implementation, the evaluation in the two basic camera angles that are orthogonal to each other is performed.

Procedure of Performing Decision Process

The decision process in the image-based handover framework is performed using a procedure similar to that used in the previous evaluation with the exception that the state includes consecutive camera images obtained in the experiment. Let x_t denote the camera image (that contains 40×40 pixel values in the experiment and obtained with the frame rate of 30 frames per second) obtained at the same time when the received power value $p_{1,t}$ is obtained[4]. From the state definition in (4.7), the received power values $p_t, p_{t-1}, \dots, p_{t-N+1}$ in the state s_t in the previous evaluation is replaced with the time consecutive images $x_t, x_{t-1}, \dots, x_{t-N+1}$. The optimal policy

---

[4] Technically, the frequencies of image and received power acquisitions are different, i.e., the former is 30 frames per second whereas the latter is 50 samples per second. Hence, I associated each camera image with the nearest neighbor received power value in terms of acquisition time. Indeed, this association procedure yields at most 10 ms time difference between the image and received power. However, this difference is negligible because the variation within 10 ms is approximately less than five decibels from the results in Chapter 3, which is much smaller than the maximum attenuation due to blockage events.

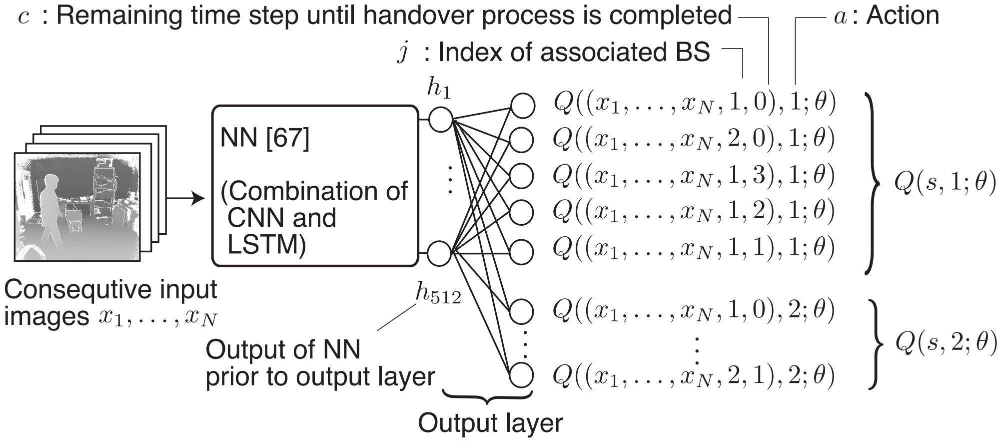

Figure 4.7: NN architecture for approximating optimal action-value function $Q^{\star}(s,a)$ defined in (2.7) for $\mathcal{C} = \{0,1,2,3\}$ and $\mathcal{J} = \{1,2\}$. With the exception of the output layer, the architecture herein is identical to that used in [67]. The architecture is a combination of a CNN, which deals with images, and an LSTM, which deals with sequential inputs [17].

is learned using deep RL with an NN that is specifically used for handling the time consecutive camera images as discussed in the following section. The parameter associated with the deep RL is set as shown in Table 4.4.

Neural Network Architecture

In the deep RL, an NN is trained such that the NN is a good approximation of the optimal action-value function $Q^{\star}(s,a)$ in (2.7) [25]. The focus of this section is on the NN architecture designed to perform deep RL in the decision process discussed in the previous subsection[5].

The NN architecture is designed such that the NN has separate outputs for each possible combination of $j \in \mathcal{J}$, $c \in \mathcal{C}$, and $a \in \mathcal{A}$, as shown in Fig. 4.7. The design allows to divide the parameters into two parts: the parameters associated with the camera images and those associated with the other low-dimensional observations j, c, and a. Let $Q(s,a;\theta)$ be the

---

[5] The NN is trained using the method discussed in [25]. For details of the training, [25] may be referred to.

NN, where $s \in \hat{\mathcal{S}}_{\text{img}}$, $(x_1, \dots, x_N) \in \mathcal{X}^N$, and θ denote the parameters of the NN. In the architecture, the NN is expressed as follows:

$$Q\big((x_1, \dots, x_N, j, c), a; \theta\big) = \sum_{k=1}^{512} \theta_{j,c,a,k} h_k, \tag{4.7}$$

where $h_1, \dots, h_{512}$ denote the output values of the layer prior to the output layer and $\theta_{j,c,a,1}, \dots, \theta_{j,c,a,512}$ denote the parameters in the output layer corresponding to the combination of j, c, and a. The parameters used to obtain the output values $h_1, \dots, h_{512}$ are associated with the camera images, and the parameters in the output layer, $\theta_{j,c,a,1}, \dots, \theta_{j,c,a,512}$ are associated with the low-dimensional observations j, c, and a.

The motivation for the architecture is that it is necessary to use the observations j and c for handover control. In the considered problem setting, the state s consists of N consecutive images $(x_1, \dots, x_N)$ with thousands of elements and (j, c) with only two elements. If the input of the NN is $(x_1, \dots, x_N, j, c)$, and thereby, the camera images $(x_1, \dots, x_N)$ and (j, c) are processed using the same parameters, the variation in (j, c) does not significantly impact the NN output values. This is because NNs generally estimate the feature representations of overall inputs; thus, they do not propagate the variation in one or two elements in the inputs to the output [17]. Hence, the controller can ignore the variation in (j, c) while making a handover decision.

It should be noted that the NN architecture used in [67] is employed with the exception of the output layer. The architecture is reported to facilitate the prediction of a future data rate in a mmWave link based on camera images. Hence, it is expected that the architecture also facilitates the learning of the optimal action-value function, which is the cumulative sum of the performance data rates in the considered problem setting.

Results

It is confirmed that the deep RL successfully maximizes the time-average of the achievable data rate in the mmWave links in the state design in (4.7). Fig. 4.8 shows an example of a time series of the data rate in the case wherein $T_{\text{dis}} = 0\,\text{s}$. The pedestrians walk in front of the mmWave transmitter at

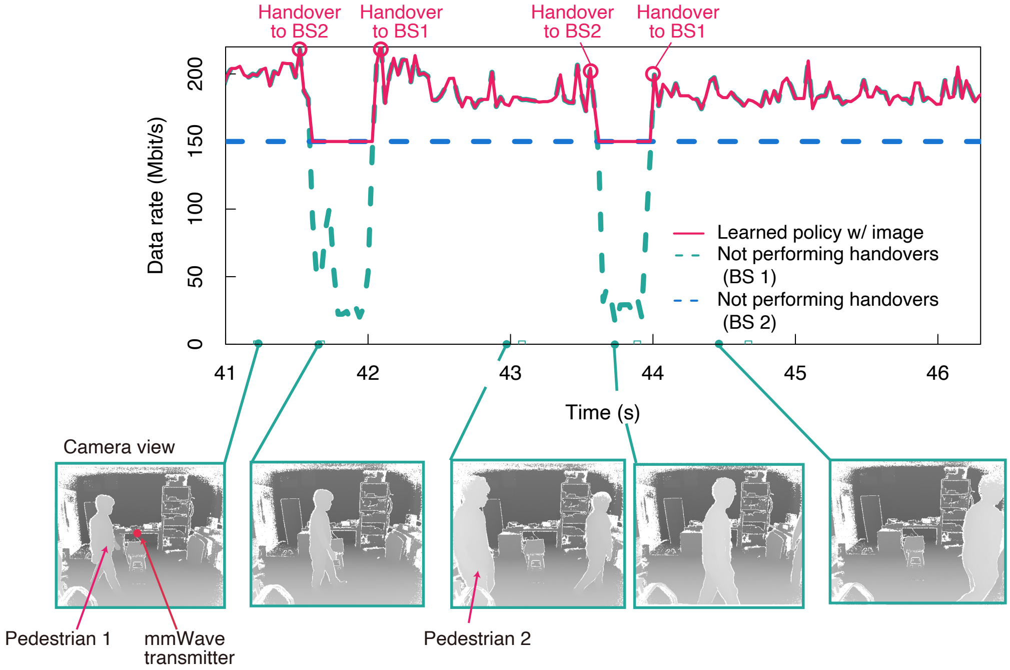

Figure 4.8: Time series of the achievable data rates under the condition of the service disruption time of $T_{\mathrm{dis}} = 0\,\mathrm{s}$ and the corresponding camera images.

approximately 41.5 s and 43.9 s. At the same time, the data rate provided by BS 1 is degraded from approximately 200 Mbit/s to 30 Mbit/s. The image-based handover framework successfully selects the BS that provides a higher data rate than the counterpart at each decision epoch and thereby maximizes the overall data rate.

It should be noted that in Fig. 4.8, the intervals between the two successive handovers, i.e., the handover from BS 1 to BS 2 and that from BS 2 to BS 1 are according to the durations wherein the blockage effects sustained. This results can be interpreted that the image-based handover framework can form a handover strategy while predicting such durations wherein the blockage effects sustain in an end-to-end manner. In this regard, we've achieved the prediction of such durations implicitly in learning the handover policy.

The proposed framework predicted a future data rate degradation from

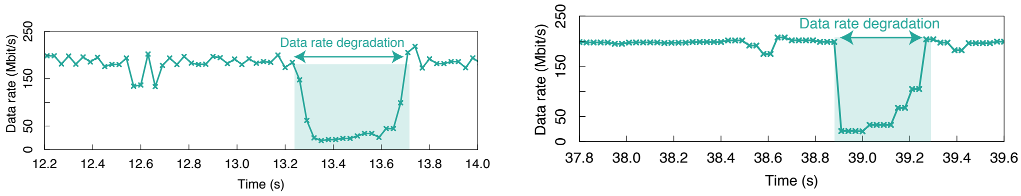

(a) Data rate provided by BS 1 obtained when the camera monitors with angle A.

(b) Data rate provided by BS 2 obtained when the camera monitors with angle B.

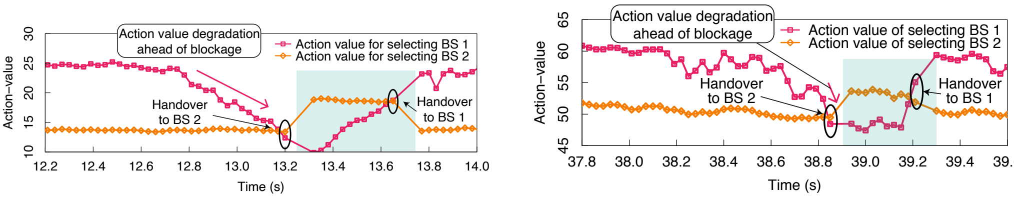

(c) Action value in proposed framework when the camera monitors with angle A.

(d) Action value in proposed framework when the camera monitors with angle B.

Figure 4.9: Comparison between time series of the data rate provided by BS 1 and that of the learned action-value function.

several hundreds milliseconds before the degradation occurs. This is observable by analyzing the learned action-value function shown in Fig. 4.9. Fig. 4.9 shows the learned action value at each decision epoch before and after the blockage effect in Fig. 4.6. The action value begins to decrease from approximately 500 ms (in camera angle A) or 200 ms (in camera angle B) before the actual degradation in the data rate provided by BS 1. As the action value is defined as the expected sum of the future data rates, one can consider that the image-based framework successfully predicts the future performance degradation several hundred milliseconds before the blockage effects occur.

Owing to the proactive prediction, the image-based handover framework triggers a handover in a proactive manner. Fig. 4.10 (a) shows an example of a time-varying data rate provided by the image-based handover framework with camera angle A. The plotted duration corresponds to that in Fig. 4.6. The image-based handover framework is different from the

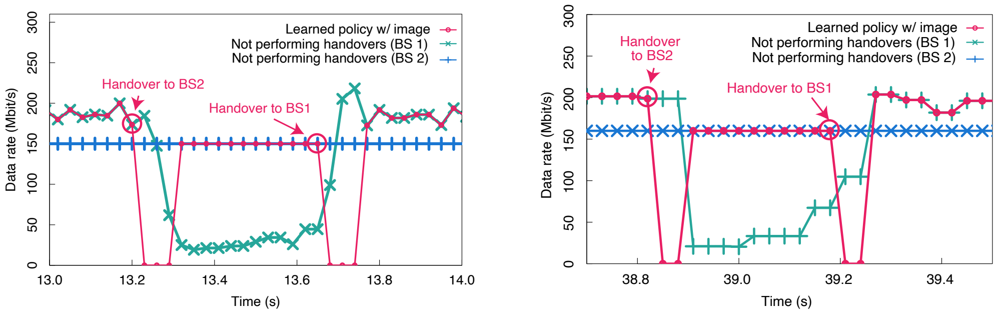

(a) Data rate and hanover timing learned when the camera monitors with angle A.

(b) Data rate and hanover timing learned when the camera monitors with angle B.

Figure 4.10: Example of handover timing. The proposed image-based framework performed handovers before the variation in the channel at BS 1 and UE with either camera angle A or angle B.

received-power-based prediction presented in the previous section in Fig. 4.6 and successfully triggers handovers prior to the variation in the data rate provided by BS 1. Fig. 4.10(b) shows an example of a time-varying data rate provided by the proposed image-based handover framework with the camera angle B. Similarly, with a different angle, the image-based framework triggers handovers prior to the degradation of the data rate provided by BS 1.

It should be noted that results show the feasibility of the proactive prediction even with the image time-series with 40×40 pixels and a frame rate of 30 frames per second. Hence, to accomplish the proactive prediction, it is sufficient to leverage such qualities of image videos, which cannot be obtained only with sophisticated cameras exampled by Kinect®sensors but also with commercial products of smart phones [74] or surveillance cameras [75].

The proposed image-based handover framework is compared with a handover framework that does not leverage images, i.e., the received power-based handover framework. Fig. 4.11 shows the average data rate achieved by the two handover policies over the duration of specific events 200 ms be-

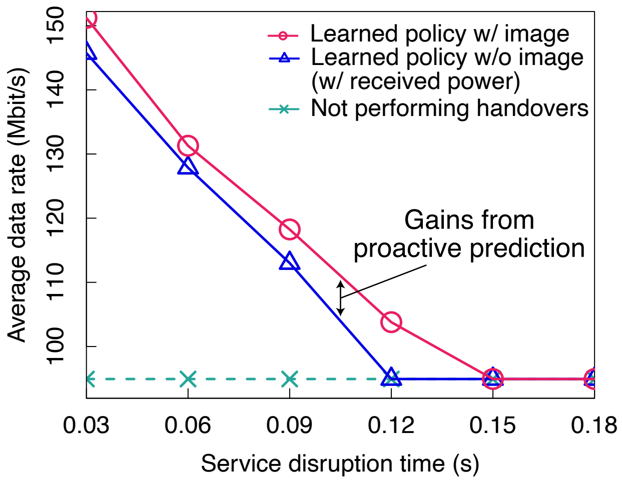

Figure 4.11: Performance comparison between proposed image-based framework and received power-based framework under various service disruption times T_{dis} when the camera in angle A.

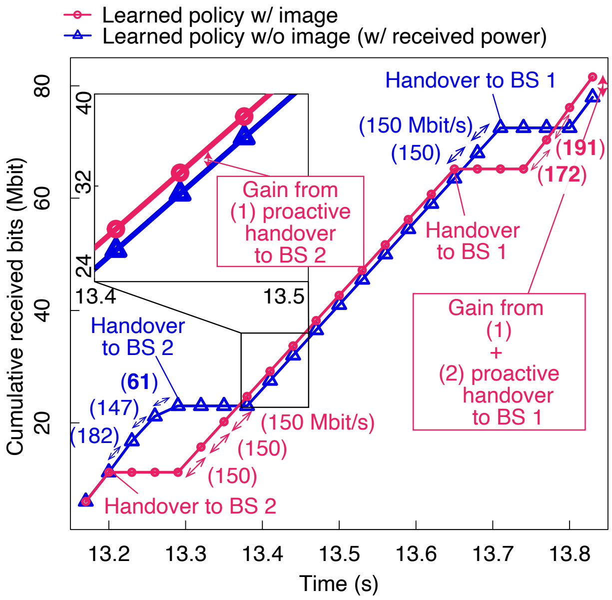

Figure 4.12: Comparison of cumulative received bits between the image-based framework and the received-power-based framework.

fore and after a blockage[6]. As blockage event, the one depicted in Figs. 5

---

[6] In detail, the blockage event is defined as the event where the received power is 3 dB below from the one observed in a LoS condition, which is according to [76].

and 9(a) has been chosen since handover policies with and without camera images exhibit different behavior according to the aforementioned figures. The choice of 200 ms is attributed to the fact that the two handover policies exhibited different a behavior from at most 200 ms before and after the blockage event. From Fig. 4.11, one can see that the handover policy learned with images achieves a higher or equal data rate as compared to the policy learned without images.

A realistic scenario where one can benefit from the gain is exemplified by combining Agile-Link [71] as the beam search method and make-before-break [77] as the handover procedure. In such a scenario, the service interruption subjected by a beam alignment is under 1 ms with a 128 size array, and by the other handover procedure would be tens of milliseconds. This leads to an overall service interruption time T_{dis} of several tens milliseconds. Recalling that there is a gain from the proactive handover when T_{dis} is in the order of tens milliseconds in Fig. 10, the system benefits from the gain in such a scenario.

To illustrate how the proactive handover led to the performance gain provided in Fig. 4.11, an analysis on the cumulative received bits in the proposed image-based handover framework and in the received power-based framework is useful. Fig. 4.12 shows the amount of cumulative received bits from the time 200 ms before the blockage event. The horizontal axis corresponds to that either in Figs. 5 and 9(a). After a handover to BS 2 is performed in the image-based handover framework, the amount of cumulative data bits is temporarily lower than that in the received power-based handover framework. Meanwhile, the amount of cumulative received bits in the image-based handover framework is larger than that in the power-based framework by 1.7 Mbit from instant 13.4 s. These results confirm the benefits of proactive handover in the long run, and the increase of the received bits can be interpreted as the gain from proactively performing a handover to BS 2. Similarly, the amount of cumulative bits in the image-based handover framework is larger than that in received power-based framework by 3.6 Mbit from instant 13.8 s. This can be attributed to the fact the image-based framework benefits earlier from a recovering data rate in BS 1 while the UE remains to be associated with BS 2 in the received power-based

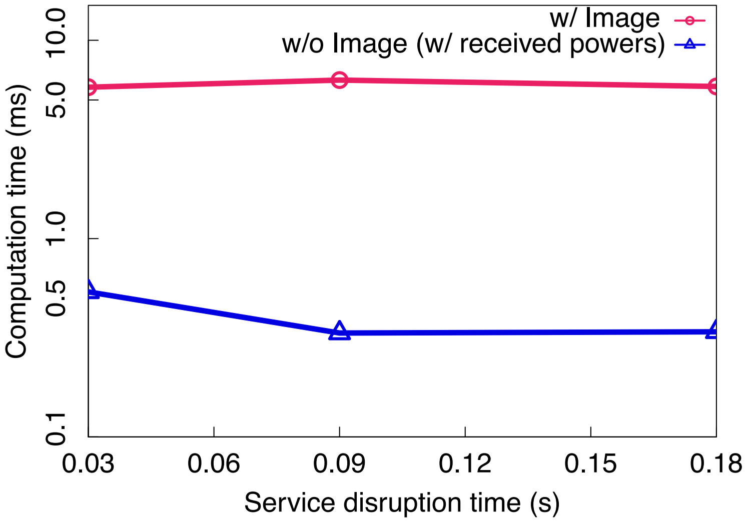

Figure 4.13: Computation time for making handover decisions.

framework. The increase in received bits can also be interpreted as a gain from proactively performing handover to BS 1.

Subsequently, the computation time required for making a handover decision is analyzed in the context of an example. Fig. 4.13 shows an example of the computation time for making a handover decision. The computation time is defined as the time for calculating the action-value from an input of images and is measured with a GeForce GTX 1080 Ti GPU. The received power-based handover achieved the smaller computation time because of the lower dimensionality of the input. Meanwhile, in the proposed image-based handover framework, the computation time was still in the order of several milliseconds. The computation time is sufficiently shorter than the required handover interval, i.e., an interval between the two successive handovers, and is reported as 750 ms in mmWave 5G systems [78]. Thus, a shorter computation time relative to the required handover interval is possible. To this regard, the computation time incurred by the large-dimensionality of images can be overcome.

The convergence property of the training procedure is investigated in Fig. 4.14. Fig. 4.14 shows the learning curve, i.e., the average data rate in the performance test corresponding to each training step. One can see

Figure 4.14: Average data rate in each performance test corresponding to a training iteration.

the following trends as the training steps are iterated: the performance enhancement, achievement of the maximum performance, and convergence to the degraded performance. These results shows that the training procedure does not converge to maximum performance. This is attributed to the fact that the training process is not stable, which is commonly reported in deep RL [23, 25] when a non-linear approximator for the action-value function is used. These results motivate to design an improved algorithm that converges to a maximum performance; however, seeking for the better convergence property is beyond the scope of this chapter.

Nevertheless, a practical solution can be employed to benefit from the results in this chapter. The solution named, "off-policy evaluation framework" [79], keeps track of the best performing policy. As this chapter evaluates the policy that achieves maximum average data rates among the learned policies, one can benefit from the results in this chapter by designing the algorithm such that the off-policy evaluation framework is performed.

4.6 Image-Based Handover Framework—Multiple Cameras Case

So far, this chapter experimentally demonstrated that via deep RL, an appropriate handover policy can be learned with the objective of enhancing overall performance based on images from one camera. However, blockage effects caused by a pedestrian out of the camera's coverage cannot be avoided. Thus, to deal with blockage effects caused by an arbitrary number of pedestrians, multiple cameras should be used.

This section investigates the feasibility of adopting cooperative sensing with multi-camera operation to the image-based handover framework. The multiple cameras allow blockage prediction while compensating for one another's blind spots. Deep RL is developed to learn the optimal mapping from multiple images to a handover decision.

This section is summarized as follows:

- To successfully adopt cooperative sensing with multi-camera operation to the image-based handover framework, this section designs a decision process where the state includes multiple images from multiple cameras.

- This section demonstrates the feasibility of adopting cooperative sensing to the image-based handover framework through an evaluation using experimentally obtained camera images and received powers. The evaluation validates that the framework with multi-camera operation outperforms a conventional framework with single-camera operation in terms of the average data rate.

4.6.1 Evaluated Scenario

Consider a scenario in which two BSs and an UE were deployed as shown in Fig. 4.15. The UE is initially associated with the BS that observed higher received power compared with that of the counterpart when there are no pedestrians. The BS initially associated with the UE is termed BS 1 and the

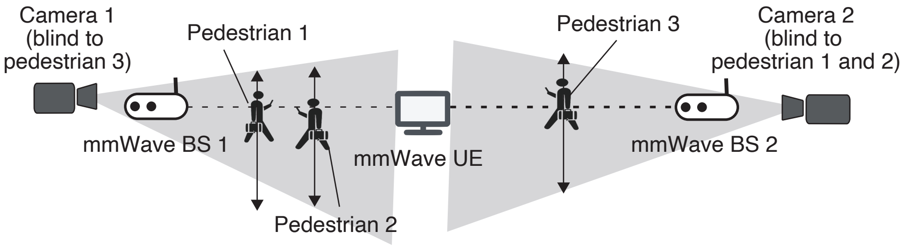

Figure 4.15: Considered mmWave links. ©2020 IEEE

other is termed BS 2. BS 2 is a candidate BS in the case the link between BS 1 and the UE is blocked by pedestrians.

Note that a multi-camera operation is considered, where the cameras compensate for one another's blind spots. Fig. 4.15 is the case where camera 1 is blind to pedestrian 2 because of limited coverage. Similarly, camera 2 is blind to pedestrian 1. By combining images from the cameras, the network controller can be aware of the movement of all pedestrians. Based on the combined images, the network controller predicts blockage effects and decides whether a handover should be triggered.

4.6.2 State Definition

For the network controller to utilize images from multiple cameras to make handover decisions, the states are designed such that they contain consecutive images from each camera. Let the numbers of deployed cameras and consecutive images be denoted by I and N, respectively. The state set is given as follows:

$$\mathcal{S} := \underbrace{\mathcal{X}^{(1)} \times \cdots \times \mathcal{X}^{(1)}}_{N} \times \cdots \times \underbrace{\mathcal{X}^{(I)} \times \cdots \times \mathcal{X}^{(I)}}_{N} \times \mathcal{J} \times \mathcal{C}. \tag{4.8}$$

In (4.8), $\mathcal{X}^{(i)}$ for $i = 1, 2, \ldots, I$ denotes the set of all possible images from the ith camera.

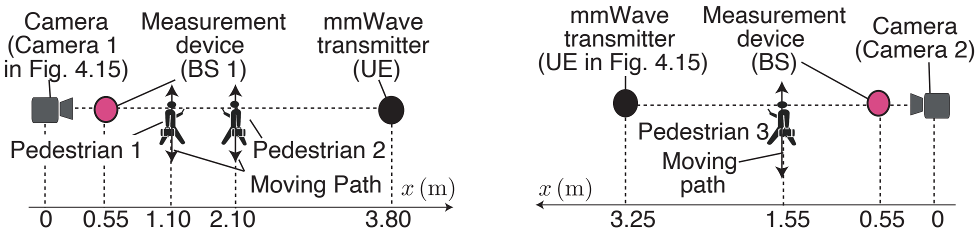

(a) Measurement on BS 1 side.

(b) Measurement on BS 2 side.

Figure 4.16: Top view of the measurement environment. The measurement device, camera, and mmWave transmitter are correspond to BS 1/BS 2, camera 1/camera 2, and the UE in Fig. 4.15, respectively. Due to experimental limitations, the same measurement equipment is used in the two measurements. ©2020 IEEE

4.6.3 Performance Evaluation

Measurement Setup

Two measurements are conducted, and two data sets each of which contains received powers and camera images are obtained. The former images are regarded as images from camera 1, while the latter are regarded as those from camera 2 in simulating the decision process as discussed in the following subsection. The received powers obtained in the first measurement were used for calculating the reward at BS 1 while those obtained in the second measurement are used for calculating that at BS 2.

A mmWave transmitter, a measurement device, and a camera are deployed as shown in Fig. 4.16. The transmitter was considered to be the UE throughout the measurements. The measurement device and camera were considered as BS 1 and camera 1, respectively, in the first measurement, while in the second measurement, they were considered BS 2 and camera 2, respectively. The mmWave transmitter transmitted signals at a carrier frequency of 60.48 GHz and subsequently, the measurement device measured the power of a part of the signals as discussed in Chapter 3. The transmitted signals were considered as uplink signals from the UE to BS 1/BS 2. In the first measurement, two pedestrians walked along the moving path in Fig. 4.16(a) and blocked the path between the transmitter and the mea-

(a) Camera image on BS 1 side

(b) Camera image on BS 2 side

Figure 4.17: Images obtained in each measurement. ©2020 IEEE

surement device. Similarly, in the second measurement, a pedestrian walked along the moving path in Fig. 4.16(b).

Simulation Procedure of Decision Process

The camera images and received powers are divided into two parts to perform learning and performance evaluation based on different sets of data. Let the camera images and received powers obtained in the ith measurement be denoted by $\left(x_t^{(i)}\right)_{t\in\mathcal{T}}$ and $\left(P_t^{(i)}\right)_{t\in\mathcal{T}}$, respectively, where $x_t^{(i)}$ denotes the tth image obtained in the ith measurement, $P_t^{(i)}$ denotes the received power obtained at the same time, and $\mathcal{T} = \{1, 2, \ldots, T\}$ denotes the set of time indices. The index set $\mathcal{T}$ is divided into the following two subsets: $\mathcal{T}_1 = \{1, 2, \ldots, T'\}$ and $\mathcal{T}_2 = \{T'+1, T'+2, \ldots, T\}$, where $1 < T' < T$.

The decision process in the learning procedure is simulated using $\left(x_t^{(i)}\right)_{t\in\mathcal{T}_1}$ and $\left(P_t^{(i)}\right)_{t\in\mathcal{T}_1}$ for $i \in \{1, 2\}$. The decision epoch is set as the time step in which an image is obtained. The decision process starts at the time step at which $x_N^{(1)}$ and $x_N^{(2)}$ is observed. The UE is initially associated with BS 1 and the time at which the process starts is not within a service disruption time, i.e., $j_N = 1$ and $c_N = 0$. Thus, the initial state s_N is set to $\left(x_N^{(1)}, \ldots, x_1^{(1)}, x_N^{(2)}, \ldots, x_1^{(2)}, 1, 0\right)$. The action a_N is selected according to the ϵ-greedy policy that is widely used in the learning phase in RL [25]; then, the next state s_{N+1} is set such that it contains the images $\left(x_{N+1}^{(1)}, \ldots, x_2^{(1)}, x_{N+1}^{(2)}, \ldots, x_2^{(2)}\right)$, j_{N+1}, and c_{N+1}, where j_{N+1} and c_{N+1} are determined based on a_N. The procedure is iterated and then ended when the state contained the last images $x_{T'}^{(1)}$ and $x_{T'}^{(2)}$.

The performance metric $R_{t+1}^{(j_{t+1})}$ for $j_{t+1} \in \mathcal{J}$ and $t \in \mathcal{T}_1$ in (4.3) is set as the data rate of the link between BS j_{t+1} and the UE, and is calculated as follows: The performance metric $R_{t+1}^{(j_{t+1})}$ is calculated by the Shannon capacity formula via the obtained received power value $P_{t+1}^{(j_{t+1})}$ as follows:

$$R_{t+1}^{(j_{t+1})} = W_{j_{t+1}} \log_2 \left(1 + \frac{P_{t+1}^{(j_{t+1})}}{\sigma^2 W_{j_{t+1}}} \right),$$

where σ^2 and $W_{j_{t+1}}$ denote the noise power spectral density and measurement bandwidth in the j_{t+1}th measurement, respectively. Note that W_1 is set as 40 MHz whereas W_2 is set as 20 MHz.

Subsequently, the performance of the learned policy is evaluated. A decision process is simulated using the same procedure as the learning procedure with the exception that $\left(x_t^{(i)}\right)_{t \in \mathcal{T}_2}$ and $\left(P_t^{(i)}\right)_{t \in \mathcal{T}_2}$ for $i \in \{1, 2\}$ is used, and the action is selected so that the learned optimal action-value in (2.7) is maximized. The time average of the reward is calculated as a performance metric of the learned policy.

The learning and evaluation is iterated by using the same dataset. The policy that achieved the highest average reward throughout the iterations is evaluated.

Compared Framework

The proposed multi-camera operation is compared with a single-camera operation. To ensure fair comparison, the decision process in a single-camera operation is designed by formulating a same decision process similar as discussed in the previous section—the images from multiple cameras in the definition of the state is replaced with the images from a single camera—and under this process,a handover policy is learned by deep RL.

In this decision process, the network controller was blind to pedestrian 3. Through the comparison, it is validated that with the multi-camera operation, the blockage effects caused by pedestrian 3 were successfully predicted; thereby showing the feasibility of the multi-camera operation in the image-based handover framework.

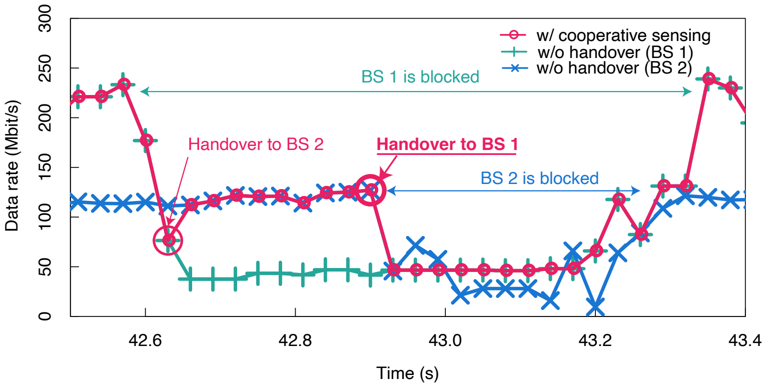

(a) In multi-camera operation. Handover to BS 2 was triggered at 42.63 s and handover to BS 1 was triggered at 42.90 s.

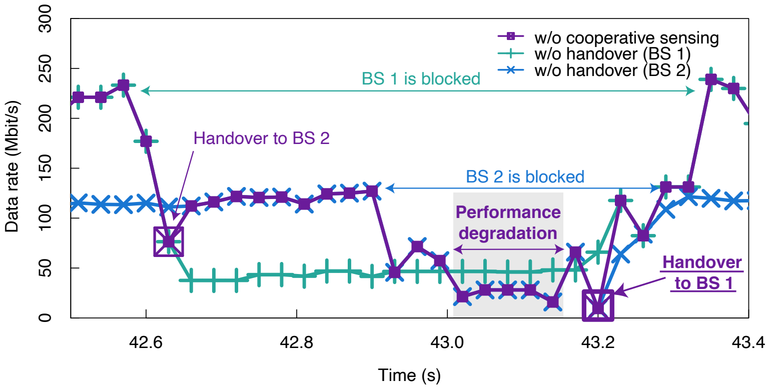

(b) In single-camera operation. Handover to BS 2 was triggered at 42.63 s and handover to BS 1 was triggered at 43.20 s.

Figure 4.18: Comparison between multi-camera operation and single-camera operation in terms of time series of data rate for service disruption time $T_{\text{dis}} = 0\,\text{s}$. ©2020 IEEE

Results

In Fig. 4.18, it is validated that camera 2 compensated for the blind spot of camera 1; thereby predicting blockage effects caused by the pedestrian 3 who is out of the coverage of camera 1. Fig. 4.18 shows an example of the time series of the data rate for the service disruption time $T_{\text{dis}} = 0\,\text{s}$. The data rate of the link between BS 1 and the UE was degraded approximately

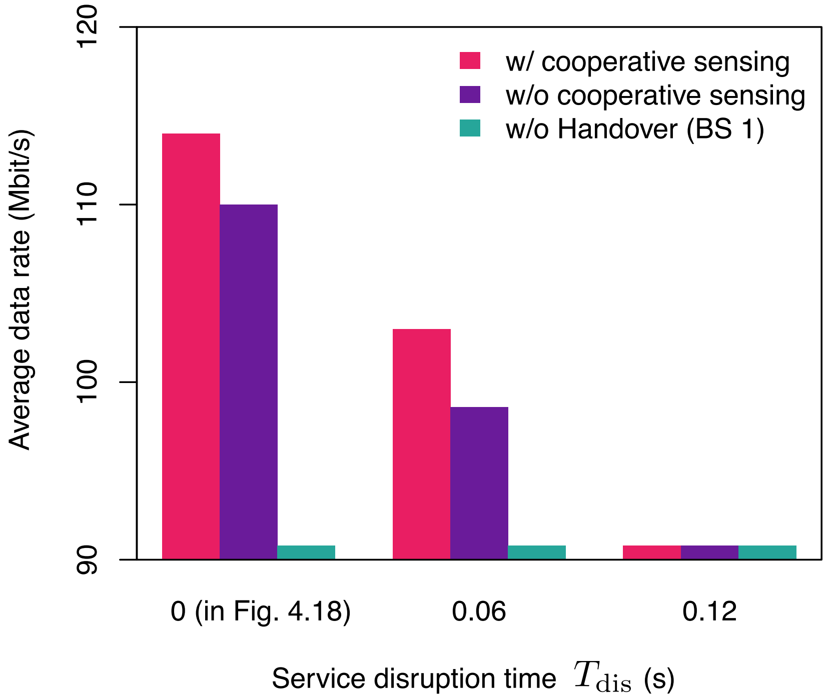

Figure 4.19: Average data rate in Fig. 4.18 for different service disruption. ©2020 IEEE

from 42.6 s to 43.3 s and that of the link between BS 2 and the UE was degraded approximately from 42.9 s to 43.4 s. Both frameworks successfully avoided the blockage effect in BS 1 by triggering a handover to BS 2[7]. However, the framework without camera 2 remained to associate with BS 2 despite of the blockage in BS 2; hence experiencing greater degradation in the data rate relative to associating with BS 1. Meanwhile, in the multi-camera operation, the network controller triggered a handover from BS 2 to BS 1 earlier and successfully avoided the degradation.

Fig. 4.19 confirms that the cooperative sensing with the multiple cameras contributed to performance enhancement. Fig. 4.19 shows the data rate

---

[7] The handover to BS 2 was not triggered in a proactive fashion. This could be attributable to the fact that the data rate of the link between the UE and BS 2 was much lower than that between the the UE and BS 1. In the situation, a proactive handover did not contribute to the performance maximization; thus, the network controller triggered a handover in a reactive manner.

averaged over the duration plotted in Fig. 4.18 for different service disruption time T_{dis}. When $T_{\text{dis}} = 0\,\text{s}$ and $0.06\,\text{s}$, the framework with multi-camera operation outperformed the framework with single-camera operation. The average data rate in the framework with the multi-camera operation was at most 5.10% higher than that with the single-camera operation.

It should be notable that without explicitly estimating the positions/velocities of the pedestrians, one could learn the handover policy that led to performance enhancement in the multi-camera operation. Thus, the results indicate the feasibility of adopting the cooperative sensing with multiple cameras to the image-based handover framework.

Fig. 4.19 also shows that in a longer service disruption, i.e., when $T_{\text{dis}} = 0.12\,\text{s}$, the average data rate in the both framework is equivalent to the average data rate in the link between the BS 1 and the UE. The characteristic is attributed to the fact that the both frameworks do not trigger a handover because a handover does not contribute to the performance maximization.

4.7 Conclusion

This chapter presented a new paradigm for leveraging time-consecutive camera images in handover decision problems for realizing the proactive prediction of future long-term performances. First, it is experimentally noted that the obstacle-caused data rate degradation in mmWave links cannot necessarily be predicted in a proactive manner based only on the time-variation of the received powers before the degradation. To solve this problem, this chapter proposed the expansion of the state space in order for the state information to comprise consecutive camera images, which comprise informative features for proactively predicting long-term data rates in mmWave links. To overcome the difficulty of the higher dimensionality of the expanded state space, deep RL is used for predicting the cumulative sum of the future data rates and deciding handover timings based on the predicted values. By performing deep RL using the state information of experimentally obtained camera images, it was confirmed that the state expansion allows the prediction of future obstacle-caused data rate degradation from approximately 500 ms before the degradation occurs. Evaluated the time-average of the data rates over approximately two minutes, it was revealed that the proposed expansion of the state space resulted in a performance gain.

Chapter 5

Multimodal Split Learning for mmWave Received Power Prediction

5.1 Overview

Wireless communication systems can benefit from peripheral data source information in addition to the RF signal domain, such as location, motion sensory data, and camera images [67, 80–83]. Incorporating these non-RF modalities can complement insufficient features in RF signals, enabling more accurate handover decisions [82], received power predictions [67], and so on. In view of this, this chapter focuses on the problem of millimeter-wave (mmWave) uplink received power prediction by efficiently integrating the received mmWave RF signal powers and depth camera images.

As shown in the previous chapter, depth image-based prediction exploiting ML reaches proactive predictions of LoS blockage events by recognizing mobility blockage patterns to detect sudden changes between LoS and non-LoS conditions, which is hardly observable from received mmWave signal powers. By contrast, current received mmWave signal powers are useful for predicting short-term received power fluctuations for a given LoS or NLoS condition [11]. To reach their full potential, the of this chapter goal is to fuse both RF received powers and depth images in an ML-based received

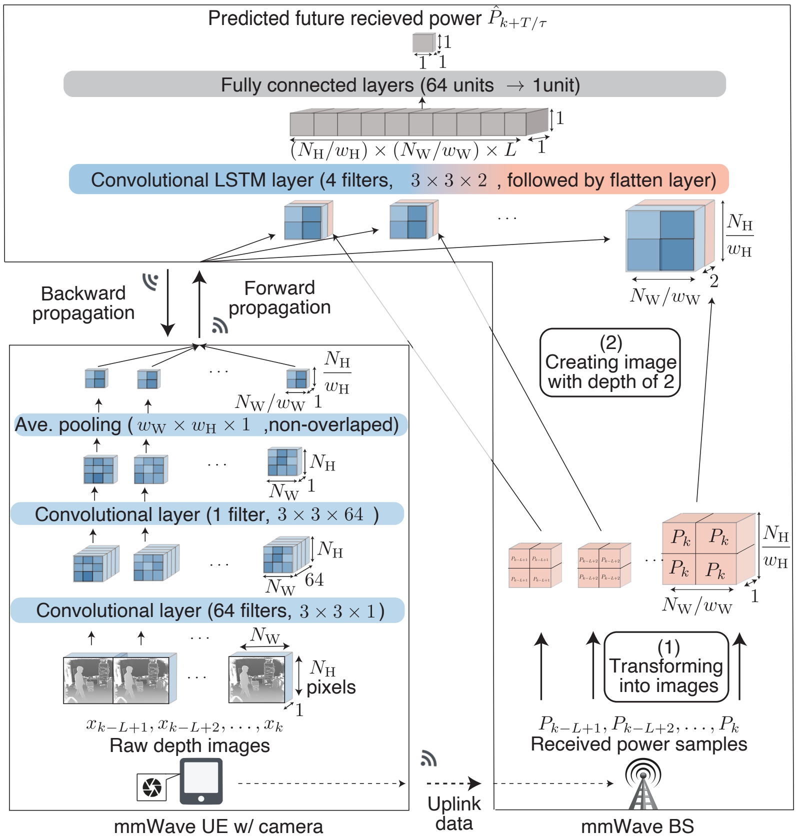

Figure 5.1: NN architectures for proposed received power prediction leveraging MultSL based on both depth images and RF received powers (Img+RF). ©2020 IEEE

power prediction.

There are two key challenges in acquiring depth images: communication latency and privacy violation. The first challenge is due to the fact that depth images are not necessarily obtained in the same location of the RF received power. The physical separation necessitates communication between the entity holding the images (e.g., UE or surveillance cameras) and that holding RF received powers (e.g., BSs) over a limited wireless bandwidth, and this can cause a severe latency in the collection of depth images. However, numerous applications for mmWave communications are delay-sensitive (e.g., VR [84]). Hence, it is important to design a prediction framework with lower communication latency for acquiring depth images.

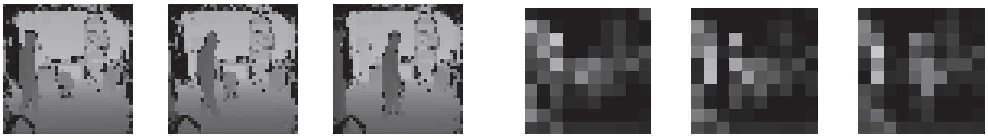

(a) Raw Images (b) $w_{\mathrm{H}} \times w_{\mathrm{W}}$: 4×4

(c) $w_{\mathrm{H}} \times w_{\mathrm{W}}$: 10×10 (d) $w_{\mathrm{H}} \times w_{\mathrm{W}}$: 40×40

Figure 5.2: Raw depth-images and output images of trained convolutional layers in MultSLs with different pooling dimension $w_{\mathrm{H}} \times w_{\mathrm{W}}$. Trained convolutional layers extract the image feature representations according to the given pooling dimensions. ©2020 IEEE

The second challenge is due to the fact that depth images may also involve privacy-sensitive information, e.g., the travel history of people in the view of cameras. Therefore, acquiring raw depth images violates the privacy of the pedestrians who block mmWave links, which motivates to design a framework to perform received power prediction in a privacy-preserving manner.

To address the aforementioned challenges, this chapter proposes a communication-efficient and privacy-preserving *multimodal split learning (MultSL)* framework. Exploiting a split NN architecture [22], without sharing raw data, MultSL combines RF and image modalities by only exchanging NN activations and gradients (Fig. 5.1). Before exchanging NN activations, the last activations for the image modality are compressed (see Fig. 5.2), achieving higher communication efficiency while preserving more data privacy. Surprisingly, experimental evaluations show that the compression is beneficial for balancing the fusion between RF and image modalities. Consequently, the MultSL with an optimal compression rate achieves higher accuracy, compared not only to baseline schemes based solely on either mmWave received powers (`RF`, Fig. 5.3(a)) or images (`Img`, Fig. 5.3(b)), but also to the MultSL without compression.

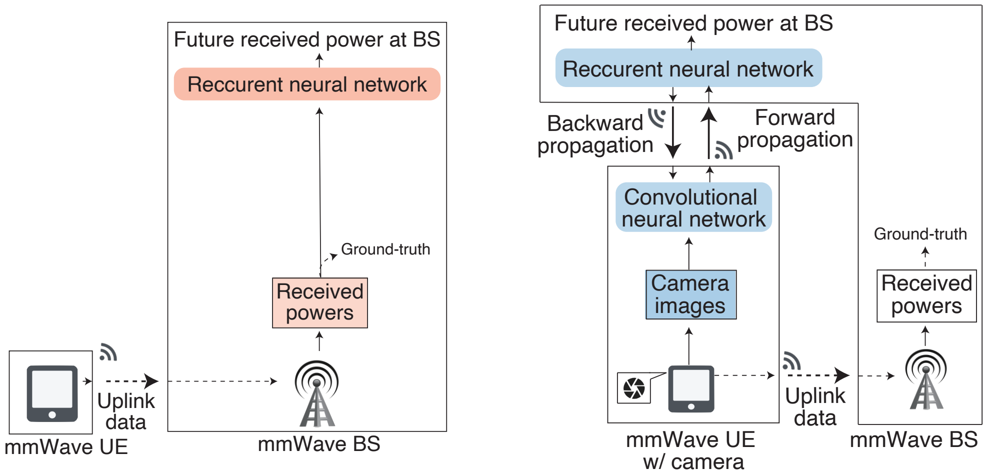

(a) Baseline 1: RF (b) Baseline 2: Img

Figure 5.3: Neural network (NN) architectures for baseline received power prediction frameworks: based solely on (a) previously received RF signal powers (RF) and on (b) depth images (Img). ©2020 IEEE

5.2 Related Works

RF or non-RF Single Modality-based Wireless Systems. For handover or positioning, RF-modalities, e.g., received power or channel state information, were studied [50, 56]. For mmWave received power prediction, handover, prior studies in [64, 67] leverage visual data to detect sudden LoS-and-NLoS transitions due to moving obstacles [31, 33]. While these aforementioned works demonstrate the feasibility of wireless systems benefitting from RF or non-RF modality, these works focus on the usage of a single modality. Unlike these works, this chapter focuses on the problem of fusing heterogeneous modalities, i.e., RF-signals and visual data. Moreover, in contrast to these studies which do not take into account privacy in collecting visual data, this chapter integrates RF and multiple visual data in a privacy-preserving manner.

RF and non-RF Modality Fusion. Fusing RF and non-RF modalities, e.g., vision modalities, is proposed mainly in positioning of human pedestrians or robots to enhance prediction accuracy [85–88]. Therein, visual data is leveraged to achieve the best positioning accuracy while RF signals compensate for occluded cameras. These works combine visual and RF modalities by simply taking weighted averages of the prediction results made with each modality [85] or leveraging dual-stream convolutional neural networks (CNNs) [88]. Besides positioning, a seamless handover mechanism is proposed by fusing GPS information of mobile terminals and received signals from the mobile terminals [82]. However, these studies do not consider the privacy in collecting highly private sensitive information, e.g., trajectory of humans viewed in visual data or mobile users tracked by GPS. Unlike these studies, this chapter studies how to benefit from fusing RF-signals and visual data in a privacy-preserving manner by leveraging a collaborative learning framework.

Federated Learning (FL). Collaborative learning frameworks exemplified by FL [20, 21, 89], have recently attracted an increasing interest. The key feature of collaborative learning is to train machine learning models in a distributed manner without sharing raw data samples, thereby preserving data privacy. In classical FL, data owners hold and train ML models locally, and model parameters, e.g., the weight parameter of NN models, are averaged using a central server [89] or other data owners [90], after which these shared model parameters are integrated. This prevents data owners from sharing raw data while enabling collaborative model training.. Several communication-efficient FL algorithms have been proposed such as NN pruning [91], gradient compression [92, 93], and output distillation [94]. However, FL suffers from the challenging non-IID problem coming from the heterogeneity of data distribution across data owners. Although the initial work regarding FL in [89] alleviates the issue by increasing the number of local training iterations, this approach does not solve the issue when data distributions are totally different from one another. In view of this, this chapter aims at providing a more efficient collaborative learning framework leveraging the idea of split learning, that benefits from multiple modalities wherein the data distributions are totally different. For a comprehensive survey and tutorial of federated learning and its applications, readers are encouraged to read [20, 21].

Split Learning. As another approach for collaborative learning, SL has been proposed in [22,95]. The key idea behind SL is to split the NN models on a per-layer basis and distribute a lower segment into data owners and an upper segment into another central entity. Therein, the data owner does not need to exchange raw data but instead exchanges NN activations with the central entity during training. In [95], the authors conceptualized the fusion of multiple modalities with totally different data distributions, enabling privacy preserving model training. However, this was a concept-level discussion, and the feasibility of applying SL based on multiple modalities to wireless systems was not investigated. Particularly, the design of communication efficient SL remains an open problem, which is of importance because NN layer segments are interconnected wirelessly with a limited bandwidth, and some entities holding an NN segment are resource-limited, e.g., wireless cameras or mobile devices. To fill these voids, this work aims at designing an SL framework by fusing RF and visual data, while enabling model training in a communication efficient manner.

5.3 MultSL for Future Received Power Prediction

The MultSL structure is illustrated in Fig. 5.1, in which a convolutional LSTM NN is split and distributed across a UE and its associated BS. In Fig. 5.1, $k \in \mathbb{N}$ denotes the time index, x_k denotes the observed image, P_k denotes the corresponding received power in the uplink signal, and τ denotes the time-interval between successive images. The UE is equipped with a depth camera whose captured images $x_{k-L+1}, x_{k-L+2}, \ldots, x_k$ are processed by convolutional layers and then uploaded to the BS, where L denotes the length of an image sequence. The BS stores an LSTM layer where the uploaded images are integrated with the uplink mmWave RF signal powers $P_{k-L+1}, P_{k-L+2}, \ldots, P_k$ received by the BS. By processing the integrated image and RF data at the last fully connected layer, the BS can predict its future mmWave received power $P_{k+T/\tau}$ with a look-ahead time T.

For training MultSL, the UE sends the output of its convolutional layers, termed a forward propagation (FP) signal to the BS. Based on the FP signal, the BS subsequently calculates the gradients of the weight parameters in its own NN and sends the gradients, termed a backward propagation (BP) signal, back to the UE. Finally, based on the BP signal, the UE updates the weight parameters of the convolutional layers.

The communication of the FP/BP signals is performed over a wireless channel. This chapter considers that the FP/BP signals are transmitted via the mmWave channel over which the aforementioned uplink signals are transmitted to achieve smaller transmission delay through exploiting a wider bandwidth in the mmWave channel. Section 5.5 further details the mmWave communication channel.

MultSL is compared with two baselines based solely on a single-modality as shown in Figs. 5.3(a) and 5.3(b). The former baseline termed as RF is based only on consecutive received powers in which the LSTM layer and fully connected layer are located at the BS, and training is performed at the BS. The latter baseline, termed as Img is based only on consecutive images, in which the entire NN is split similarly in MultSL.

5.4 Compression of CNN Output via Pooling Towards Communication Efficiency and Privacy Preservation

In addition to prediction accuracy, MultSL involves the following two key metrics: over-the-air latency for transmitting FP signals and data privacy [22]. Hence, it is important to optimize the operation of MultSL such that both latency and privacy leakage are minimized without compromising the prediction accuracy.

It can be noticed that increasing the pooling dimension $w_{\mathrm{W}} \times w_{\mathrm{H}}$ in the convolutional layer: i.e., the compression intensity of the convolutional layer output, is suitable for reducing both the latency and privacy leakage. Given that the pooling dimension is $w_{\mathrm{W}} \times w_{\mathrm{H}}$, and pooling regions are non-overlapping (i.e., the horizontal and vertical strides are $N_{\mathrm{W}}/w_{\mathrm{W}}$ and $N_{\mathrm{H}}/w_{\mathrm{H}}$, respectively), the number of pixels to be forwarded to the BS is $LN_{\mathrm{W}}N_{\mathrm{H}}/w_{\mathrm{W}}w_{\mathrm{H}}$ as shown in Fig. 5.1. Thus, the payload size of FP signals

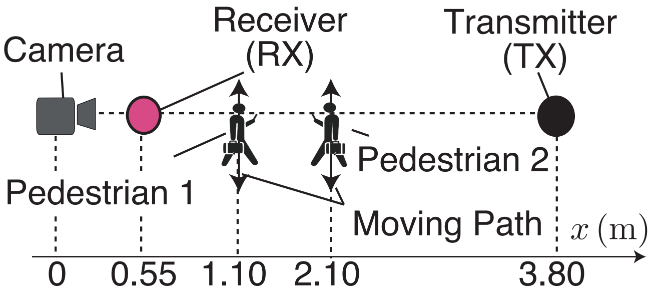

Figure 5.4: Experimental environment for measuring the communication channel and depth image data, in which a pair of mmWave transmitter and receiver is blocked by two moving pedestrians. ©2020 IEEE

and the consequent over-the-air latency for transmitting them can be reduced by increasing the pooling dimension. Moreover, the privacy leakage may be reduced by the increase of pooling dimension since compressed images make it harder to see what the images reflect (as depicted in Fig. 5.2). The next section experimentally demonstrates that an increasing pooling dimension yields a smaller latency and privacy leakage.

5.5 Experimental Evaluation

5.5.1 Setting

Datasets. The prediction accuracy achieved by the proposed MultSL is evaluated using the data set of received powers and depth images [67]. The experimental environment is shown in Fig. 5.4. A transmitter (TX), receiver (RX), and camera are deployed. As the TX, a commercial product of IEEE 802.11ad access points is utilized. As the RX, the measurement system developed in the chapter 3 is utilized. The usage of this measurement system is because it is validated to be capable of measuring the time-variance of the mmWave received powers due to moving obstacles, which is essential to train the NN models in Fig. 5.1 [67]. The TX transmits signals at the carrier frequency of 60.48 GHz towards the RX, and two pedestrians walk across the path between the TX and RX. The camera (Kinect®sensor [73]) obtains depth images viewing the two pedestrians with the resolution of 512 × 480 and with the interval of successive image frames τ of 33.3 ms. The obtained images are compressed to have a pixel resolution of $N_{\mathrm{W}} \times N_{\mathrm{H}} = 40 \times 40$. The details of the measurement are discussed in [67].

Training, Validation, and Test. The training, validation, and test are performed with datasets that differ from one another. It is noted that the validation is performed *during training* to monitor the prediction accuracy while preventing overfitting. The test is performed *after training* to evaluate the final performance of the trained model. The procedures are both commonly performed in ML [17]. Let $k \in \mathcal{K}$ denote the time-index of the image and received power samples obtained in the aforementioned measurement with $\mathcal{K} = \{1, 2, \ldots, 15325\}$. Training, validation, and test are performed with samples whose time-index is in the index set $\mathcal{K}_{\text{train}}$, $\mathcal{K}_{\text{valid}}$, and $\mathcal{K}_{\text{test}}$, respectively, wherein $\mathcal{K}_{\text{train}} \cup \mathcal{K}_{\text{valid}} \cup \mathcal{K}_{\text{test}} = \mathcal{K}$. In this evaluation, the ratio of $|\mathcal{K}_{\text{train}}|$ and $|\mathcal{K}_{\text{valid}}|$ is set as 75% and 25%, respectively, and that of $|\mathcal{K}_{\text{train}}|$ and $|\mathcal{K}_{\text{test}}|$ is set as 80% and 20%, respectively; hence, $\mathcal{K}_{\text{train}} = \{1, 2, \ldots, 9928\}$, $\mathcal{K}_{\text{valid}} = \{9929, 9930, \ldots, 13228\}$, and $\mathcal{K}_{\text{test}} = \{9929, 9930, \ldots, 15325\}$.

The training is performed such that the mean square error (MSE) between the predicted and actual received powers is minimal. Let the actual received power at the time-index k be denoted by P_k. Given pooling dimension $w_{\mathrm{W}} \times w_{\mathrm{H}}$, the following optimization problem is solved:

$$\underset{\theta}{\text{minimize}} \quad \frac{1}{|\mathcal{K}_{\text{train}}|} \sum_{k \in \mathcal{K}_{\text{train}}} \left(\hat{P}_{k+T/\tau}^{(\theta, w_{\mathrm{W}}, w_{\mathrm{H}})} - P_{k+T/\tau} \right)^2, \tag{5.1}$$

where $\hat{P}_{k+T/\tau}^{(\theta, w_{\mathrm{W}}, w_{\mathrm{H}})}$ denotes the predicted received power values with the look ahead time $T = 120\,\mathrm{ms}$ given the trained NN parameters θ and pooling dimension $w_{\mathrm{W}} \times w_{\mathrm{H}}$. Note that $\hat{P}_{k+T/\tau}^{(\theta, w_{\mathrm{W}}, w_{\mathrm{H}})}$ is calculated from the input of sequential images $x_{k-L+1}, x_{k-L+2}, \ldots, x_k$ and received powers $P_{k-L+1}, P_{k-L+2}, \ldots, P_k$ with the sequence length of $L = 4$. The problem is solved with the Adam optimizer [96] with the learning rate of 1.0×10^{-3}, the decaying rate parameters $\beta_1 = 0.9$ and $\beta_2 = 0.999$, and the batch size of 64. The training is continued until 50 training epochs (156 stochastic gradient descent steps) are iterated. In the MultSL and the baseline frameworks that are subsequently discussed, both UE and BS trained their NN layers, i.e., performed forward and backward calculations in parallel computing via exploiting an Nvidia Tesla T4 GPU with 2560 cores with memory corresponding to 16 GB and memory bandwidth corresponding to 320 GB/s.

FP/BP Communication Channel. FP/BP signals are assumed to be transmitted over the mmWave channel. Under this channel, an NLoS event decreases the received power by around 15 dB compared to the values in LoS conditions, and lasts for 200-300 ms. The LoS-NLoS transition occurs within 50–200 ms. An exemplary snapshot capturing these channel characteristics is illustrated in Fig. 5.6.

Baselines. The proposed prediction framework is compared with two baselines that depend solely on either image sequences or received power sequences. In the former baseline, termed as Img, only the output of the convolutional layers are fed into the convolutional LSTM layer. In the latter baseline, termed as RF, only the received power values are fed into the convolutional LSTM layer. Hereinafter, the proposed multimodal prediction framework is denoted as Img+RF to explicitly indicate that the proposed framework utilizes both images and received power values for the prediction.

It is noted that the objective of the comparison is to demonstrate the improvement in accuracy from using the other modality *in addition to* a single modality. Hence, although there are differences in input data sizes, Img+RF uses 8 inputs (image and received power sequences wherein each exhibits a length of 4) while Img and RF use 4 inputs (image or received power sequence with a length of 4).

5.5.2 Performance Metrics

Prediction Accuracy. Prediction accuracies in validation and test are evaluated using the root MSE (RMSE). Given the predicted received powers $\left(\hat{P}_{k+T/\tau}^{(\theta,w_{\mathrm{W}},w_{\mathrm{H}})}\right)_{k\in\mathcal{K}_j}$ in the trained parameters θ and pooling dimension $w_{\mathrm{W}} \times w_{\mathrm{H}}$ where $j \in \{\mathrm{valid}, \mathrm{test}\}$, the RMSE is given as follows:

$$\mathrm{RMSE} = \sqrt{\frac{\sum_{k\in\mathcal{K}_j}\left(\hat{P}_{k+T/\tau}^{(\theta,w_{\mathrm{W}},w_{\mathrm{H}})} - P_{k+T/\tau}\right)^2}{|\mathcal{K}_j|}}, \tag{5.2}$$

where the RMSEs for j = valid and j = test are referred to as validation RMSE and test RMSE, respectively. The validation RMSE is calculated for each training epoch.

FP/BP Transmission Latency. The latency for transmitting FP/BP signals is calculated as follows. Let $(P_k)_{k\in\mathcal{K}}$ denote the measured time-varying received power values. The shorthand notations $[k]$ is used to denote the interval $[(k-1)\tau', k\tau']$ for $k \in \mathcal{K}$, where $\tau' = 33.3\,\mathrm{ms}$ denotes the interval between the successive received power samples. Given that the pooling is performed with the pooling dimension of $w_{\mathrm{W}} \times w_{\mathrm{H}}$, the latency for transmitting FP signals within the interval $[k]$ is denoted by $T_{\mathrm{FP}}[k]$ and is calculated as follows:

$$T_{\mathrm{FP}}[k] = \frac{L(N_{\mathrm{H}}/w_{\mathrm{H}})(N_{\mathrm{W}}/w_{\mathrm{W}})R}{W\log_2(1+P_k/\sigma^2 W)}, \tag{5.3}$$

where $\sigma^2 = -173\,\mathrm{dBm/Hz}$ denotes the noise power spectral density, $R = 32$ denotes the number of bits for one pixel, and $W = 40\,\mathrm{MHz}$ is the measurement bandwidth. Likewise, the latency for transmitting BP signals within the interval $[k]$ is denoted by $T_{\mathrm{BP}}[k]$ and is calculated as follows:

$$T_{\mathrm{BP}}[k] = \frac{N_{\mathrm{layer2}}R'}{W\log_2(1+P_k/\sigma^2 W)}, \tag{5.4}$$

where $N_{\mathrm{layer2}} = 576$ denotes the number of weights in the upper convolutional layer, and $R' = 32$ denotes the number of bits required for representing the BP gradients. The time duration during which a stochastic gradient step is performed within the interval $[k]$ is denoted by $T_{\mathrm{step}}[k]$ and is given by $T_{\mathrm{FP}}[k] + T_{\mathrm{BP}}[k] + T_{\mathrm{comp}}$, where T_{comp} is the sum of time duration for calculating the FP/BP signals.

It should be noted that the training speed is affected by $T_{\mathrm{step}}[k]$, and the impact of the pooling dimension on the training speed is also evaluated. For that, the time elapsed until which the nth stochastic gradient descent step is performed is calculated and its corresponding validation accuracy is plotted. Let $N[k] := \lfloor \tau'/T_{\mathrm{step}}[k] \rfloor$ denote the maximum number of stochastic gradient steps performed within $[k]$. The nth stochastic gradient descent step is performed in a certain interval, whose index is defined as k_n and is given by $\max\{\, k' \mid \sum_{k=1}^{k'} N[k] \le n \,\}$. The time elapsed until the nth

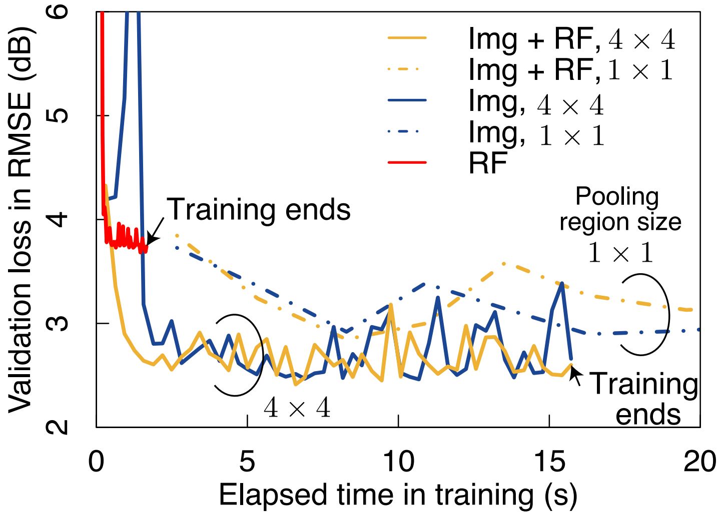

Figure 5.5: Impact of pooling dimension on validation accuracy in training. In Img+RF and Img, the larger pooling dimension results in the faster improvement on validation accuracy. ©2020 IEEE

stochastic gradient descent step is performed, denoted by T_n, is calculated as follows:

$$T_n = \sum_{k=1}^{k_n-1} T_{\text{step}}[k] + \left(n - \sum_{k=1}^{k_n-1} N[k] + 1 \right) T_{\text{step}}[k_n]. \tag{5.5}$$

Privacy Leakage Level. As the convolutional layer output becomes more similar to the input images, privacy is increasingly violated. Thus, the privacy leakage level is quantified with the inverse of the similarity between each raw image sample x_k and its CNN output. Let $\phi(x_k)$ denote the CNN output resized such that it involves the same number of pixels as that in x_k via nearest neighbor interpolation. For measuring a similarity between x_k and $\phi(x_k)$, the Euclidean-distance multidimensional scaling algorithm [97] is utilized, where the low-dimensional representations of these images are embedded to an Euclidean-space, and the similarity between these images is quantitatively represented by the Euclidean-distance. Given the measured distance $d(x_k, \phi(x_k))$, the privacy leakage is given as: $1/\max_{k \in \mathcal{K}_{\text{val}}} d(x_k, \phi(x_k))$.

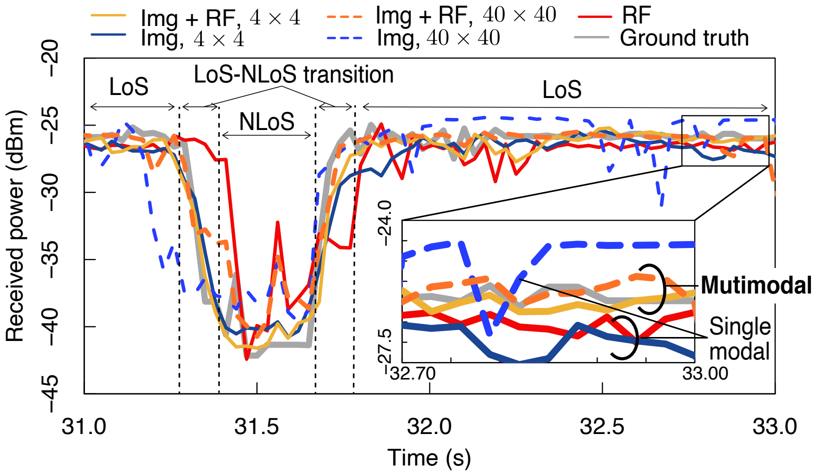

(a) Received power predicted 120 ms prior to the observation when pooling dimensions correspond to 4 × 4 and 40 × 40.

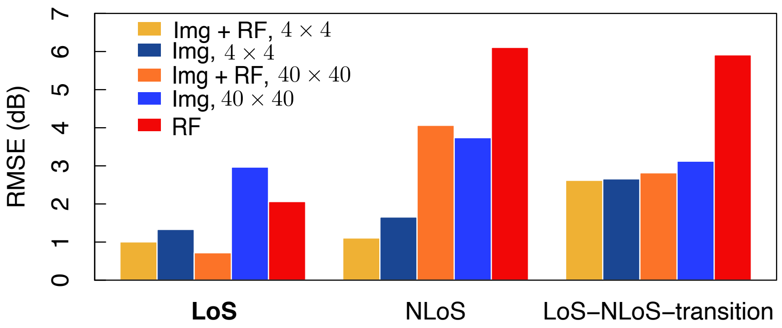

(b) RMSE in different channel conditions.

Figure 5.6: Received power prediction results after training. ©2020 IEEE

5.5.3 Results and Discussions

Validation Accuracy in Training. First, the impact of the pooling dimension on the validation accuracies during training is analyzed. Fig. 5.5 shows the time progress of the validation accuracy in RMSE in training. In Img+RF and Img, the pooling dimensions of 4×4 and 1×1 were examined. The computation time T_{comp} in either Img+RF and Img was 1.00 ms while that in RF was 0.21 ms. The computation time T_{comp} in Img+RF and Img are same within the measurable accuracy (at second decimal digit); hence T_{comp}

is treated as of the same value as 1.00 ms in Fig. 5.5 [1]. The computation time is obtained by measuring the time-duration during which the aforementioned GPU computes updates of all model parameters in a stochastic gradient descent step. In the pooling dimension of 4 × 4, the improvement in RMSE is faster compared to the training with the pooling dimension of 1 × 1. This is attributed to the shorter $T_{\mathrm{FP}}[k]$ in the pooling dimension of 4×4 relative to that in 1×1, wherein more stochastic gradient descent steps can be performed within a certain period. The model in RF can be trained 8x faster than that in either Img+RF and Img with the pooling dimension of 4 × 4. This faster training is because the training in RF does not involve communication of FP/BP signals, i.e., $T_{\mathrm{FP}}[k] = T_{\mathrm{BP}}[k] = 0$, $\forall k \in \mathcal{K}$. However, the RMSE reaches approximately 3.7 dB, which corresponds to the poorer prediction performance compared to Img+RF and Img wherein the RMSE ranges from 2.7 dB to 3.0 dB.

Prediction After Training. It is shown that the received powers predicted by Img + RF match the actual received powers better than the Img and RF baselines. Fig. 5.6(a) shows the time series of the actual received powers and of the received powers predicted 120 ms before the actual powers were observed. In Img+RF and Img, the models with the pooling dimensions of 4 × 4 and 40 × 40 are examined as an example. First, RF did not match the ground truth as accurately as Img+RF and Img in particular NLoS conditions. Focusing on LoS conditions (a zoomed-in view in Fig. 5.6(a)), Img+RF matches the ground truth more accurately than Img, which corresponds to the advantage of Img+RF over Img. This is also quantitatively validated in Fig. 5.6(b) showing the RMSE in LoS, NLoS, and LoS-NLoS-transition conditions in the time-duration in Fig. 5.6(a), where one can see that the RMSE in Img+RF under a LoS condition is smaller

---

[1] The same computation time within the measurable accuracy is due to a much higher computational complexity in the convolutional layers shared between Img+RF and Img compared to one in the other upper layers. By counting the multiplying operation in a forward propagation, one can see that the computational complexity in the convolutional layers is approximately 10–100x higher than that in the other upper layers. Hence, the computation in the convolutional layers is dominant, and this is the reason for the almost same computation time.

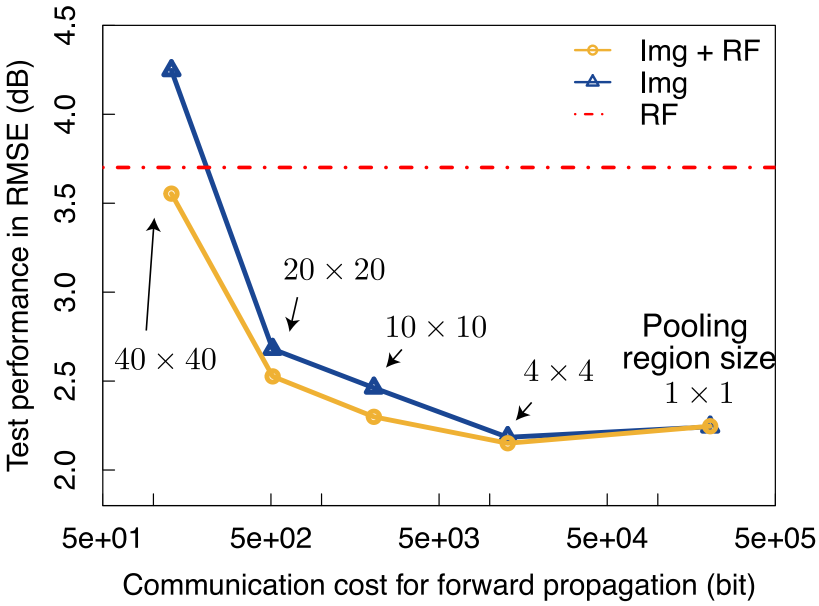

Figure 5.7: Test RMSE in different pooling dimension and consequent communication cost for transmitting FP signals. ©2020 IEEE

than that in Img. This can be attributed to the invariance of received powers under LoS conditions. In LoS conditions, the input of current received powers in Img+RF exhibits a value similar to future received power values and can be considerably informative in terms of predicting the future received power values. Hence, Img+RF predicted future received power values more accurately under LoS conditions than Img.

Test Accuracy vs. Latency and Privacy Leakage. Fig. 5.7 shows the impact of the pooling dimension on the RMSE and communication costs during inference. Drawing an inference requires a single FP transmission whose payload size is calculated by $L(N_{\mathrm{H}}/w_{\mathrm{H}})(N_{\mathrm{W}}/w_{\mathrm{W}})R$. The FP communication cost is monotonically decreased with the pooling dimension, and is minimized when the UE output is maximally compressed (i.e., 40×40 pooling dimension). By contrast, the prediction accuracy is convex-shaped over the pooling dimension. The maximum accuracy (i.e., minimum RMSE) is achieved when the UE output is 93% compressed (i.e., 4×4 pooling dimension), at which both accuracy and communication efficiency are improved compared to the case without compression (i.e., 1×1 pooling dimension).

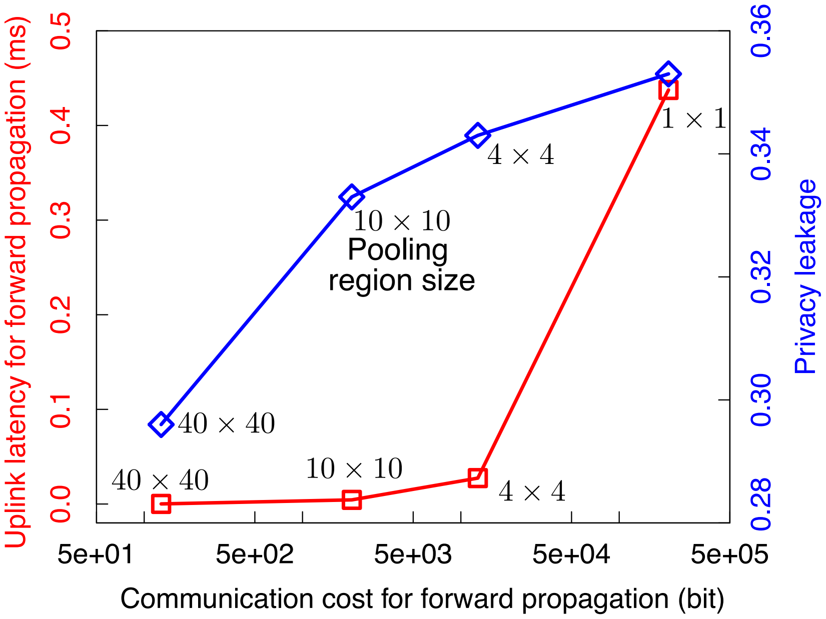

Figure 5.8: Uplink latency for transmitting FP signals and privacy leakage in different pooling dimensions. ©2020 IEEE

This counter-intuitive result is because the very large UE output dimension makes the LSTM layer biased only towards the image sequences while almost ignoring the received power sequences, highlighting the importance of balancing image and RF modalities.

Fig. 5.8 shows the impact of pooling dimension on the privacy leakage level as well as the uplink latency for uploading the FP signals. As the pooling dimension becomes larger, the raw image is converted to one with the smaller pixel resolutions as depicted in Fig. 5.2, which yields the lower latency and privacy leakage. Specifically, in the pooling dimension of 4×4, uplink latency and privacy leakage are reduced by 93% and 2.8%, respectively compared to the case of pooling dimension of 1×1 (i.e., without compressing the convolutional layer output).

5.6 Conclusions

This chapter proposed MultSL in which a convolutional LSTM is split into two wirelessly connected segments to utilize both image and RF modalities for future mmWave received power prediction. With a single pair of image and RF signal sources, this chapter demonstrated that optimally compressing the image segment's output dimension reduces communication payload sizes and privacy leakage without compromising the prediction accuracy. Seeking an optimal MultSL architecture for multiple image and RF signal sources under a generic network topology could be an interesting topic for future work.

Chapter 6

Conclusions

Motivated by the idea of proactiveness and data-driven-ness, this thesis proposed visual data-driven mmWave communication systems to combat LoS blockages. First, as a methodological buidling block, this thesis provided the measurement method of RF received powers in off-the-shelf IEEE 802.11ad APs with packet-mode transmission. As main topics, this thesis examined: *1)* visual data-driven handover predicting future throughput performance subject to rapid variations of data rate, and *2)* multimodal, i.e., RF and visual data, future received power prediction that collects visual data in a communication-efficient and privacy preserving manner. More specific conclusions are elaborated below.

In Chapter 4, this thesis demonstrated the feasibility of a visual data-driven handover framework that predicts future throughput performance of each BS including rapid variations of data rate. The key characteristic obtained from using visual data was in the capability of predicting the impact of blockage events prior to the occurrence, and this led to triggering a handover prior to the occurrence. At firsthand, this thesis highlighted that such a characteristic could not necessarily be obtained in a handover framework without visual data, by implementing a received power-based handover framework. Subsequently, this thesis did not only demonstrate the feasibility of the aforementioned proactive prediction, but also confirmed that there is a throughput gain from the proactive prediction. The author believes that this knowledge sheds light on how one can fully take advantage of mmWave communications and provide reliable and high throughput connections under blockage effects.

In Chapter 5, this thesis proposed visual and RF data fusion to enhance the accuracy of future received power prediction and, at the same time, addressed the problem of preserving the privacy of persons in a field-of-view of cameras. The key idea of achieve this goal was to design MultSL where a lower segment extracted abstracted image features, and an upper segment accepted the features and integrated them with RF data inputs. Therein, the camera did not share raw visual data, which contributed to preserving the privacy. Moreover, given the MultSL, this thesis discussed how to enhance the privacy levels and communication efficiency in collecting the image features by notifying the importance of pooling dimension in the convolutional layer in lower segments. The testbed experiments demonstrated that the prediction accuracy did not necessarily trade-off with communication efficiency and privacy levels, which provided an insight into the importance of an appropriate setting of the pooling dimension. The author believes that this insight contributes to alleviating the reluctance for bringing visual data into mmWave systems.

The author would like to conclude this thesis by envisioning several deployment scenarios of visual data-driven mmWave communication systems. First, the insight provided in this thesis can be directly applied to many data-intensive applications in static environments because the evaluations are performed in such static conditions wherein the transmitter and receiver were fixed. These applications are exemplified by, though not limited to, wireless monitoring systems in a factory or data steaming to digital signages in staition concourses (Recall that the LoS blockage possesses serious negative impacts particularly in open spaces). Contrary, as for mobile scenarios, there remain several future works. In mobile scenarios, to predict blockage events, one has to track not only blockage obstacles but also mobile UEs in a camera's view. Hence, identifying and tracking the target UEs in camera images with high reliability is included in possible future works. Nevertheless, even in such mobile scenarios, the experiments and results provided in this thesis are not meaningless in the sense that these results tell that one can feasibly achieve proactive predictions of LoS blockages if such a particular problem coming from UE mobility is overcome. Given this, the author envisages that though not directly, the insights provided in this thesis apply to remote surgical operations, remote robot operation in factories or construction sites, and cooperative perception among vehicles in outdoor spaces.

It should finally be noted that some data-intensive applications are not driven by a small complaint from some particular people, but are driven by serious societal problems. For example, remote surgical operations are driven by a shortage of surgeries, cooperative perceptions among vehicles are driven by the motivation to avoid tragedic traffic accidents, and remote robot operations are driven by the safety of practitioners. Given this, the author hopes that the insights provided in this thesis motivate to solve the aforementioned future works, bring mmWave communications into heterogeneous environments, and thereby contribute to realizing a human-centric digital society driven by serious societal problems as envisioned by the concept of Society 5.0 [98].

Bibliography

[1] K. Sakaguchi, R. Fukatsu, T. Yu, E. Fukuda, K. Mahler, R. Heath, T. Fujii, K. Takahashi, A. Khoryaev, S. Nagata, et al., "Towards mmWave V2X in 5G and beyond to support automated driving," IEICE Trans. Commun. (Early Access), pp.1–18, Nov. 2020.

[2] M. Xiao, S. Mumtaz, Y. Huang, L. Dai, Y. Li, M. Matthaiou, G.K. Karagiannidis, E. Björnson, K. Yang, I. Chih-Lin, and G. Amitabha, "Millimeter wave communications for future mobile networks," IEEE J. Sel. Areas Commun., vol.35, no.9, pp.1909–1935, Sept. 2017.

[3] T.S. Rappaport, R.W. Heath Jr, R.C. Daniels, and J.N. Murdock, Millimeter Wave Wireless Communications, Pearson Education, London, England, 2015.

[4] T. Baykas, C.-S. Sum, Z. Lan, J. Wang, M.A. Rahman, H. Harada, and S. Kato, "IEEE 802.15.3c: The first IEEE wireless standard for data rates over 1 Gb/s," IEEE Commun. Mag., vol.49, no.7, pp.114–121, July 2011.

[5] J. Wang, Z. Lan, C.-W. Pyo, T. Baykas, C.-S. Sum, M.A. Rahman, J. Gao, R. Funada, F. Kojima, H. Harada, and S. Kato, "Beam codebook based beamforming protocol for multi-Gbps millimeter-wave WPAN systems," IEEE J. Sel. Areas Commun., vol.27, no.8, pp.1390–1399, Oct. 2009.

[6] "Wireless LAN medium access control (MAC) and physical layer (PHY) specification," IEEE Std. 802.11ad-2012.

[7] https://mentor.ieee.org/802.11/dcn/15/11-15-0625-03-00ay-ieee-802-11-tgay-usage-scenarios.pptx

[8] "User equipment (UE) radio transmission and reception; Part 1: Range 1 standalone," 3GPP TS38.101-1 V15.2.0.

[9] G.R. MacCartney, S. Deng, S. Sun, and T.S. Rappaport, "Millimeter wave human blockage at 73 GHz with a simple double knife edge diffraction model and extension for directional antennas," Proc. IEEE VTC2016-Fall, pp.1–5, Montréal, Canada, Sept. 2016.

[10] ITU-R Recommendation, "Propagation by diffraction," Recommendation P.526-7, pp.1–21, Jan. 2001.

[11] M. Jacob, C. Mnianke, and T. Kürner, "A dynamic 60 GHz radio channel model for system level simulations with MAC protocols for IEEE 802.11ad," Proc. IEEE ISCE 2010, pp.1–5, Braunschweig, Germany, June 2010.

[12] M. Jacob, S. Priebe, A. Maltsev, A. Lomayev, V. Erceg, and T. Kürner, "A ray tracing based stochastic human blockage model for the IEEE 802.11ad 60 GHz channel model," Proc. IEEE EuCAP 2011, pp.3084–3088, Rome, Italy, April 2011.

[13] M. Jacob, S. Priebe, M. Peter, and M. Wisozki, "Fundamental analyses of 60 GHz human blockage," Proc. IEEE EuCAP 2013, pp.117–121, Gothenburg, Sweden, April 2013.

[14] https://news.panasonic.com/jp/press/data/jn080108-13/jn080108-13.html

[15] S. Aggarwal, A. Thirumurugan, and D. Koutsonikolas, "A first look at 802.11ad performance on a smartphone," Proc. ACM Mobicom 2019 Workshops, pp.13–18, Los Cabos, Mexico, Oct. 2019.

[16] Iperf, https://iperf.fr/

[17] I. Goodfellow, Y. Bengio, and A. Courville, Deep Learning, MIT Press, Cambridge, MA, USA, 2016.

[18] M. Mohri, A. Rostamizadeh, and A. Talwalkar, Foundations of Machine Learning, MIT press, London, England, 2018.

[19] C. Bishop, Pattern Recognition and Macine Learning, Springer, Berlin, Germany, 2010.

[20] P. Kairouz, H.B. McMahan, B. Avent, A. Bellet, M. Bennis, A.N. Bhagoji, K. Bonawitz, Z. Charles, G. Cormode, R. Cummings,, et al., "Advances and open problems in federated learning," Found. Trends® Mach. Learn., vol.14, no.1, pp.1–105, March 2021.

[21] J. Park, S. Samarakoon, M. Bennis, and M. Debbah, "Wireless network intelligence at the edge," Proc. IEEE, vol.107, no.11, pp.2204–2239, Nov. 2019.

[22] O. Gupta and R. Raskar, "Distributed learning of deep neural network over multiple agents," Elsevier J. Netw. Comput. Appl., vol.116, pp.1–8, Aug. 2018.

[23] R.S. Sutton and A.G. Barto, Reinforcement Learning: An Introduction, MIT Press, Cambrige, MA, USA, 1998.

[24] C. Szepesvári, "Algorithms for reinforcement learning," Synth. Lect. Artif. Intell. Mach. Learn, vol.4, no.1, pp.1–103, June 2010.

[25] V. Mnih, K. Kavukcuoglu, D. Silver, A.A. Rusu, J. Veness, M.G. Bellemare, A. Graves, M. Riedmiller, A.K. Fidjeland, G. Ostrovski,, et al., "Human-level control through deep reinforcement learning," Nature, vol.518, no.529, pp.529–533, Feb. 2015.

[26] E. Perahira and M.X. Gong, "Gigabit wireless LANs: An overview of IEEE 802.11ac and 802.11ad," ACM SIGMOBILE Moble Comput. Commun. Rev., vol.15, no.3, pp.23–33, July 2011.

[27] X. Tie, K. Ramachandran, and R. Mahindra, "On 60 GHz wireless link performance in indoor environments," Proc. ACM PAM 2012, pp.147–157, Vienna, Austraria, March 2012.

[28] K. Haneda, "Channel models and beamforming at millimeter-wave frequency bands," IEICE Trans. Commun., vol.E98-B, no.5, pp.755–772, May 2015.

[29] K. Sakaguchi, E.M. Mohamed, H. Kusano, M. Mizukami, S. Miyamoto, R.E. Rezagah, K. Takinami, K. Takahashi, N. Shirakawa, H. Peng, T. yamamoto, and S. Namba, "Millimeter-wave wireless LAN and its extension toward 5G heterogeneous networks," IEICE Trans. Commun., vol.E98-B, no.10, pp.1932–1947, Oct. 2015.

[30] T. Nische, G. Bielsa, A. Loch, and J. Widmer, "Boon and bane of 60 GHz networks: Practical insights into beamforming, interference, and frame level operation," Proc. ACM CoNEXT 2015, pp.1–6, Heidelberg, Germany, Dec. 2015.

[31] S. Collonge, G. Zaharia, and G.E. Zein, "Influence of the human activity on wide-band characteristics of the 60 GHz indoor radio channel," IEEE Trans. Wireless Commun., vol.3, no.6, pp.2396–2406, Nov. 2004.

[32] T. Wang, M. Umehira, H. Otsu, S. Takeda, T. Miyajima, and K. Kagoshima, "A twin cylinder model for moving human body shadowing in 60 GHz WLAN," Proc. APCC 2015, pp.188–192, Kyoto, Japan, Oct. 2015.

[33] G.R. MacCartney and T.S. Rappaport, "A flexible millimeter-wave channel sounder with absolute timing," IEEE J. Sel. Areas Commun., vol.35, no.6, pp.1402–1418, June 2017.

[34] P. Karadimas, B. Allen, and P. Smith, "Human body shadowing characterization for 60-GHz indoor short-range wireless links," IEEE Antennas Wireless Propag. Lett., vol.12, pp.1650–1653, Dec. 2013.

[35] A. Goldsmith, Wireless Communications, Cambridge University Press, Cambrige, MA, USA, 2004.

[36] H. Akaike, "A new look at the statistical model identification," IEEE Trans. Autom. Control, vol.19, no.6, pp.716–723, Dec. 1974.

[37] S.R. Saunder and A.A. Zavala, Antennas and Propagation for Wireless Communication Systems, Wiley, Hoboken, NJ, USA, 2007.

[38] A. Papoulis and S. Pillai, Probability, Random Variables and Stochastic Processes, 4th ed., McGraw-Hill New York, NY, USA, 2002.

[39] Y. Niu, Y. Li, D. Fin, and A.V. Vasilakos, "A survey of millimeter wave communications (mmWave) for 5G: Opportunities and challenges," Springer Wirel. Netw., vol.21, no.8, pp.2657–2676, Nov. 2015.

[40] C. Dehos, J. Gonzàlez, A.D. Domenica, D. Kténas, and L. Dussopt, "Millimeter wave access and backhauling: The solution to the exponential data traffic increase in 5G mobile communication systems?," IEEE Commun. Mag., vol.52, no.9, pp.88–95, Sept. 2014.

[41] P. Wang, Y. L.i, L. Song, and B. Vucetic, "Multi-gigabit millimeter wave wireless communications for 5G: From fixed access to cellular networks," IEEE Commun. Mag., vol.53, no.1, pp.168–178, Jan. 2015.

[42] A. Osseiran, F. Boccardi, V. Braun, K. Kusume, P. Marsch, M. Maternia, O. Queseth, M. Schellmann, H. Schotten, H. Taoka,, et al., "Scenarios for 5G mobile and wireless communications: The vision of the METIS project," IEEE Commun. Mag., vol.52, no.5, pp.26–35, May 2014.

[43] ITU-R Recommendation, "IMT vision–framework and overall objectives of the future development of IMT for 2020 and beyond," Recommendation M2083, pp.1–19, Sept. 2015.

[44] X. Zhang, S. Zhou, X. Wang, D. Zhu, and M. Lei, "Improving network throughput in 60 GHz WLANs via multi-AP diversity," Proc. IEEE ICC 2012, pp.4803–4807, Ottawa, Canada, June 2012.

[45] Y. Oguma, R. Arai, T. Nishio, K. Yamamoto, and M. Morikura, "Implementation and evaluation of reactive base staiton selection for human blockage in mmWave communications," Proc. APCC 2015, pp.1–6, Kyoto, Japan, Oct. 2015.

[46] M. Umehira, G. Saito, S. Takeda, T. Miyajima, and K. Kagoshima, “Feasibility of RSSI based access network detection for multi-band WLAN using 2.4/5 GHz and 60 GHz,” Proc. IEEE WPMC 2014, pp.1–6, Sydney, Australia, Sept. 2014.

[47] M. Polese, M. Giordani, M. Mezzavilla, S. Rangan, and M. Zorzi, “Improved handover through dual connectivity in 5G mmWave mobile networks,” IEEE J. Sel. Areas Commun., vol.35, no.9, pp.2069–2084, Sept. 2017.

[48] Y. Sun, G. Feng, S. Qin, Y.C. Liang, and T.S.P. Yum, “The SMART handoff policy for millimeter wave heterogeneous cellular networks,” IEEE Trans. Mobile Comput., vol.17, no.6, pp.1456–1468, June 2018.

[49] E.S. Navarro, Y. Lin, and V. Wong, “An MDP-based vertical handoff decision algorithm for heterogeneous wireless networks,” IEEE Trans. Veh. Technol., vol.57, no.2, pp.1243–1254, March 2008.

[50] M. Mezzavilla, S. Goyal, S. Panwar, S. Rangan, and M. Zorzi, “An MDP model for optimal handover decisions in mmWave cellular networks,” Proc. EUCNC 2016, pp.100–105, Athens, Greece, June 2016.

[51] C. Dhahri and T. Ohtsuki, “Adaptive Q-learning cell selection method for open-access femtocell networks: Multi-user case,” IEICE Trans. Commun., vol.E97-B, no.8, pp.1679–1688, Aug. 2014.

[52] C. Dhahri and T. Ohtsuki, “Q-learning cell selection for femtocell networks: Single and multi-user case,” Proc. IEEE GLOBECOM 2012, pp.4975–4980, Anaheim, CA, USA, Dec. 2012.

[53] H. Tabrizi, G. Farhadi, and J. Cioffi, “Dynamic handoff decision in heterogeneous wireless systems: Q-learning approach,” Proc. IEEE ICC 2012, pp.3217–3222, Ottawa, Canada, June 2012.

[54] B.-J. Chang and J.-F. Chen, “Cross-layer-based adaptive vertical handoff with predictive RSS in heterogeneous wireless networks,” IEEE Trans. Veh. Technol., vol.57, no.6, pp.3679–3692, Nov. 2008.

[55] Q. Liu and C.W. Chen, “Smart downlink scheduling for multimedia streaming over LTE networks with hard handoff,” IEEE Trans. Circuits Syst. Video Technol., vol.25, no.11, pp.1815–1829, Nov. 2015.

[56] O. Kaltiokallio, H. Yiğitler, and R. Jäntti, “A three-state received signal strength model for device-free localization,” IEEE Trans. Veh. Technol., vol.66, no.10, pp.9226–9240, Oct. 2017.

[57] C.-R. Lin, Y.-J. Chen, and L.-C. Wang, “Handoff delay analysis in SDN-enabled mobile networks: a network calculus approach,” Proc. IEEE VTC2017-Fall, pp.1–5, Toronto, Canada, Sept. 2017.

[58] D. Eigen, C. Puhrsch, and R. Fergus, “Depth map prediction from a single image using a multi-scale deep network,” Proc. NIPS 2014, pp.1–9, Montréal, Canada, Dec. 2014.

[59] N.W. Sung, N.-T. Pham, T. Huynh, and W.-J. Hwang, “Predictive association control for frequent handover avoidance in femtocell networks,” IEEE Commun. Lett., vol.17, no.5, pp.924–927, May 2013.

[60] S. Zang, W. Bao, P.L. Yeoh, H. Chen, Z. Lin, B. Vucetic, and Y. Li, “Mobility handover optimization in millimeter wave heterogeneous networks,” Proc. IEEE ISCIT 2017, pp.1–6, Cairns, Australia, Sept. 2017.

[61] S. Zansg, W. Bao, P.L. Yeoh, B. Vucetic, and Y. Li, “Managing vertical handovers in millimeter wave heterogeneous networks,” IEEE Trans. Commun., vol.67, no.2, pp.1629–1644, Feb. 2019.

[62] Y. Koda, K. Yamamoto, T. Nishio, and M. Morikura, “Reinforcement learning based predictive handover for pedestrian-aware mmWave networks,” Proc. IEEE INFOCOM 2018 Workshops, pp.1–6, Honolulu, HI, USA, April 2018.

[63] Y. Oguma, R. Arai, T. Nishio, K. Yamamoto, and M. Morikura, “Proactive base station selection based on human blockage prediction using RGB-D cameras for mmWave communications,” Proc. IEEE GLOBECOM 2015, pp.1–6, San Diego, CA, USA, Dec. 2015.

[64] Y. Oguma, T. Nishio, K. Yamamoto, and M. Morikura, “Proactive handover based on human blockage prediction using RGB-D cameras for mmWave communications,” IEICE Trans. Commun., vol.E99-B, no.8, pp.1734–1744, Oct. 2016.

[65] T. Nishio, R. Arai, K. Yamamoto, and M. Morikura, “Proactive traffic control based on human blocakge prediction using RGB-D cameras for millimeter-wave communciations,” Proc. IEEE CCNC 2015, pp.152–153, Las Vegas, NV, USA, Jan. 2015.

[66] H. Okamoto, T. Nishio, M. Morikura, and K. Yamamoto, “Machine-learning-based throughput estimation using images for mmWave communications,” Proc. IEEE VTC2017-Spring, pp.1–6, Sydney, Australia, June 2017.

[67] T. Nishio, H. Okamoto, K. Nakashima, Y. Koda, K. Yamamoto, M. Morikura, Y. Asai, and R. Miyatake, “Proactive received power prediction using machine learning and depth images for mmWave networks,” IEEE J. Sel. Areas Commun., vol.37, no.11, pp.2413–2427, Nov. 2019.

[68] X. Tan, X. Luan, Y. Cheng, A. Liu, and J. Wu, “Cell selection in two-tier femtocell networks using Q-learning algorithm,” Proc. ICACT 2014, pp.1036–1040, PyeongChang, Korea, Feb. 2014.

[69] “General packet radio service (GPRS) enhancements for evolved universal terrestrial radio access network (E-UTRAN) access,” 3GPP TS 23.401-2013.

[70] W. Jiao, P. Jiang, and Y. Ma, “Fast handover scheme for real-time applications in mobile WiMAX,” Proc. IEEE ICC 2017, pp.6038–6042, Glasgow, Scotland, June 2017.

[71] H. Hassanieh, O. Abari, M. Rodriguez, M. Abdelghany, D. Katabi, and P. Indyk, “Fast millimeter wave beam alignment,” Proc. ACM SIGCOMM 2018, pp.432–445, Budapest, Hungary, Aug. 2018.

[72] B. Peng, S. Rey, D.M. Rose, S. Hahn, and T. Kuerner, “Statistical characteristics study of human blockage effect in future indoor millimeter and sub-millimeter wave wireless communications,” Proc. IEEE VTC2018-Spring, pp.1–5, Porto, Portugal, June 2018.

[73] K. Khoshelham and S.O. Elberink, “Accuracy and resolustion of Kinect depth data for indoor mapping applications,” Sensors, vol.12, no.2, pp.1437–1454, Feb. 2012.

[74] P. Ji, H.-M. Tsai, C. Wang, and F. Liu, “Vehicular visible light communications with LED taillight and rolling shutter camera,” Proc. IEEE VTC2014-Spring, pp.1–6, Seoul, Korea, May 2014.

[75] R. Hill, C. Madden, A. van den Hengel, H. Detmold, and A. Dick, “Measuring latency for video surveillance systems,” Proc. IEEE DICTA 2009, pp.89–95, Melbourne, Australia, Dec. 2009.

[76] T. Choi, C.U. Bas, R. Wang, S. Hur, J. Park, J. Zhang, and A.F. Molisch, “Measurement based directional modeling of dynamic human body shadowing at 28 GHz,” Proc. IEEE GLOBECOM 2018, pp.1–6, Abu Dhabi, UAE, Dec. 2018.

[77] L.C. Gimenez, P.H. Michaelsen, K.I. Pedersen, T.E. Kolding, and H.C. Nguyen, “Towards zero data interruption time with enhanced synchronous handover,” Proc. IEEE VTC2017-Spring, pp.1–6, Sydney, Australia, May 2017.

[78] A. Talukdar, M. Cudak, and A. Ghosh, “Handoff rates for millimeter-wave 5G systems,” Proc. IEEE VTC2014-Spring, pp.1–5, Seoul, Korea, May 2014.

[79] G. Theocharous, P.S. Thomas, and M. Ghavamzadeh, “Personalized ad recommendation systems for life-time value optimization with guarantees,” Proc. IJCAI 2015, pp.1806–1812, Buenos Aires, Republica Argentina, July 2015.

[80] Y.-S. Huang, F.-Y. Leu, J.-C. Liu, Y.-L. Huang, and W.C.-C. Chu, “A handover scheme for LTE wireless networks under the assistance

of GPS," Proc. IEEE BWCCA 2013, pp.399–403, Compiegne, France, Oct. 2013.

[81] P.H. Lehne, A.A. Glazunov, K. Mahmood, and P.-S. Kildal, "Analyzing smart phones' 3D accelerometer measurements to identify typical usage positions in voice mode," Proc. EuCAP 2016, pp.1–5, Davos, Switzerland, April 2016.

[82] T. Ei and F. Wang, "A trajectory-aware handoff algorithm based on GPS information," Springer Ann. Telecommun., vol.65, no.7-8, pp.411–417, Dec. 2010.

[83] M. Taha, L. Parra, L. Garcia, and J. Lloret, "An intelligent handover process algorithm in 5G networks: The use case of mobile cameras for environmental surveillance," Proc. IEEE ICC 2017 Workshops, pp.840–844, Paris, France, May 2017.

[84] X. Wang, L. Kong, F. Kong, F. Qiu, M. Xia, S. Arnon, and G. Chen, "Millimeter wave communication: A comprehensive survey," IEEE Commun. Surveys Tuts., vol.20, no.3, pp.1616–1653, June 2018.

[85] T. Miyaki, T. Yamasaki, and K. Aizawa, "Tracking persons using particle filter fusing visual and Wi-Fi localizations for widely distributed camera," Proc. IEEE ICIP 2007, pp.225–228, San Antonio, TX, USA, Sept. 2007.

[86] T. Oskiper, H.-P. Chiu, Z. Zhu, S. Samarasekera, and R. Kumar, "Multi-modal sensor fusion algorithm for ubiquitous infrastructure-free localization in vision-impaired environments," Proc. IEEE/RSJ IROS 2010, pp.1513–1519, Taipei, Taiwan, Oct. 2010.

[87] A. Alahi, A. Haque, and L. Fei-Fei, "RGB-W: When vision meets wireless," Proc. IEEE ICCV 2015, pp.3289–3297, Santiago, Chile, Dec. 2015.

[88] T.T.T. Pham, T.-L. Le, and T.-K. Dao, "Fusion of WiFi and visual signals for person tracking," Proc. ACM SoICT 2016, pp.345–351, Ho Chi Minh City, Vietnam, Dec. 2016.

[89] H.B. McMahan, E. Moore, D. Ramage, S. Hampson, and B.A.Y. Arcas, "Communication-efficient learning of deep networks from decentralized data," Proc. AISTATS 2017, pp.1–11, Fort Lauderdale, FL, USA, April 2016.

[90] A. Elgabli, J. Park, A.S. Bedi, M. Bennis, and V. Aggarwal, "GADMM: Fast and communication efficient framework for distributed machine learning," J. Mach. Learn. Res, vol.21, no.76, pp.1–39, March 2020.

[91] J. Konečnỳ, H.B. McMahan, F.X. Yu, P. Richtárik, A.T. Suresh, and D. Bacon, "Federated learning: Strategies for improving communication efficiency," arXiv preprint arXiv:1610.05492, pp.1–10, Oct. 2016.

[92] Y. Lin, S. Han, H. Mao, Y. Wang, and W.J. Dally, "Deep gradient compression: Reducing the communication bandwidth for distributed training," Proc. ICLR 2018, pp.1–14, Vancouver, Canada, April 2017.

[93] N. Agarwal, A.T. Suresh, F.X.X. Yu, S. Kumar, and B. McMahan, "cpSGD: Communication-efficient and differentially-private distributed SGD," Proc. NeurIPS 2018, pp.7564–7575, Vancouver, Canada, Dec. 2018.

[94] E. Jeong, S. Oh, H. Kim, J. Park, M. Bennis, and S.-L. Kim, "Communication-efficient on-device machine learning: Federated distillation and augmentation under non-IID private data," Proc. NeurIPS Workshops., pp.1–6, Montreal, Canada, Nov. 2018.

[95] P. Vepakomma, O. Gupta, T. Swedish, and R. Raskar, "Split learning for health: Distributed deep learning without sharing raw patient data," arXiv preprint arXiv:1812.00564, pp.1–7, Dec. 2018.

[96] I. Sutskever, J. Martens, G. Dahl, and G. Hinton, "On the importance of initialization and momentum in deep learning," Proc. ICML 2013, pp.1139–1147, Atlabta, GA, USA, June 2013.

[97] M.C. Hout, H.J. Godwin, G. Fitzsimmons, A. Robbins, T. Menneer, and S.D. Goldinger, "Using multidimensional scaling to quantify sim-

ilarity in visual search and beyond," Springer Atten., Percept. Psychophys., vol.78, no.1, pp.3–20, Jan. 2016.

[98] M. Fukuyama, "Society 5.0: Aiming for a new human-centered society," Japan Spotlight, vol.27, pp.47–50, July 2018.

Publication List

Journal Papers

1. Y. Koda, K. Yamamoto, T. Nishio and M. Morikura, "Measurement method of temporal attenuation by human body in off-the-thelf 60 GHz WLAN with HMM-based transmission state estimation," Hindawi Wirel. Commun. Mob. Comput., vol. 2018, article ID 7846936, pp. 1–9, April 2018.

2. T. Nishio, H. Okamoto, K. Nakashima, Y. Koda, K. Yamamoto, M. Morikura, Y. Asai, and R. Miyatake, "Proactive received power prediction using machine learning and depth images for mmWave networks," IEEE J. Sel. Areas Commun., vol. 37, no. 11, pp. 2413–2427, Nov. 2019.

3. Y. Koda, K. Nakashima, K. Yamamoto, T. Nishio, and M. Morikura, "Handover management for mmWave networks with proactive performance prediction using camera images and deep reinforcement learning," IEEE Trans. Cogn. Commun. Netw., vol. 6, no. 2, pp. 802–816, June 2020.

4. Y. Koda, J. Park, M. Bennis, K. Yamamoto, T. Nishio, M. Morikura, and K. Nakashima, "Communication-efficient multimodal split learning for mmWave received power prediction," IEEE Commun. Lett., vol. 24, no. 6, pp. 1284–1288, June 2020.

5. Y. Fu, K. Yamamoto, Y. Koda, T. Nishio, M. Morikura, C. Huang, Y. Shirato, and N. Kita, "Stochastic geometry analysis of wireless

backhaul networks with beamforming in roadside environments," IEICE Trans. Commun., vol. E104-B, no. 1, pp. 118–127, Jan. 2021.

International Conference Papers

1. Y. Koda, Y. Oguma, T. Nishio, K. Yamamoto and M. Morikura, "Statistical prediction of human blockage for camera-assisted mmWave communications," Proc. IEEE APWCS 2016, pp. 1–5, Tokyo, Japan, Aug. 2016.

2. Y. Koda, K. Yamamoto, T. Nishio, and M. Morikura, "Time series measurement of IEEE 802.11ad signal power involving human blockage with HMM-based state estimation," Proc. IEEE VTC2017-Fall, pp. 1–5, Toronto, Canada, Sept. 2017.

3. Y. Koda, K. Yamamoto, T. Nishio, and M. Morikura, "Reinforcement learning based predictive handover for pedestrian-aware mmWave networks," Proc. IEEE INFOCOM 2018 Workshops, pp. 692–697, Waikiki, HI, USA, April 2018.

4. K. Nakashima, Y. Koda, K. Yamamoto, H. Okamoto, T. Nishio, M. Morikura, Y. Asai, and R. Miyatake, "Impact of input data size on received power prediction using depth images for mmWave communications," Proc. IEEE VTC2018-Fall, pp. 1–5, Chicago, IL, USA, Aug. 2018.

5. Y. Koda, J. Park, M. Bennis, K. Yamamoto, T. Nishio, and M. Morikura, "One pixel image and RF signal based split learning for mmWave received power prediction," Proc. ACM CoNEXT 2019 Poster, pp. 54–56, Orlando, FL, USA, Dec. 2019.

6. M. Shinzaki, Y. Koda, K. Yamamoto, T. Nishio, and M. Morikura, "Reducing transmission delay in EDCA using policy gradient reinforcement learning," Proc. IEEE CCNC 2020, pp. 1–6, Las Vegas, NV, USA, Jan. 2020.

7. Y. Koda, K. Nakashima, K. Yamamoto, T. Nishio, and M. Morikura, “Cooperative sensing in deep RL-based image-to-decision proactive handover for mmWave networks,” Proc. IEEE CCNC 2020, pp. 1–6, Las Vegas, NV, USA, Jan. 2020.

8. Y. Kihira, Y. Koda, K. Yamamoto, T. Nishio, and M. Morikura, “Adversarial reinforcement learning-based robust access point coordination against uncoordinated interference,” Proc. IEEE VTC2020-Fall, pp. 1–5, held online, Oct. 2020.

9. M. Shinzaki, Y. Koda, K. Yamamoto, T. Nishio, M. Morikura, C. H. Huang, Y. Shirato, and N. Kita, “Deep reinforcement learning-based beam tracking from mmWave antennas installed on overhead messenger wires,” Proc. IEEE VTC2020-Fall, pp. 1–6, held online, Oct. 2020.

10. Y. Koda, K. Yamamoto, T. Nishio, and M. Morikura, “Differentially private AirComp federated learning with power adaptation harnessing receiver noise,” Proc. IEEE GLOBECOM 2020, pp. 1–6, Taipei, Taiwan, Dec. 2020.

Preprints

1. Y. Koda, J. Park, M. Bennis, K. Yamamoto, T. Nishio, and M. Morikura, “Distributed heteromodal split learning for vision aided mmWave received power prediction,” arXiv preprint arXiv:2007.08208, pp. 1–14, July 2020 (submitted to IEEE Trans. Cogn. Commun. Netw.).

2. S. Itahara, T. Nishio, Y. Koda, M. Morikura, and K. Yamamoto, “Distillation-based semi-supervised federated learning for communication-efficient collaborative training with non-IID private data,” arXiv preprint arXiv:2008.06180, pp. 1–11, Aug. 2020 (submitted to IEEE Trans. Mob. Comput.).

3. T. Nishio, Y. Koda, J. Park, M. Bennis, and K. Doppler, “When wireless communications meet computer vision in beyond 5G,” arXiv preprint arXiv:2010.06188, pp. 1–7, Oct. 2020 (submitted to IEEE Commun. Stan. Mag.).
4. Y. Koda, M. Shinzaki, K. Yamamoto, T. Nishio, M. Morikura, Y. Shirato, and N. Kita, “Millimeter wave communications on overhead messenger wire: Deep reinforcement learning-based predictive beam tracking,” arXiv preprint arXiv:2012.00982, pp. 1–12, Dec. 2020 (submitted to IEEE Trans. Cogn. Commun. Netw.).

Technical Reports and Local Conference Papers

1. Y. Koda, Y. Oguma, T. Nishio, K. Yamamoto, and M. Morikura, “Human blockage prediction in mmWave communication based on statical approaches using an RGB-D camera,” IEICE Technical Report, SR2015-96, pp.53–58, Tokyo, Japan, March 2016 (in Japanese).
2. Y. Koda, K. Yamamoto, T. Nishio, and M. Morikura, “Power measurement system for IEEE 802.11ad mmWave with estimation of signal duration,” IEICE Technical Report, SR2016-88, pp.53–58, Matsuyama, Japan, Jan. 2017 (in Japanese).
3. Y. Koda, K. Yamamoto, T. Nishio, and M. Morikura, “Time series measurement of IEEE 802.11ad signal power involving human blockage with HMM-based state estimation,” IEICE Technical Report, RCS147-151, pp.53–58, Sapporo, Japan, July 2017 (in Japanese).
4. Y. Koda, K. Yamamoto, T. Nishio, and M. Morikura, “Time series measurement of IEEE 802.11ad signal power involving human blockage with HMM-based state estimation,” Proc. IEICE Society Conf., B-17-2, p. 353, Tokyo, Japan, Sept. 2017 (in Japanese).
5. Y. Koda, K. Yamamoto, T. Nishio, and M. Morikura, “Predictive handover decision in pedestrian-aware mmWave networks: A rein-

forcement learning approach," IEICE Technical Report, SR2017-131, pp. 95–102, Kanagawa, Japan, March 2018 (in Japanese).

6. Y. Koda, K. Yamamoto, T. Nishio, and M. Morikura, "Reinforcement learning based predictive handover decision in pedestrian-aware mmWave networks," Proc. IEICE General Conf., B-17-8, p. 452, Tokyo, Japan, March 2018 (in Japanese).

7. Y. Koda, K. Yamamoto, T. Nishio, and M. Morikura, "Experimental evaluation of reinforcement learning-based pedestrian-aware predictive handover for mmWave networks," IEICE Technical Report, RCS2018-101, pp. 113–114, Hokkaido, Japan, July 2018 (in Japanese).

8. K. Nakashima, Y. Koda, K. Yamamoto, H. Okamoto, T. Nishio, and M. Morikura, "Deep learning based RSS prediction using RGB-D camera for mmWave communications," IEICE Technical Report, RCS2018-95, pp. 93–94, Hokkaido, Japan, July 2018 (in Japanese).

9. Y. Koda, K. Yamamoto, T. Nishio, and M. Morikura, "Reinforcement learning-based predictive handover decision in pedestrian-aware mmWave networks," Proc. IEICE Society Conf., B-17-8, p. 410, Ishikawa, Japan, Sept. 2018 (in Japanese).

10. Y. Koda, K. Nakashima, K. Yamamoto, T. Nishio, and M. Morikura, "Deep RL-based end-to-end learning of proactive handover policy for camera-assisted mmWave networks," Proc. IEICE General Conf., B-5-100, p. 366, Tokyo, Japan, March 2019 (in Japanese).

11. M. Shinzaki, Y. Koda, K. Yamamoto, T. Nishio, and M. Morikura, "Policy gradient reinforcement learning for reducing transmission delay in EDCA," IEICE Technical Report, RCS2019-52, pp. 91–96, Okinawa, Japan, June 2019 (in Japanese).

12. Y. Koda, K. Yamamoto, T. Nishio, and M. Morikura, "Cooperative camera sensing in deep RL-based proactive handover for mmWave networks," Proc. IEICE Society Conf., B-15-9, p. 252, Osaka, Japan, Sept. 2019 (in Japanese).

13. Y. Koda, K. Nakashima, K. Yamamoto, T. Nishio and M. Morikura, “Handover control for mmWave networks with proactive performance prediction using depth images and deep reinforcement learning,” Proc. IEICE Cross Field Research Association of Super-Intelligent Networking, p. 1, Tokyo, Japan, Nov. 2019 (in Japanese).
14. Y. Koda, J. Park, M. Bennis, K. Yamamoto, T. Nishio, and M. Morikura, “One pixel image and RF signal based split learning for mmWave future RSS prediction,” Proc. IEICE General Conf., B-5-119, p. 407, cancalled, March 2020 (in Japanese).
15. K. Yamamoto, Y. Kihira, Y. Koda, T. Nishio, and M. Morikura, “Factor analysis of communication quality using redundancy-check information in wireless LANs,” Proc. IEICE General Conf., B-5-147, p. 435, cancelled, March 2020 (in Japanese).
16. Y. Koda, K. Yamamoto, T. Nishio, and M. Morikura, “Power adaptation for differentially private over-the-air computation,” Proc. IEICE Society Conf., B-5-30, p. 230, held online, Sept. 2020 (in Japanese).
17. Y. Kihira, Y. Koda, K. Yamamoto, T. Nishio, and M. Morikura, “Interference avoidance by adversarial RL for WLAN,” IEICE Technical Report, SeMI2020-25, pp. 43, held online, Nov. 2020 (in Japanese).

Awards

1. IEEE VTS Tokyo Chapter 2017 Young Researcher’s Encouragement Award.
2. Cross-field Research Association of Super-Intelligent Networking (RISING 2019), Best Poster Presentation Award.
3. The Telecommunications Advancement Foundation, The 35th Telecom System Award, 2019.
4. IEEE Kansai Chapter Student Research Encouragement Award, 2020.